

Nedim Osmic, Adnan Tahirovic and Bakir Lacevic

Octocopter Design: Modelling, Control and Motion Planning

Contents

List of Figures	ix
List of Tables	xiii
1 Introduction	1
2 Modelling	5
2.1 Mechanical design	6
2.2 Vertical motion - lift	6
2.3 Roll	8
2.4 Pitch	9
2.5 Yaw	10
2.6 Frames of reference	11
2.7 Forces, moments and control inputs	13
2.8 Octocopter kinematics	17
2.9 Octocopter dynamics	18
2.10 Motor dynamics	21
2.11 State space model	23
3 Control	25
3.1 Relevant background work	26
3.2 Motor Controller	26
3.3 Control allocation algorithm	30
3.4 Linearized model	32
3.5 Altitude control near equilibrium	35
3.6 Orientation control near equilibrium	35
3.7 Position control near equilibrium	39
3.8 Overall UAV control architecture	42
3.9 RLS-based fault tolerant control	42
3.9.1 Fault-tolerant PD tracking control	46
3.9.2 Simulation results for Fault-tolerant PD tracking control	47
4 Maneuverability	51
4.1 Fault-dependent admissible set of thrust force and torques	51
4.2 Fault-dependent controllability test procedure	56

4.3	Fault-dependent controllability analysis for a quadcopter system	57
4.3.1	Fault-dependent controllability analysis for a hexacopter system	58
4.3.2	Fault-dependent controllability analysis for an octocopter system	58
5	Risk-sensitive motion planning	67
5.1	Presentation of the admissible set of thrust force and torques with a set of inequality constraints	67
5.2	Selected optimization framework for motion planning	68
5.3	Risk-sensitive motion planner based on mission-related fault-tolerant analysis	70
5.4	Simulation results	72
6	Conclusion	91
	Bibliography	93

List of Figures

2.1	An octocopter design based on the PNPNPNP configuration structure, where P and N indicate counterclockwise (motors M_1, M_3, M_5 and M_7) and clockwise (motors M_2, M_4, M_6 and M_8) directions.	7
2.2	The local coordinate system attached to an octocopter. . . .	7
2.3	The forces that influence the movement of an octocopter system.	8
2.4	Distribution of the forces to ensure rotation of an octocopter system around X -axis of the local coordinate system.	9
2.5	Distribution of the forces to ensure rotation of an octocopter system around Y -axis of the local coordinate system.	10
2.6	Distribution of the forces to ensure rotation of an octocopter system around Z -axis of the local coordinate system.	11
2.7	Body and ground fixed frames for a PNPNPNP octocopter system, where P and N indicate counter and clockwise directions depicted with blue and red colors respectively [59]. . . .	12
2.8	Gyroscopic effect.	15
2.9	Simplified rotor geometry.	17
2.10	A simplified octocopter configuration structure.	21
2.11	Equivalent electric circuit of the armature.	22
3.1	Motor speed control diagram	28
3.2	Motor speed tracking.	28
3.3	Time response of the armature current.	29
3.4	Time response of the armature voltage.	29
3.5	Vectorized control of motor speed.	33
3.6	Actuation generation diagram.	33
3.7	Control architecture.	33
3.8	Altitude tracking control diagram.	36
3.9	Altitude tracking results.	36
3.10	Orientation tracking control diagram.	37
3.11	Altitude and orientation tracking results.	38
3.12	Control diagram for tracking x and y Cartesian coordinates. .	40
3.13	Flatness-based control diagram.	41
3.14	Position and orientation tracking results.	43

3.15	Trajectory tracking of Viviani curve achieved with an PNPNPNP octocopter configuration structure without any failure states.	43
3.16	Trajectory tracking for each position and orientation achieved with an PNPNPNP octocopter configuration structure without any failure states. Left: reference and achieved values. Right: tracking errors.	44
3.17	Trajectory tracking achieved with an PNPNPNP octocopter configuration structure with the motor M_3 being in a fault state.	44
3.18	Trajectory tracking achieved with an PNPNPNP octocopter configuration structure and M_3 being in a fault state. Left: reference and achieved values, Right: tracking errors.	45
3.19	Tracking performance achieved in 3D space with an PNPNPNP octocopter configuration structure based on a PD controller and control allocation algorithm with a fault state in motor M_3 starting from $t = 5$ [s].	48
3.20	Tracking performance achieved with an PNPNPNP octocopter configuration based on a PD control with a fault state in motor M_3 starting from $t = 5$ [s]. Left: reference values. Right: tracking error.	49
3.21	Estimation of rotor capacities during the tracking task.	50
4.1	Representation of the four-dimensional admissible region $(T, \tau_x, \tau_y, \tau_z)$ in three-dimensional space (T, τ_x, τ_y) when $\tau_z = 0$	53
4.2	Representation of the four-dimensional admissible region $(T, \tau_x, \tau_y, \tau_z)$ in three-dimensional space (T, τ_x, τ_z) when $\tau_y = 0$	53
4.3	Representation of the four-dimensional admissible region $(T, \tau_x, \tau_y, \tau_z)$ in three-dimensional space (T, τ_y, τ_z) when $\tau_x = 0$	54
4.4	The projection of torques τ_x, τ_y onto the plane $T = mg$ along its orthogonal direction for a PNPNPNP octocopter configuration structure without any fault states.	54
4.5	The projection of torques τ_x and τ_y onto the plane $T = mg$ along its orthogonal direction for a PNPNPNP octocopter configuration structure with a fault state related to the DC motor M_1	55
4.6	The projection of torques τ_x and τ_y onto the plane $T = mg$ along its orthogonal direction, for a PNPNPNP octocopter configuration structure with a double fault state related to the DC motors M_1 and M_2	55
4.7	The projection of torques τ_x and τ_y onto the plane $T = mg$ along its orthogonal direction for a PNPNPNP octocopter configuration structure with a fault state related to the DC motor M_1	59

4.8	The projection of torques τ_x and τ_z onto the plane $T = mg$ along its orthogonal direction a PNPNPNP octocopter configuration structure with a fault state related to the DC motor M_1	60
5.1	Uniform sampling of the Viviani curve with 21 points.	73
5.2	Control input domain (projection onto plane $T = mg$) in case without any faults (green), and in case of M1 in fault state (red).	74
5.3	Paths generated using RIP, RCP, and RSP motion planners. The traversal time is 20 seconds.. . . .	76
5.4	Tracking of trajectories obtained using RIP, RCP, and RSP planners. The nominal traversal time is 20s, with the fault state at M1 occurring at $t = 8s$	77
5.5	Tracking of Cartesian coordinates x , y , z orientation ψ and respective tracking errors e_x , e_y , e_z i e_ψ in case of trajectory generated by RIP planner. The traversal time is 20s, with the fault at M1 occurring at $t=8s$	78
5.6	Tracking of Cartesian coordinates x , y , z orientation ψ and respective tracking errors e_x , e_y , e_z and e_ψ in case of trajectory generated by RCP planner. The traversal time is 20s, with the fault at M1 occurring at $t=8s$	79
5.7	Tracking of Cartesian coordinates x , y , z and orientation ψ and respective tracking errors e_x , e_y , e_z and e_ψ in case of trajectory generated by <i>RSP</i> planner. The traversal time is 20s, with the fault at M1 occurring at $t=8s$	80
5.8	Control input domain (projection onto plane $T = mg$) in case without any faults (green), and in case of simultaneous faults at M1 and M6 (red).	81
5.9	Paths generated using RIP (without fault states), RCP (faults at M1 and M6), and RSP (faults at M1 and M6 – selected inequalities) motion planners. The traversal time is 26 seconds.	82
5.10	Tracking of trajectories obtained using RIP, RCP, and RSP planners. The nominal traversal time is 26s, with the fault states at M1 and M6 occurring at $t=8s$ and $t=12s$ respectively.	83
5.11	Tracking of trajectories obtained using RIP, RCP, and RSP planners. The traversal times are 16s, 26s and 18s respectively. The fault states at M1 and M6 occur at $t=8s$ and $t=12s$ respectively.	84
5.12	Octocopter motion through a narrow corridor (dimensions 1m x 1m x 1m). RRT algorithm is used for generating waypoints.. . . .	88
5.13	Octocopter motion through the corridor with a single fault state at M_1 at $t = 3s$. RCP anticipates the fault state at M_1	89
5.14	Octocopter motion through the corridor with a single fault state at M_1 at $t = 3s$. RCP anticipates the fault state at M_8	89

5.15 Octocopter motion through the corridor with a double fault states at M_1 and M_4 at $t = 3s$ and $t = 5s$ respectively. RCP anticipates the fault state at M_8	90
5.16 Octocopter motion through the corridor with a double fault states at M_1 and M_4 at $t = 5s$ and $t = 8s$ respectively. RCP anticipates the fault state at M_8	90

List of Tables

4.1	Quadcopter: Analysis of single-fault cases.	59
4.2	Hexacopter: Analysis of single-fault cases for the PNPNP and PPNNPN configurations.	60
4.3	Hexacopter: Analysis of double-fault cases for the PNPNP configuration.	61
4.4	Hexacopter: Analysis of double-fault cases for the PPNNPN configuration.	62
4.5	Octocopter: Analysis of single-fault cases for the PNPNP and PPNNPPNN configurations.	64
4.6	Octocopter: Analysis of double-fault cases for the PNPNP configuration.	65
4.7	Octocopter: Analysis of double-fault cases for the PPNNPPNN configuration.	66
5.1	Performance comparison between the RIP and RCP approaches (Case 1, steps 1, 2 and 3).	75
5.2	Performance comparison for RIP, RCP and RSP motion planners with traversal time $T=20s$ (Case 1, steps 5 and 6).	76
5.3	Performance comparison for RIP, RCP and RSP motion planners with traversal time $T=20s$ (Case 1, steps 5 and 6).	77
5.4	Performance comparison for RIP, RCP and RSP motion planners in case of double fault, where their minimum respective traversal times are considered (Case 2, steps 2, 3, and 5).	81
5.5	Performance comparison for RIP, RCP and RSP motion planners in case of simultaneous fault at M1 and M6 (Case 2, steps 5 and 6). Traversal time is $T=26s$	82
5.6	Performance comparison for RIP, RCP and RSP motion planners in case of simultaneous fault at M1 and M6 (Case 2, steps 5 and 6). Traversal times are $T=16s$, $26s$, and $18s$ respectively.	83
5.7	Performance comparison between the RIP, RCP and RSP planners (Case 3. step 1, 2 and 3).	85
5.8	The number of unsatisfied inequalities for RIP, RCP and RSP planners for each possible single fault state (M_i), with respect to feasible control inputs (Case 3, steps 4,5, and 6).	86

5.9	Feasibility comparison for trajectories obtained using RIP, RCP and RSP planners, for each possible single fault state (M_i). The time instant of fault occurrence is random.	86
-----	---	----

1

Introduction

CONTENTS

In recent years, unmanned aerial vehicles (UAV) have become one of the major fields of robotics research in academic and industrial communities due to the broad range of their potential applications, including search and rescue missions in urban [77, 10, 3] and non-urban environments [23], aerial construction [39], precision agriculture [8], [82], disaster management [45, 70, 40], remote sensing [14, 15], power line and structural inspection [22, 38, 9, 50], exploration and mapping of unknown environments [16, 74, 75, 76], surveillance [18],[20], swarming [36], as well as monitoring and traffic analysis [62]. Multirotor aerial vehicles (MAV) are among the most popular UAV platforms due to characteristics such as small geometries, vertical takeoff and landing, low cost, simple construction, degrees of freedom, their inherent maneuverability, as well as ability to perform the tasks which are highly risk for humans. The miniaturization of actuators and sensors, power density improvements of batteries and the ubiquity of low cost computing platforms have additionally motivated research in the field of small UAVs [5]. Nowadays, there exist different design solutions for MAVs, ranging from micro and mini to heavy MAVs with large endurance [25]. Quadrotors have the simplest MAV configuration based on the four rotor actuation. Quadrotor platforms such as AR-Drone have become a standard aerial robotic research platform used in scientific community [44, 33].

Regardless of the structural design type of a MAV, different faults may occur during the task execution. Faults can affect functional properties of actuators, sensors, and controllers and they can be of a structural nature. If a failure occurs, the mission execution may be terminated. The detailed Failure Mode and Effect Analysis (FMEA), presented in [67], identifies critical mechanical, electrical and software components of MAV systems. Reliability requirements of mechanical and electrical components are generally met via redundancy. The critical software components include the control system and the attitude estimation algorithm, which need to be fault-tolerant to satisfy reliability constraints. In [54] and [56], the authors have investigated a control strategy for a quadcopter in the case of either a single or multiple rotor faults,

including double-fault of two opposing propellers and all combinations of triple faults caused by failures of different propellers.

To increase a likelihood of mission accomplishment, a various types of redundancy can be imposed in the MAV design such as redundancy of the propulsion system. In [13, 12, 71, 79, 41], the authors investigated how the controllability property of a system with respect to different rotor faults could be preserved by increasing the number of rotors, or using a rotor with a possibility to tilt motors [52], [46]. As an example, in [67] it was demonstrated how to control degrees of freedom of an octocopter (a MAV designed with 8 rotors) for any potential double-fault scenarios. To design a highly reliable MAV, it is inevitable to increase the total number of rotors in the initial system design. As an example, octocopters are inherently reliable with regards to double-faults scenarios, with full system controllability being preserved in 89% of those scenarios [67].

Regardless of whether the configuration of a MAV is redundant, the control algorithm has a significant role in improving its overall fault-tolerance. If a control algorithm is fault-ignorant, using redundant components in the initial design does not necessary increase reliability of a MAV system, that is the probability of completing the mission. A large number of fault-tolerant control algorithms that inherently possess a certain level of robustness with respect to possible failures include sliding mode control [80], adaptive fault-tolerant control [81], [30], control allocation method for MAVs [7], [58], reconfigurable control [11], backstepping method [24], [21], model predictive control [32], control based on linear quadratic regulator [37], fuzzy predictive control [49], to name a few.

Fault-tolerant controls and estimation techniques are based on Fault Detection and Isolation (FDI) algorithms, which identify and localize system faults. An extensive survey of these algorithms is presented in [83], [27]. In case of fault-tolerant MAV systems, the state-of-the-art methods heavily rely on observer based FDI techniques. Notable examples include Luenberger state estimation [68], Moving Horizon Estimation (MHE) and Unscented Kalman Filtering (UKF) [29] for actuator fault diagnosis, as well as Thau observer [17] and multi-observer [2] for sensor fault diagnosis. A fault detection and isolation, formulated as the least squares parameter identification problem, has already been considered in [14] for linear time invariant state space models. A more specific approach, tailored for a class of nonlinear aerodynamic models can be found in [15].

Besides construction-based redundancy as well as control-induced fault tolerance, a further increase of mission reliability can be achieved at the motion planning stage. Namely, in case the system is aware of potential risks related to failure probabilities, it is then possible to carefully generate trajectories to make the system capable of dealing with different faults. Specifically, each faulty state may have some risky manoeuvres that the system may want to avoid, especially in case a faulty state is highly probable. A conservative approach to address this problem would be to generate the system trajectories

based on safe maneuvers only. In that case, the system would significantly deteriorate its flying capabilities without achieving performances for which it is designed. However, a motion planner based on the decreased probability of moving with risky maneuvers for the given mission has been introduced in [61]. In this way, the planner compromises two extremes, a safe and reliable planner with bad performance (risk conservative planner) and a risk-ignorant planner with the best possible performance.

The octocopter system is consisted of an 8-rotor system which makes it a representative example for all three reliability aspects. First, it is highly redundant by construction and capable of flying even in case of multiple motor faults simultaneously occur during the mission. Second, fault-tolerant control can come to the fore in case when there exist more fault-tolerant degrees of freedom. For instance, the octocopter system has more fault states in which it is still capable of completing the mission than the quadcopter and hexacopter systems. Third, the motion planner algorithms designed for the octocopter system are capable of taking into account a wide spectrum of potential faulty states into account. This may help to generate only those trajectories along which the octocopter would be likely ready for potential faults to occur preserving good performance of a risk-ignorant planner and safety of a risk conservative approach.

This book provides a solution to the control and motion planning design for an octocopter system. It includes a particular choice of control and motion planning algorithms which is based on the authors' previous research work, so it can be used as a reference design guidance for students, researchers as well as autonomous vehicles hobbyists. The control is constructed based on a fault tolerant approach aiming to increase the chances of the system to detect and isolate a potential failure in order to produce feasible control signals to the remaining active motors. The used motion planning algorithm is risk-aware by means that it takes into account the constraints related to the fault-dependant and mission-related maneuverability analysis of the octocopter system during the planning stage. Such a planner generates only those reference trajectories along which the octocopter system would be safe and capable of good tracking in case of a single motor fault and of majority of double motor fault scenarios. The control and motion planning algorithms presented in the book aim to increase overall reliability of the system for completing the mission.

In Chapter 2, we derive the octocopter dynamics and provide its full state space model. Chapter 3 includes different controllers used in the octocopter control architecture. A variant of fault-tolerant controller is also described which can be used to increase overall system reliability. Chapter 4 explains how to conduct a maneuverability analysis aiming to understand octocopter controllability constraints related to different possible motor faults and to the given mission. This chapter also describes how it is possible to exploit such analysis in order to design a risk-aware motion planner. Conclusion remarks are outlined in Chapter 5.



2

Modelling

CONTENTS

2.1	Mechanical design	5
2.2	Vertical motion - lift	6
2.3	Roll	8
2.4	Pitch	9
2.5	Yaw	10
2.6	Frames of reference	10
2.7	Forces, moments and control inputs	13
2.8	Octocopter kinematics	16
2.9	Octocopter dynamics	18
2.10	Motor dynamics	20
2.11	State space model	22

Although the Lagrangian formulation of dynamics [4] [63], [78] can also be used to derive a general octocopter dynamical model, in this book the model is derived based on the Newton-Euler formulation from the direct interpretation of Newton's second law of motion [4], [19], [43], [59], [35]. The dynamical model plays an important role in MAV motion analysis and provides understanding of system behaviour (position, orientation, velocity and acceleration) with respect to applied inputs (e.g., voltages applied to MAV rotors). The model is also used in silico for testing different control laws that can be potentially implemented aiming to force the system to behave in a desired manner. In order to present the underlying model equations, we first explain the working principle of an octocopter system that secures its desired movements (roll, pitch and yaw). Then, we present octocopter kinematics and dynamics of linear and angular motions together with motor dynamics. We also explain what types of forces and moments act on the octocopter and how they can be framed in order to be used in the final dynamical model.

2.1 Mechanical design

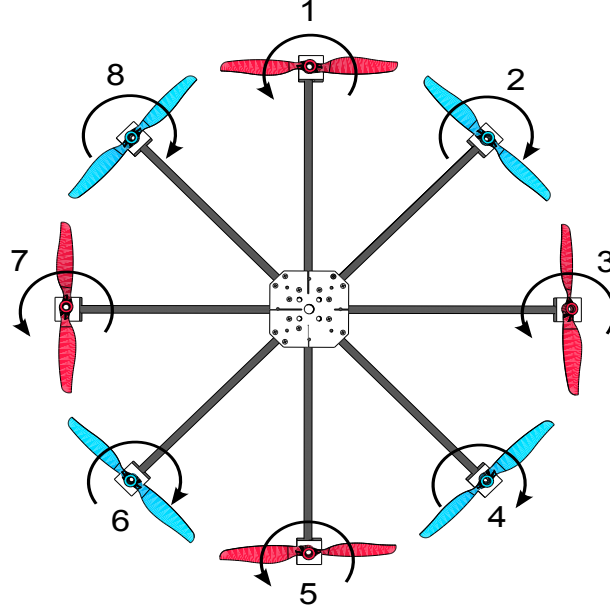
The octocopter system shown in Fig. 2.1 consists of eight arms of the same length l that are fixed to a support plate, where each arm is equipped with a DC motor M_i driving a fixed pitch rotor, where $i = 1, \dots, 8$. The angle between any two adjacent arms in an octocopter design is 45 degrees. The DC motors depicted with blue color (M_2, M_4, M_6 and M_8) rotate clockwise, while those depicted with red color (M_1, M_3, M_5 and M_7) rotate counterclockwise. Therefore, an octocopter system is inherently balanced with regard to the drag moment which can be generated by the motors included in the design. All other system components should be placed in a protective case which is mounted to the support plate.

If the origin of the local coordinate system is fixed to the center of mass of the octocopter system (see Fig. 2.2), where X -axis is taken along the DC motors M_7 and M_3 with the positive direction being from M_7 to M_3 , Y -axis is taken along the rotors M_5 and M_1 with the positive direction being from M_5 to M_1 , and Z -axis is directed upward, one gets the so-called '+' with the PNPNNPN configuration structure, where P and N indicate positive and negative motor rotations, respectively. Such a setup represents a classical octocopter configuration structure. However, the so-called 'X' formation based on the PPNNPPNN DC motor movement directions [67] is also possible to use, as well as those with different motor distributions including the so-called 'V' and 'X' constructions based on the coaxial rotor setups [64].

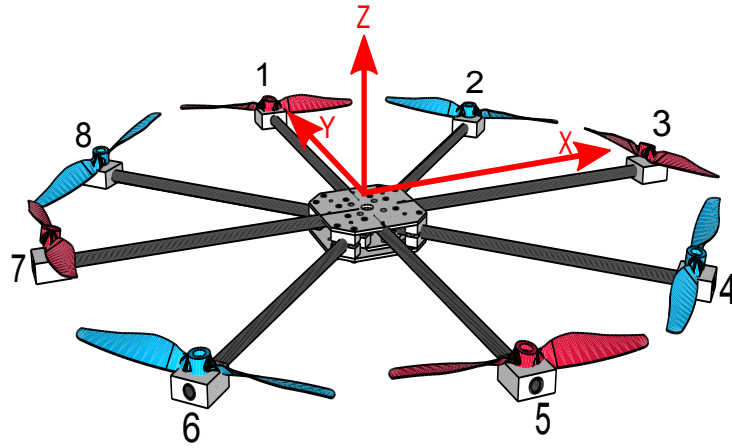
Since the mechanical construction contains the motors attached to the propellers as the only moving parts of the octocopter, the input signals used to force the octocopter to change its position and orientation represent the control variables of interest. In the following subsections, we present different moving directions based on which it is possible to control an octocopter system.

2.2 Vertical motion - lift

Fig. 2.1 illustrates a mechanical structure of an octocopter based on eight motors setup attached with eight propellers, where the motors (M_1, M_3, M_5, M_7) and (M_2, M_4, M_6, M_8) rotate in the opposite directions. In case when the equal input signals are applied to these motors, eight equal vertical forces ($F_1 = F_2 = \dots = F_8$) would be generated, all acting in the positive direction along Z -axis which is opposite to the direction of gravitational force. Whenever the sum of the generated forces, which are produced by each motor rotating with angular speed ω_0 [$rad s^{-1}$], is greater than the gravitational

**FIGURE 2.1**

An octocopter design based on the PNPNPNP configuration structure, where P and N indicate counterclockwise (motors M_1 , M_3 , M_5 and M_7) and clockwise (motors M_2 , M_4 , M_6 and M_8) directions.

**FIGURE 2.2**

The local coordinate system attached to an octocopter.

force, the octocopter starts moving upwards. To secure further upward moving, it is necessary to additionally increase angular speed of motors ($\omega_0 + \Delta\omega$), where $\Delta\omega \in (0, \Delta\omega_{max})$, meaning that an octocopter can change its vertical position depending on the value of $\Delta\omega$. The upper limit $\Delta\omega_{max}$ is selected such that the system does not either face nonlinearities caused by the Coriolis and gyroscopic effects or the speed saturation.

In case when the octocopter is not in an ideal horizontal position then the resulting generated force can be decomposed along X and Y axes into two non-zero components that cause the horizontal movement. The inclination from an ideal horizontal position and rotation around Z -axis can be generated by applying asymmetrical motor speeds which allow the octocopter movement in any desired direction. In the following subsections, we explain how the forces and motor speeds are generated to force the octocopter rotation around X , Y and Z axes.

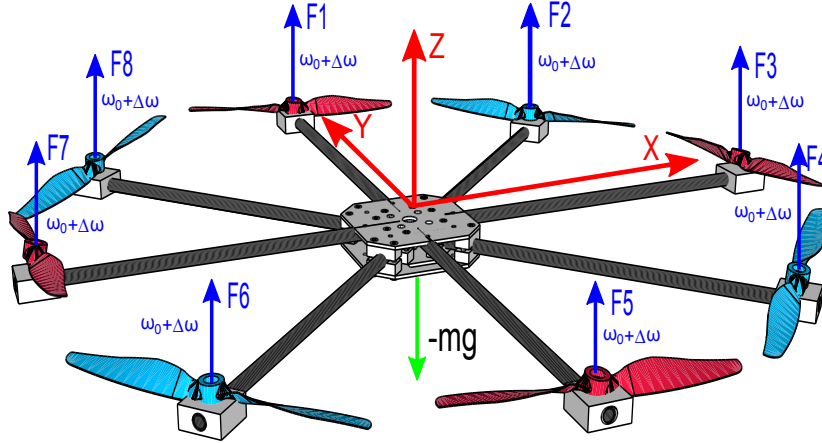
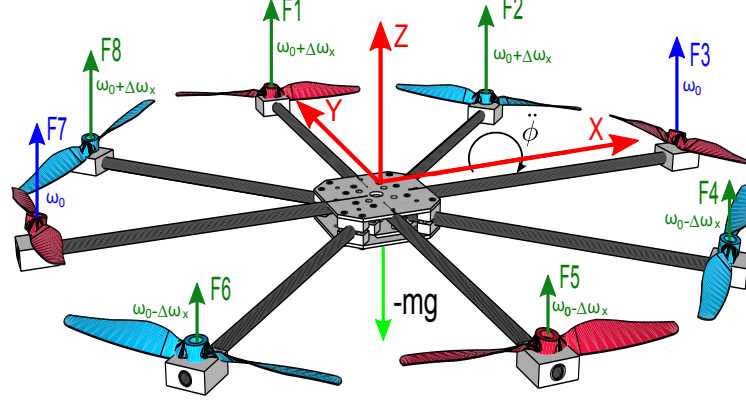


FIGURE 2.3

The forces that influence the movement of an octocopter system.

2.3 Roll

Rolling around X -axis (see Fig. 2.4) with an angle ϕ can be achieved by increasing the angular velocity of the DC motors M_1 , M_2 and M_8 for a value $\Delta\omega_x$, while decreasing the angular velocity of the DC motors M_4 , M_5 and M_6 for a value $\Delta\omega_x$ and maintaining the same angular velocity ω_0 of the remaining motors M_3 and M_7 . In this way, the intensity of generated forces $F_1 = F_2 = F_8$

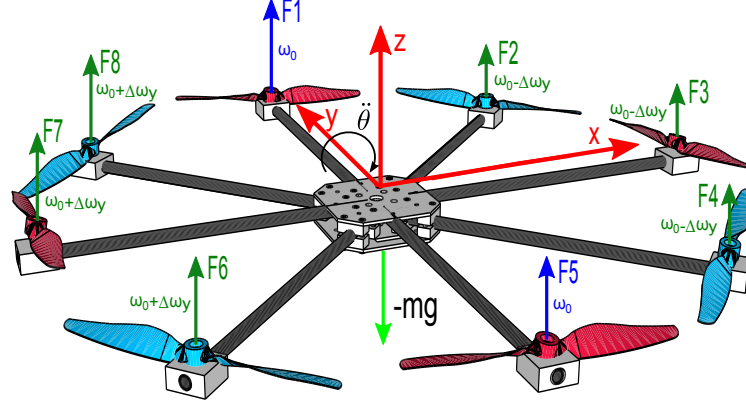
**FIGURE 2.4**

Distribution of the forces to ensure rotation of an octocopter system around X -axis of the local coordinate system.

are greater than the intensity of forces $F_3 = F_7$ and $F_4 = F_5 = F_6$. Having now $F_1 + F_2 + F_8 > F_4 + F_5 + F_6$ implies $\phi > 0$, i.e. a positive rotation of the octocopter around X -axis of the local coordinate system. It can be seen from Fig. 2.4 that the total sum of generated forces is still the same which preserves the same vertical octocopter position. It can also be noticed that there is a full balance between (F_2, F_3, F_4) and (F_6, F_7, F_8) , and between (F_2, F_4, F_6, F_8) and (F_1, F_3, F_5, F_7) , providing no additional rotations around Y -axis and Z -axis, respectively. However, in order to rotate an octocopter system only around X -axis but in the opposite direction, one should secure $F_1 + F_2 + F_8 < F_4 + F_5 + F_6$ while preserving $F_3 = F_7$.

2.4 Pitch

Pitching around Y -axis (see Fig. 2.5) with an angle θ can be achieved by increasing the angular velocity of the DC motors M_6 , M_7 and M_8 for a value $\Delta\omega_x$, while decreasing the angular velocity of the DC motors M_2 , M_3 and M_4 for a value $\Delta\omega_x$ and maintaining the same angular velocity of the remaining DC motors M_1 and M_5 . In this way, the intensity of generated forces $F_6 = F_7 = F_8$ are greater than the intensity of forces $F_1 = F_5$ and $F_2 = F_3 = F_4$. Having now $F_6 + F_7 + F_8 > F_2 + F_3 + F_4$ implies $\theta > 0$, i.e. a positive rotation of the octocopter around Y -axis. It can be seen from Fig. 2.5 that the total sum of generated forces is still the same which preserves the same vertical octocopter position. It can also be noticed that there is a full balance between (F_1, F_2, F_8) and (F_4, F_5, F_6) , and between (F_2, F_4, F_6, F_8) and (F_1, F_3, F_5, F_7) , providing

**FIGURE 2.5**

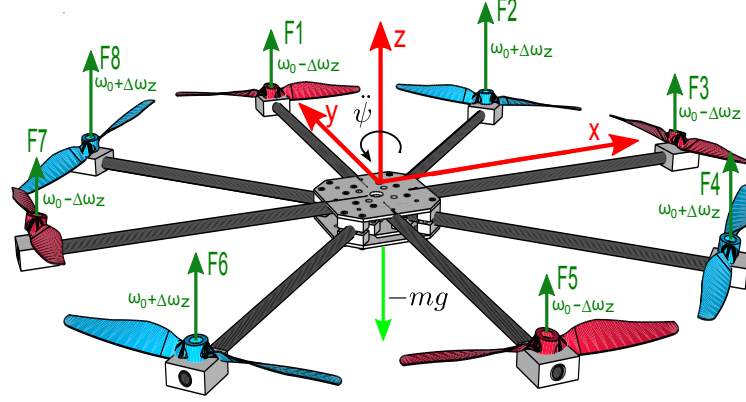
Distribution of the forces to ensure rotation of an octocopter system around Y -axis of the local coordinate system.

no additional rotations around X -axis and Z -axis, respectively. However, in order to rotate an octocopter system only around Y -axis but in the opposite direction, one should secure $F_6 + F_7 + F_8 < F_2 + F_3 + F_4$ while preserving $F_1 = F_5$.

2.5 Yaw

Yawing around Z -axis (see Fig. 2.6) with an angle ψ can be achieved by increasing the angular velocity of the DC motors M_2 , M_4 , M_6 and M_8 for a value $\Delta\omega_x$, while decreasing the angular velocity of the DC motors M_1 , M_3 , M_5 and M_7 for a value $\Delta\omega_x$. In this way, the intensity of generated forces $F_2 = F_4 = F_6 = F_8$ over the P type of rotors are greater than the intensity of forces $F_1 = F_3 = F_5 = F_7$ over the N type of rotors. This imbalance implies $\psi > 0$, i.e. a positive rotation of the octocopter around Z -axis. It can be seen from Fig. 2.6 that the total sum of generated forces is still the same which preserves the same vertical octocopter position. It can also be noticed that there is a full balance between (F_1, F_2, F_8) and (F_4, F_5, F_6) , and between (F_2, F_3, F_4) and (F_6, F_7, F_8) , providing no additional rotations around X -axis and Y -axis, respectively. However, in order to rotate an octocopter system only around Z -axis but in the opposite direction, one should apply the opposite logic with respect to P and N types of rotors.

Now, it is possible to describe the octocopter system motion towards a given reference point in space, as illustrated in the following subsections.

**FIGURE 2.6**

Distribution of the forces to ensure rotation of an octocopter system around Z-axis of the local coordinate system.

2.6 Frames of reference

The octocopter system based on the PNPNPNP configuration design, its body (local) and ground (global) fixed frames are shown in Fig. 2.7. As earlier stated, each motor and its associated propeller included in the octocopter design is mounted on an arm of length l . The adjacent arms are equally distant from each other by 45° , that is $(360^\circ/n)$, where $n = 8$ is the total number of motors.

Two reference frames are used to derive the model, one for a local coordinate system $\{o\}$ attached to the octocopter system and one representing a global coordinate system $\{g\}$ fixed to the ground. For $\{g\}$, the ENU convention is used to represent the axes, meaning that the axes X_B , Y_B and Z_B are pointing to the north, east and up, where $\mathbf{x} = [x \ y \ z]^T$ and $\mathbf{\Psi} = [\phi \ \theta \ \psi]^T$ indicate the position and the Euler-based orientation. The linear velocity $\mathbf{v} = [u \ v \ w]^T$ and the angular velocity $\mathbf{P} = [P \ Q \ R]^T$ are represented in $\{o\}$. The positive directions of ϕ , θ and ψ are chosen to coincide with the positive directions of P , Q and R , respectively.

Rotations around the axes of the local coordinate system in terms of minimal representation can be described by the Euler angles ϕ , θ and ψ which are also known as roll, pitch and yaw, respectively. These are elementary rotations

and can be expressed with the rotation matrices [72]:

$$\mathbf{R}(X, \phi) = \begin{bmatrix} 1 & 0 & 0 \\ 0 & c_\phi & -s_\phi \\ 0 & s_\phi & c_\phi \end{bmatrix}, \quad (2.1)$$

$$\mathbf{R}(Y, \theta) = \begin{bmatrix} c_\theta & 0 & s_\theta \\ 0 & 1 & 0 \\ -s_\theta & 0 & c_\theta \end{bmatrix}, \quad (2.2)$$

$$\mathbf{R}(Z, \psi) = \begin{bmatrix} c_\psi & -s_\psi & 0 \\ s_\psi & c_\psi & 0 \\ 0 & 0 & 1 \end{bmatrix}, \quad (2.3)$$

where the positive directions of the roll, pitch and yaw are defined by the right hand rule.

If we assume that the local and global coordinate systems are perfectly aligned for $(\phi, \theta, \psi) = (0, 0, 0)$, then any vector $\mathbf{p}^o = [p_x^o \ p_y^o \ p_z^o]^T$ given in the reference frame $\{o\}$ can be expressed in terms of the reference frame $\{g\}$ as a vector $\mathbf{p}^g = [p_x^g \ p_y^g \ p_z^g]^T$, that is

$$\mathbf{p}^g = \mathbf{R}_o^g \mathbf{p}^o, \quad (2.4)$$

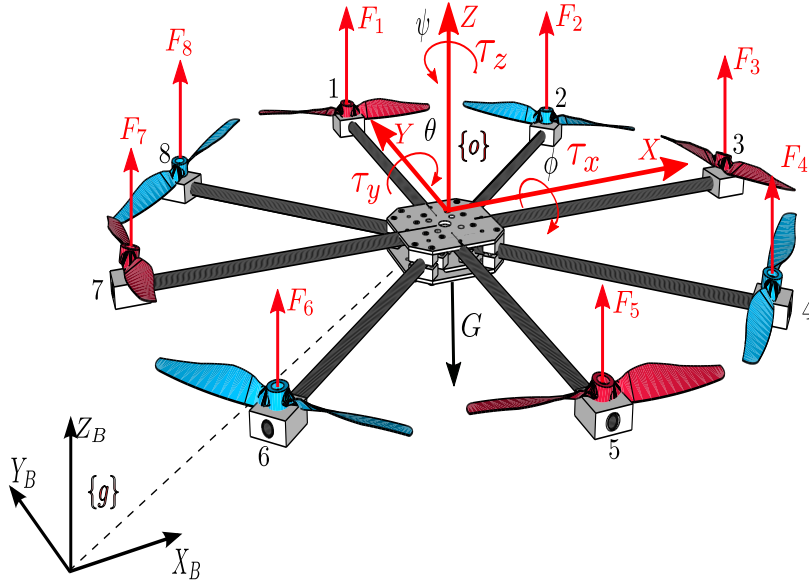


FIGURE 2.7

Body and ground fixed frames for a PNPNPNP octocopter system, where P and N indicate counter and clockwise directions depicted with blue and red colors respectively [59].

where \mathbf{R}_o^g is a rotation matrix describing the total rotation between the local and global coordinate systems. Finally, if we assume the ZYX convention then the rotation matrix is given by

$$\begin{aligned}\mathbf{R}_o^g &= \mathbf{R}(\phi, \theta, \psi) = \mathbf{R}(Z, \psi) \mathbf{R}(Y, \theta) \mathbf{R}(X, \phi) \\ &= \begin{bmatrix} c_\psi c_\theta & c_\psi s_\theta s_\phi - s_\psi c_\phi & c_\psi s_\theta c_\phi + s_\psi s_\phi \\ s_\psi c_\theta & s_\psi s_\theta s_\phi + c_\psi c_\phi & s_\psi s_\theta c_\phi - c_\psi s_\phi \\ -s_\theta & c_\theta s_\phi & c_\theta c_\phi \end{bmatrix}. \end{aligned} \quad (2.5)$$

2.7 Forces, moments and control inputs

The forces and torques acting on the system are shown in Fig. 2.7. There are only two types of forces acting on the system, i.e. thrust T and gravitational force G . Based on a static approximation, the motor thrust can be computed as follows [44]:

$$T = \sum_{i=1}^8 F_i = b \sum_{i=1}^8 \Omega_i^2, \quad (2.6)$$

where $b [Ns^2/rad^2]$ is the motor thrust constant, while $\Omega_i [rad/s]$ and $F_i [N]$ are the angular velocity and the thrust force associated with the i^{th} motor, respectively. If we denote the octocopter mass with m_o , then the gravitational force can be expressed as $G = m_o g$, where $g \approx 9.81 [m/s^2]$ is the gravitational acceleration of Earth. The thrust T acts along the Z direction of the local coordinate system and therefore can be written as the vector $\mathbf{T}^o = [0 \ 0 \ T]^T$, while the gravitational force G acts along the Z_B direction of the global coordinate system and can be written as the vector $\mathbf{G}^g = [0 \ 0 \ G]^T$.

Let the torques acting around the X , Y and Z axes of the local coordinate system be denoted as τ_x , τ_y and τ_z , respectively (see Fig. 2.7). Then, we assume that the distances from the octocopter center of mass from the center of mass of each single motor are equal and denoted by l . Now, the torques around the X and Y axes can be computed as:

$$\begin{aligned}
\tau_x &= l \left(F_1 + \frac{\sqrt{2}}{2} F_2 + \frac{\sqrt{2}}{2} F_8 - F_5 - \frac{\sqrt{2}}{2} F_4 - \frac{\sqrt{2}}{2} F_6 \right) \\
&= bl \left(\Omega_1^2 + \frac{\sqrt{2}}{2} \Omega_2^2 + \frac{\sqrt{2}}{2} \Omega_8^2 - \Omega_5^2 - \frac{\sqrt{2}}{2} \Omega_4^2 - \frac{\sqrt{2}}{2} \Omega_6^2 \right), \\
\tau_y &= l \left(F_7 + \frac{\sqrt{2}}{2} F_6 + \frac{\sqrt{2}}{2} F_8 - F_3 - \frac{\sqrt{2}}{2} F_2 - \frac{\sqrt{2}}{2} F_4 \right) \\
&= bl \left(\Omega_7^2 + \frac{\sqrt{2}}{2} \Omega_6^2 + \frac{\sqrt{2}}{2} \Omega_8^2 - \Omega_3^2 - \frac{\sqrt{2}}{2} \Omega_2^2 - \frac{\sqrt{2}}{2} \Omega_4^2 \right).
\end{aligned}$$

The angular motion of any motor included in the design causes a drag moment which is opposite to the direction of the motion according to Newton's third law. Therefore, if we also assume a static approximation of the drag [44], we can model the torque around the Z axis as

$$\begin{aligned}
\tau_z &= -M_1 + M_2 - M_3 + M_4 - M_5 + M_6 - M_7 + M_8 \\
&= d \left(-\Omega_1^2 + \Omega_2^2 - \Omega_3^2 + \Omega_4^2 - \Omega_5^2 + \Omega_6^2 - \Omega_7^2 + \Omega_8^2 \right), \quad (2.7)
\end{aligned}$$

where $d[Nms^2/rad^2]$ is the rotor drag constant and $M_i[Nm]$ ($i = \overline{1..8}$) is the drag moment of the i^{th} motor.

In an octocopter system, the algebraic sum

$$W_G = -\Omega_1 + \Omega_2 - \Omega_3 + \Omega_4 - \Omega_5 + \Omega_6 - \Omega_7 + \Omega_8 \quad (2.8)$$

of the angular velocities of all eight rotors is usually kept equal to zero. However, if $W_G \neq 0$ an additional moment M_g appears caused by gyroscopic effect.

Gyroscopic effect appears when the octocopter rotates around an axis (the spin axis in Fig. 2.8) during which there exist a force which is perpendicular to the plane of rotation causing the related moment along the input axis (Fig. 2.8). This results in a precession movement which rotates the octocopter around the output axis (Fig. 2.8).

The gyroscopic moment is proportional to the sum W_g [53] and can be written as

$$M_G = \omega \times \left(J_G \cdot \begin{bmatrix} 0 \\ 0 \\ \sum (-1)^i \cdot \Omega_i \end{bmatrix} \right) = \omega \times \begin{bmatrix} I_{XXm} & 0 & 0 \\ 0 & I_{YYm} & 0 \\ 0 & 0 & I_{ZZm} \end{bmatrix} \cdot \begin{bmatrix} 0 \\ 0 \\ \sum (-1)^i \cdot \Omega_i \end{bmatrix}, \quad (2.9)$$

where M_G , ω , J_G and Ω_i indicate the resulting moment, the octocopter angular velocity, the motor inertia and the rotational velocity of the motor M_i ,

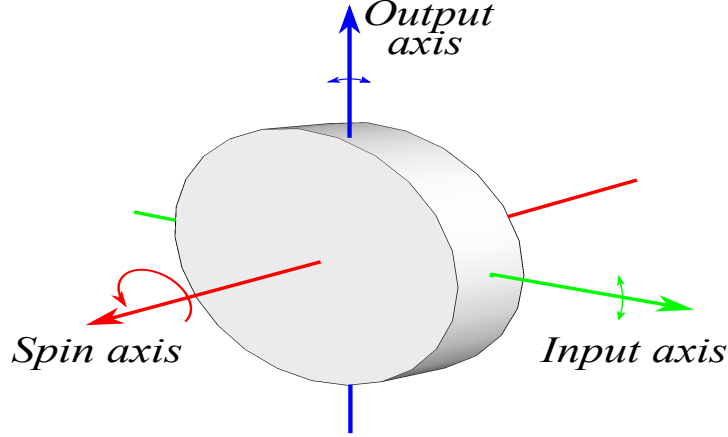


FIGURE 2.8
Gyroscopic effect.

respectively. Since $\omega = [P \ Q \ R]^T$, (2.9) can be written in a more compact form as

$$M_G = \begin{bmatrix} P \\ Q \\ R \end{bmatrix} \times \begin{bmatrix} 0 \\ 0 \\ I_{ZZm} \cdot W_G \end{bmatrix}. \quad (2.10)$$

If we now use the skew-symmetric vector operator $S(\cdot)$ (see, e.g. [73]) which transforms a vector $a = [a_1 \ a_2 \ a_3]^T$ into a skew-symmetric matrix

$$S(a) = -S^T(a) = \begin{bmatrix} 0 & -a_3 & a_2 \\ a_3 & 0 & -a_1 \\ -a_2 & a_1 & 0 \end{bmatrix}, \quad (2.11)$$

then the outer product (2.10) can be written as a matrix product

$$M_G = \begin{bmatrix} 0 & R & -Q \\ -R & 0 & P \\ Q & -P & 0 \end{bmatrix} \cdot \begin{bmatrix} 0 \\ 0 \\ I_{ZZm} \cdot W_G \end{bmatrix} = \begin{bmatrix} Q \cdot I_{ZZm} \cdot W_G \\ -P \cdot I_{ZZm} \cdot W_G \\ 0 \end{bmatrix}. \quad (2.12)$$

It should be noted that $M_g \neq 0$ only when the yawing and rolling occur simultaneously. However, the moment caused by gyroscopic effect can be often neglected in comparison to other moments and forces generated in the octocopter system. We also use a simplified rotor geometry as shown in Fig. 2.9 to derive the moment of inertia I_{zzm} . We assume that the rotor can be modelled as an infinitely thin rod ($R_p \rightarrow 0$) of length l_p and mass m_p . We also assume a unit transmission between the motor shaft and the rotor and neglect the moment of inertia of the motor shaft due to its relative small size with regard to the rotor geometry. Therefore, the inertia moment I_{zzm} is described

as [53]:

$$I_{zzm} = \frac{m_p l_p^2}{12}. \quad (2.13)$$

In order to control the octocopter system, we generate different thrust and torque values by changing the angular velocity of the rotors. Therefore, if we define the virtual control vector $\mathbf{u} = [T \ \boldsymbol{\tau}]^T = [T \ \tau_x \ \tau_y \ \tau_z]^T$ and the actuation matrix \mathbf{A} as:

$$\mathbf{A} = \begin{bmatrix} b & b & b & b & b & b & b & b \\ bl & \frac{\sqrt{2}}{2}bl & 0 & -\frac{\sqrt{2}}{2}bl & -bl & -\frac{\sqrt{2}}{2}bl & 0 & \frac{\sqrt{2}}{2}bl \\ 0 & -\frac{\sqrt{2}}{2}bl & -bl & -\frac{\sqrt{2}}{2}bl & 0 & \frac{\sqrt{2}}{2}bl & bl & \frac{\sqrt{2}}{2}bl \\ -d & d & -d & d & -d & d & -d & d \end{bmatrix},$$

the system actuation can be finally described as $\mathbf{u} = \mathbf{A}\boldsymbol{\Omega}_s$, where $\boldsymbol{\Omega}_s$ is the squared rotor velocity vector defined as:

$$\boldsymbol{\Omega}_s = [\Omega_1^2 \ \Omega_2^2 \ \Omega_3^2 \ \Omega_4^2 \ \Omega_5^2 \ \Omega_6^2 \ \Omega_7^2 \ \Omega_8^2]^T. \quad (2.14)$$

Consequently, the control inputs of the system are represented with the motor speeds $\Omega_1, \Omega_2, \Omega_3, \Omega_4, \Omega_5, \Omega_6, \Omega_7$ and Ω_8 . Changing the rotor velocity of the motors in range $0 \leq \Omega_i \leq \Omega_{max}$, $i = 1..8$, the different thrust force (T) and the torque (τ_x, τ_y and τ_z) about the x, y and z axes can be achieved.

In order to control the octocopter using rotor angular velocities as input variables, it is necessary to understand all forces that act on the system. Since each motor can have different angular velocity, different forces F_i ($i = 1, \dots, 8$) directed along positive direction of Z -axis and moments τ_x, τ_y, τ_z with respect to all three axes, X, Y , and Z can be generated. Every generated force is proportional to the square of angular velocity, that is

$$F_i = b \cdot \Omega_i^2, \quad (2.15)$$

where the coefficient b can be experimentally found for each type of propellers.

Alongside with the generated forces F_i , the gravitational force also acts on the system which is balanced with the thrust force generated with the rotor movements, where the thrust force can be computed as

$$T = \sum_{i=1}^8 F_i = \sum_{i=1}^8 b \cdot \Omega_i^2 = b \cdot (\Omega_1^2 + \Omega_2^2 + \Omega_3^2 + \Omega_4^2 + \Omega_5^2 + \Omega_6^2 + \Omega_7^2 + \Omega_8^2). \quad (2.16)$$

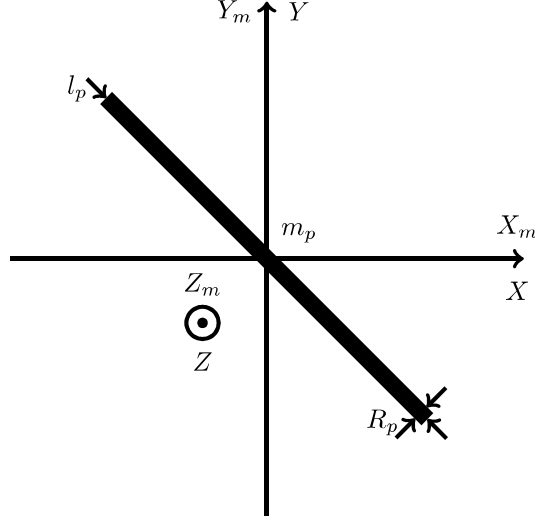


FIGURE 2.9
Simplified rotor geometry.

2.8 Octocopter kinematics

Let the linear velocities along the X , Y and Z axes of the local coordinate system be denoted as u , v and w , respectively. Let also the linear velocities along the X_B , Y_B and Z_B axes of the global coordinate system be denoted as \dot{x} , \dot{y} and \dot{z} , respectively. By rewriting these velocities in a vector form as $\mathbf{v}^o = \mathbf{v} = [u \ v \ w]^T$ and $\dot{\mathbf{x}}^g = \dot{\mathbf{x}} = [\dot{x} \ \dot{y} \ \dot{z}]^T$, we can directly apply the rotation matrix R_o^g to derive the kinematic model of the linear motion as

$$\dot{\mathbf{x}} = \mathbf{R}(\phi, \theta, \psi) \mathbf{v}. \quad (2.17)$$

The derivation of the kinematic model of the angular motion is also straightforward but it has some subtleties that need to be discussed. First, let the angular velocities around the X , Y and Z axes of the local coordinate system be denoted as P , Q and R , respectively. Recall that the total rotation of the local coordinate system with respect to the global coordinate system can be expressed in terms of the Euler angles ϕ , θ and ψ . By calculating the derivative of the Euler angles, we get the rotational velocities $\dot{\phi}$, $\dot{\theta}$ and $\dot{\psi}$, which in general do not have a physical interpretation. If we rewrite the angular velocities in the vector form as $\mathbf{P}^o = \mathbf{P} = [P \ Q \ R]^T$ and the rotational velocities in the vector form as $\dot{\mathbf{\Psi}} = [\dot{\phi} \ \dot{\theta} \ \dot{\psi}]^T$, then we can calculate the contributions of each rotational velocity component to the angular velocity

components as [72]:

$$\begin{aligned}
\mathbf{P} &= (\mathbf{R}(Z, \psi) \mathbf{R}(Y, \theta) \mathbf{R}(X, \phi))^{-1} \begin{bmatrix} 0 \\ 0 \\ \dot{\psi} \end{bmatrix} + \\
&\quad (\mathbf{R}(Y, \theta) \mathbf{R}(X, \phi))^{-1} \begin{bmatrix} 0 \\ \dot{\theta} \\ 0 \end{bmatrix} + \mathbf{R}^{-1}(X, \phi) \begin{bmatrix} \dot{\phi} \\ 0 \\ 0 \end{bmatrix} \\
&= \mathbf{R}_A(\phi, \theta, \psi) \begin{bmatrix} \dot{\phi} \\ \dot{\theta} \\ \dot{\psi} \end{bmatrix} = \mathbf{R}_A(\phi, \theta, \psi) \dot{\Psi},
\end{aligned} \tag{2.18}$$

where $\mathbf{R}_A(\phi, \theta, \psi)$ is defined as

$$\mathbf{R}_A(\phi, \theta, \psi) = \begin{bmatrix} 1 & 0 & -s_\theta \\ 0 & c_\phi & s_\phi c_\theta \\ 0 & -s_\phi & c_\phi c_\theta \end{bmatrix}. \tag{2.19}$$

By calculating the determinant of $\mathbf{R}_A(\phi, \theta, \psi)$, it can be shown that the inverse mapping is singular for $c_\theta = 0$, which yields $\theta = \pm \frac{\pi}{2}$ to be singular configurations. In real world applications, we measure the angular velocities P , Q and R with inertial measurement units (IMU) and try to estimate the Euler angles, therefore the inverse mapping

$$\dot{\Psi} = \mathbf{R}_A^{-1}(\phi, \theta, \psi) \mathbf{P}, \tag{2.20}$$

is more useful, where the matrix $\mathbf{R}_A^{-1}(\phi, \theta, \psi)$ is defined as

$$\mathbf{R}_A^{-1}(\phi, \theta, \psi) = \begin{bmatrix} 1 & s_\phi t_\theta & c_\phi t_\theta \\ 0 & c_\phi & -s_\phi \\ 0 & \frac{s_\phi}{c_\theta} & \frac{c_\phi}{c_\theta} \end{bmatrix}. \tag{2.21}$$

2.9 Octocopter dynamics

In order to derive the dynamical model of the linear motion, we apply Newton's third law in the form

$$\mathbf{F}_{\text{net}}^o = m_o \dot{\mathbf{v}}_{\text{net}}^o, \tag{2.22}$$

where $\mathbf{F}_{\text{net}}^o$ is the net force acting on the system and $\dot{\mathbf{v}}_{\text{net}}^o$ is the net linear acceleration of the system with respect to the local reference frame $\{o\}$. The

net force is the sum of the thrust and the gravitational force expressed in the local coordinate system, therefore we can write

$$\mathbf{F}_{\text{net}}^o = \mathbf{T}^o + \mathbf{G}^o = \mathbf{T}^o + (\mathbf{R}_g^o)^{-1} \mathbf{G}^g = \quad (2.23)$$

$$\begin{aligned} &= \mathbf{T}^o + (\mathbf{R}(Z, \psi) \mathbf{R}(Y, \theta) \mathbf{R}(X, \phi))^{-1} \mathbf{G}^g \\ &= \begin{bmatrix} 0 \\ 0 \\ T \end{bmatrix} + m_o g \begin{bmatrix} s_\theta \\ -s_\phi c_\theta \\ -c_\phi c_\theta \end{bmatrix}. \end{aligned} \quad (2.24)$$

Given that $\{o\}$ is a non-inertial reference frame, the net acceleration is calculated as [26]:

$$\dot{\mathbf{v}}_{\text{net}}^o = \dot{\mathbf{v}}^o + \mathbf{P}^o \times \mathbf{v}^o = \dot{\mathbf{v}} + \mathbf{P} \times \mathbf{v} = \dot{\mathbf{v}} + \mathbf{S} \mathbf{v}, \quad (2.25)$$

where \mathbf{S} is a skew-symmetric matrix defined as [72]:

$$\mathbf{S} = \begin{bmatrix} 0 & -R & Q \\ R & 0 & -P \\ -Q & P & 0 \end{bmatrix}. \quad (2.26)$$

The resulting linear motion dynamics, obtained by combining the equations (2.22), (2.24) and (2.25), can be written in the form

$$\dot{\mathbf{v}} = \frac{\mathbf{F}^o}{m_o} - \mathbf{S} \mathbf{v} = \begin{bmatrix} 0 \\ 0 \\ \frac{T}{m_o} \end{bmatrix} + g \begin{bmatrix} s_\theta \\ -s_\phi c_\theta \\ -c_\phi c_\theta \end{bmatrix} - \mathbf{S} \mathbf{v}. \quad (2.27)$$

In the same manner, to derive the dynamic model of the angular motion we apply Newton's third law in the form

$$\boldsymbol{\tau}_{\text{net}}^o = \mathbf{J} \dot{\boldsymbol{\omega}}_{\text{net}}^o, \quad (2.28)$$

where $\boldsymbol{\tau}_{\text{net}}^o$ is the net torque acting on the system and $\dot{\boldsymbol{\omega}}_{\text{net}}^o$ is the net angular acceleration of the system with respect to the reference frame $\{o\}$. \mathbf{J} is the inertia tensor of the octocopter and, based on the fact that X , Y and Z are principle axes of inertia, can be written in the form:

$$\mathbf{J} = \begin{bmatrix} I_{xx} & 0 & 0 \\ 0 & I_{yy} & 0 \\ 0 & 0 & I_{zz} \end{bmatrix}, \quad (2.29)$$

where I_{xx} , I_{yy} and I_{zz} are the moments of inertia around the X , Y and Z axes, respectively. The net torque acting on the system is described by $\boldsymbol{\tau}_{\text{net}}^o = \boldsymbol{\tau}$ and the net angular acceleration is given as [26]:

$$\begin{aligned} \dot{\boldsymbol{\omega}}_{\text{net}}^o &= \dot{\mathbf{P}}^o + \mathbf{J}^{-1} \mathbf{P}^o \times \mathbf{J} \mathbf{P}^o = \dot{\mathbf{P}} + \mathbf{J}^{-1} \mathbf{P} \times \mathbf{J} \mathbf{P} \\ &= \dot{\mathbf{P}} + \mathbf{J}^{-1} \mathbf{S} \mathbf{J} \mathbf{P}. \end{aligned} \quad (2.30)$$

The resulting angular motion dynamics can be obtained by combining the equations (2.28) and (2.30) and can be written as

$$\dot{\mathbf{P}} = \mathbf{J}^{-1} (\boldsymbol{\tau} - \mathbf{SJP}). \quad (2.31)$$

If we also want to include the Gyroscopic effect into the dynamic model of the angular motion, we have to add the gyroscopic term [31]

$$-\mathbf{P} \times \mathbf{J}_m \begin{bmatrix} 0 \\ 0 \\ W_g \end{bmatrix}, \quad (2.32)$$

where W_g is the difference of the rotor velocities given as (2.8) and \mathbf{J}_m is the inertia tensor of the rotors given as

$$\mathbf{J}_m = \begin{bmatrix} I_{xxm} & 0 & 0 \\ 0 & I_{yy m} & 0 \\ 0 & 0 & I_{zzm} \end{bmatrix}. \quad (2.33)$$

The I_{xxm} , $I_{yy m}$ and I_{zzm} are the moments of inertia around the axes of the rotor reference frame. The gyroscopic term can be simplified to

$$-\mathbf{P} \times \mathbf{J}_m \begin{bmatrix} 0 \\ 0 \\ W_g \end{bmatrix} = -\mathbf{S} \begin{bmatrix} 0 \\ 0 \\ I_{zzm} W_g \end{bmatrix}, \quad (2.34)$$

and finally, in order to include Gyroscopic effect, the angular motion dynamics can be rewritten as

$$\dot{\mathbf{P}} = \mathbf{J}^{-1} \left(\boldsymbol{\tau} - \mathbf{SJP} - \mathbf{S} \begin{bmatrix} 0 \\ 0 \\ I_{zzm} W_g \end{bmatrix} \right). \quad (2.35)$$

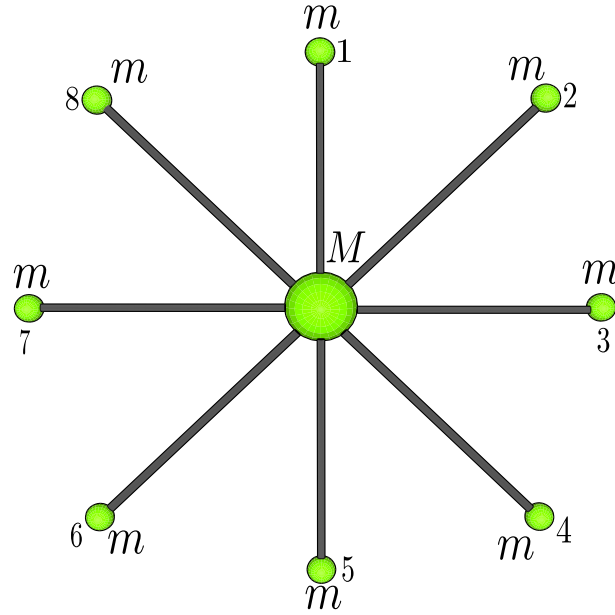
In order to model the inertia moments I_{xx} , I_{yy} and I_{zz} we use the parallel axis theorem (also called Huygens–Steiner theorem) [53]. We assume a simplified octocopter configuration structure as shown in Fig. 2.10, where the motors are particles with mass m , the support plate with the mounted hardware is a solid sphere of radius r and mass M , while the mass of the rotors is considered negligible.

Therefore, the inertia moments I_{xx} and I_{yy} are given as

$$\begin{aligned} I_{xx} = I_{yy} &= \frac{2Mr^2}{5} + 2ml^2 + 4 \left(\frac{\sqrt{2}}{2} l \right)^2 \\ &= \frac{2Mr^2}{5} + 4ml^2, \end{aligned} \quad (2.36)$$

while the inertia moment I_{zz} is given by

$$I_{zz} = \frac{2Mr^2}{5} + 8ml^2. \quad (2.37)$$

**FIGURE 2.10**

A simplified octocopter configuration structure.

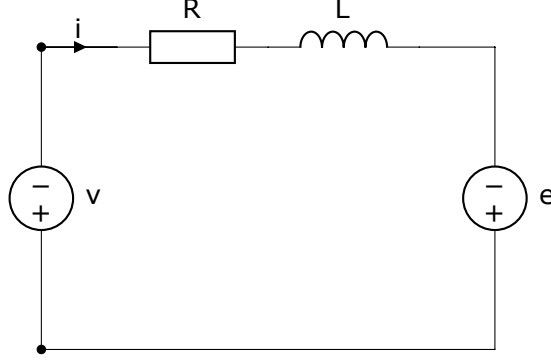
2.10 Motor dynamics

The actuator used to drive propellers mounted on an octocopter system (or any other MAV) is usually a DC motor which can be modelled with (2.38) and represented in Fig. 2.11

$$v = Ri + L \frac{di}{dt} + e, \quad (2.38)$$

where R is the resistance and L is the inductance of the motor windings, while v is the voltage applied to the motor, i is the motor current and e is the counter-electromotive force induced into the motor windings. This can be simplified to the algebraic model $v = Ri + e$ if we neglect inductive losses of the motor armature. This is a reasonable assumption based on the fact that DC motors used in robotics are in general constructed to minimize the inductive losses. We can rewrite the counter-electromotive force as $e = K_e \Omega$, where K_e [Vs/rad] is the so-called electrical motor constant and Ω is the angular velocity of the motor (which is in our case also the angular velocity of the rotor). Therefore, the electrical model of the motor can be written in the form:

$$v = Ri + K_e \Omega. \quad (2.39)$$

**FIGURE 2.11**

Equivalent electric circuit of the armature.

The dynamic model of the rotor angular motion can be obtained by applying Newton's second law [26] in the form:

$$I_{zzm}\dot{\Omega} = \tau_m - \tau_l, \quad (2.40)$$

where I_{zzm} is moment of inertia of the motor, τ_m and τ_l are the motor and load torque, respectively. We can rewrite the motor torque as $\tau_m = K_m i$, where K_m [Nm/A] is the so-called mechanical motor constant. The resulting motor dynamics can be obtained by combining (2.39) i (2.40) with the previously defined motor torque term τ_m in the form

$$I_{zzm}\dot{\Omega} + \frac{K_m K_e}{R}\Omega = \frac{K_m}{R}v - \tau_l. \quad (2.41)$$

By treating the DC motor as an isolated system and writing out the power balance equations, it is possible to show that the electrical and mechanical motor constants have the same numeric values given in different units. Another subtlety we need to include in the model is the motor voltage saturation given as $0 \leq v \leq v_{\max}$.

Finally, assuming that all motors have the same parameter values J_m , K_m , K_e i R , we can model the octocopter motor dynamics as

$$I_{zzm}\dot{\Omega}_i + \frac{K_m K_e}{R}\Omega_i = \frac{K_m}{R}v_i - \tau_{li}, \quad i = \overline{1..8}, \quad (2.42)$$

where the load torque is the drag moment given as

$$\tau_{li} = d\Omega_i^2, \quad i = \overline{1..8}, \quad (2.43)$$

and d being the rotor drag constant.

2.11 State space model

In this section we provide the complete state space model of an octocopter which includes linear and angular velocities with respect to the local coordinate system, (u, v, w) and (P, Q, R) , Euler angles ϕ, θ, ψ and the octocopter position (x, y, z) with respect to the global reference system.

The resulting force F^o which acts on the octocopter consists of the gravitational force F_G^B presented in the global coordinate system and the thrust which is generated as a sum of all forces caused by rotation of motors, that is

$$F^o = F_G^B + T.$$

From (2.27), one can obtain

$$\dot{v} = -Sv + \frac{F_G^B}{m} + \frac{T}{m}, \quad (2.44)$$

which can be written in the form

$$\begin{bmatrix} \dot{u} \\ \dot{v} \\ \dot{w} \end{bmatrix} = - \begin{bmatrix} 0 & -R & Q \\ R & 0 & -P \\ -Q & P & 0 \end{bmatrix} \cdot \begin{bmatrix} u \\ v \\ w \end{bmatrix} + \begin{bmatrix} g \cdot s_\theta \\ -g \cdot c_\theta \cdot s_\phi \\ -g \cdot c_\theta \cdot c_\phi \end{bmatrix} + \frac{1}{m} \begin{bmatrix} F_x \\ F_y \\ F_z \end{bmatrix}. \quad (2.45)$$

If we assume that the thrust force acts only along the direction of Z -axis, it yields

$$\begin{bmatrix} \dot{u} \\ \dot{v} \\ \dot{w} \end{bmatrix} = - \begin{bmatrix} 0 & R & -Q \\ -R & 0 & P \\ Q & -P & 0 \end{bmatrix} \cdot \begin{bmatrix} u \\ v \\ w \end{bmatrix} + \begin{bmatrix} g \cdot s_\theta \\ -g \cdot c_\theta \cdot s_\phi \\ -g \cdot c_\theta \cdot c_\phi \end{bmatrix} + \begin{bmatrix} 0 \\ 0 \\ \frac{F_z}{m} \end{bmatrix}, \quad (2.46)$$

that is

$$\begin{bmatrix} \dot{u} \\ \dot{v} \\ \dot{w} \end{bmatrix} = \begin{bmatrix} R \cdot v - Q \cdot w \\ P \cdot w - R \cdot u \\ Q \cdot u - P \cdot v \end{bmatrix} + \begin{bmatrix} g \cdot s_\theta \\ -g \cdot c_\theta \cdot s_\phi \\ -g \cdot c_\theta \cdot c_\phi \end{bmatrix} + \begin{bmatrix} 0 \\ 0 \\ \frac{T}{m} \end{bmatrix}. \quad (2.47)$$

From (2.35), one can obtain

$$\dot{P} = J^{-1}(\tau - SJP). \quad (2.48)$$

that is

$$\begin{bmatrix} \dot{P} \\ \dot{Q} \\ \dot{R} \end{bmatrix} = J^{-1} \cdot \left\{ \begin{bmatrix} 0 & R & -Q \\ -R & 0 & P \\ Q & -P & 0 \end{bmatrix} \cdot \begin{bmatrix} I_{xx} & 0 & 0 \\ 0 & I_{yy} & 0 \\ 0 & 0 & I_{zz} \end{bmatrix} \cdot \begin{bmatrix} P \\ Q \\ R \end{bmatrix} + \begin{bmatrix} \tau_x \\ \tau_y \\ \tau_z \end{bmatrix} \right\}, \quad (2.49)$$

which gives the form

$$\begin{aligned}
 \begin{bmatrix} \dot{P} \\ \dot{Q} \\ \dot{R} \end{bmatrix} &= \begin{bmatrix} I_{XX}^{-1} & 0 & 0 \\ 0 & I_{YY}^{-1} & 0 \\ 0 & 0 & I_{ZZ}^{-1} \end{bmatrix} \cdot \left\{ \begin{bmatrix} (I_{YY} - I_{ZZ}) \cdot QR \\ (I_{ZZ} - I_{XX}) \cdot PR \\ (I_{XX} - I_{YY}) \cdot PQ \end{bmatrix} + \begin{bmatrix} \tau_x \\ \tau_y \\ \tau_z \end{bmatrix} \right\} \\
 &= \begin{bmatrix} \frac{I_{YY} - I_{ZZ}}{I_{XX}} \cdot QR \\ \frac{I_{XX} - I_{ZZ}}{I_{YY}} \cdot PR \\ \frac{I_{YY} - I_{XX}}{I_{ZZ}} \cdot PQ \end{bmatrix} + \begin{bmatrix} \frac{\tau_x}{I_{XX}} \\ \frac{\tau_y}{I_{YY}} \\ \frac{\tau_z}{I_{ZZ}} \end{bmatrix}.
 \end{aligned} \tag{2.50}$$

Furthermore, from (2.4) which indicates the relation between Euler angles and angular velocities, one obtains

$$\begin{aligned}
 \dot{\phi} &= P + s_\phi \cdot t_\theta \cdot Q + c_\phi \cdot t_\theta \cdot R \\
 \dot{\theta} &= c \cdot Q - s_\phi \cdot R \\
 \dot{\psi} &= \frac{s_\phi}{c_\theta} \cdot Q + \frac{c_\phi}{c_\theta} \cdot R,
 \end{aligned} \tag{2.51}$$

providing the relations between the time derivatives of Euler angles from which one can compute the system orientation ϕ, θ, ψ at each time instant.

Finally, by taking into account the previously derived relations (2.17) and (2.19) one obtains the full state space model of the octocopter system as follows

$$\begin{aligned}
 \dot{x} &= c_\theta \cdot c_\psi \cdot u + (s_\phi \cdot s_\theta \cdot c_\psi - c_\phi \cdot s_\psi) \cdot v + (c_\phi \cdot s_\phi \cdot c_\psi + s_\phi \cdot s_\psi) \cdot w \\
 \dot{y} &= c_\theta \cdot s_\psi \cdot u + (s_\phi \cdot s_\theta \cdot s_\psi + c_\phi \cdot c_\psi) \cdot v + (c_\phi \cdot s_\phi \cdot s_\psi - s_\phi \cdot c_\psi) \cdot w \\
 \dot{z} &= -s_\theta \cdot u + c_\theta \cdot s_\phi \cdot v + c_\theta \cdot c_\phi \cdot w \\
 \dot{u} &= R \cdot v - Q \cdot w + g \cdot s_\theta \\
 \dot{v} &= P \cdot w - R \cdot u - g \cdot c_\theta \cdot s_\phi \\
 \dot{w} &= Q \cdot u - P \cdot v - g \cdot c_\theta \cdot c_\phi + \frac{T}{m} \\
 \dot{P} &= \frac{I_{YY} - I_{ZZ}}{I_{XX}} \cdot Q \cdot R + \frac{\tau_x}{I_{XX}} - \frac{I_{ZZM}}{I_{XX}} \cdot Q \cdot W_G \\
 \dot{Q} &= \frac{I_{XX} - I_{ZZ}}{I_{YY}} \cdot P \cdot R + \frac{I_{XX}}{I_{YY}} + \frac{I_{ZZM}}{I_{YY}} \cdot P \cdot W_G \\
 \dot{R} &= \frac{I_{YY} - I_{XX}}{I_{ZZ}} \cdot P \cdot Q + \frac{\tau_z}{I_{ZZ}} \\
 \dot{\phi} &= P + Q \cdot s_\phi \cdot t_\theta + R \cdot c_\phi \cdot t_\theta \\
 \dot{\theta} &= Q \cdot c_\phi - R \cdot s_\phi \\
 \dot{\psi} &= Q \cdot \frac{s_\phi}{c_\theta} + R \cdot \frac{c_\phi}{c_\theta}
 \end{aligned} \tag{2.52}$$

3

Control

CONTENTS

3.1	Relevant background work	25
3.2	Motor Controller	26
3.3	Control allocation algorithm	30
3.4	Linearized model	32
3.5	Altitude control near equilibrium	34
3.6	Orientation control near equilibrium	35
3.7	Position control near equilibrium	37
3.8	Overall UAV control architecture	40
3.9	RLS-based fault tolerant control	42
3.9.1	Fault-tolerant PD tracking control	42
3.9.2	Simulation results for Fault-tolerant PD tracking control	47

This chapter describes the control architecture for tracking reference trajectories. The architecture comprises position and orientation controllers, control allocation algorithm, and motor speed controllers. To facilitate the control design, a nonlinear mathematical model of the multi-rotor craft is linearized with respect to equilibrium point. The resulting controllers enable satisfactory tracking of reference trajectories. In the remainder of the chapter, a tracking controller based on the architecture from [44] and a simple PD control law is designed. Despite its simplicity, the control system is able to track considerably complex reference trajectories. Moreover, the considered UAV system may be equipped with additional actuators and hence the capacity to continue the mission. However, a mechanism for fault detection is also necessary, together with the suitable control system capable of utilizing the information about the fault state occurrence, in terms of its location and severity. This information should be used, if possible, to mitigate the consequences caused by the fault state. To this end, this chapter also presents some relevant aspects of fault-tolerant control.

3.1 Relevant background work

First controllers designed for the purpose of multi-rotor UAV are proposed in the aforementioned PhD dissertation of Samir Bouabdallah [4], where the first fully autonomous quad-rotor craft has been developed. A simple stabilizing PID controller is designed, and it was shown that it was possible to perform the orientation stabilization. Based on results from [5], the author has compared the PID-based control with adaptive LQR-based controller, and shown that the former performs better. Continuing on his work on UAV control, he designed a backstepping-based controller, and a sliding-mode-based controller [6]. Remarkably, the backstepping control ensured better performance. It was argued that this was the consequence of switching nature of the sliding mode control that caused unwanted oscillations within UAV control. Beside the seminal work of Bouabdallah, the collaboration of Robert Mahony, Vijay Kumar and Peter Corke yielded several papers that attracted substantial attention and paved the path for further research in the field of UAV control. The methods proposed by the abovementioned authors have been validated both in simulated environment and on real UAVs. In [51], the results show the tracking of reference trajectories in laboratory-controlled conditions, whilst [69] and [70] demonstrate the validation in real-world indoor and outdoor environments. Soon after the first real-world validations, the controllers were developed capable of navigating UAVs in obstacle-filled environments and performing complex maneuvers [48], [44]. Further enhancements in multi-rotor UAV control can be found in the works of Mark W. Mueller and Raffaell D’Andrea, which enabled “aggressive” maneuvers [42]. For instance, in [57], the authors developed a quad-copter equipped with a tennis racket, along with a perception system with eight cameras. The system was able to predict the motion of the tennis ball, enabling the real-time trajectory planning for the UAV to timely place the racket and reflect the approaching ball. The same authors successfully showed that multiple UAVs can be coordinated for performing complex tasks [65], while in [55] it was shown that the craft can be controlled even in case when one or more rotors are in fault state.

3.2 Motor Controller

The motor dynamic model can be expressed with eq. (2.41)-(2.43). A robust multirotor motor control approach with respect to battery voltage changes can be found in [44] and is given by

$$v^{\text{des}} = K_{\Omega} (\Omega_{\text{ref}} - \Omega) + v_{\text{ff}}(\Omega_{\text{ref}}), \quad (3.1)$$

where Ω_{ref} is a constant referent velocity, $K_\Omega > 0$ is the proportional controller gain and $v_{\text{ff}}(\Omega_{\text{ref}})$ is the voltage feedforward term ensuring drag moment compensation at Ω_{ref} velocity. The feedforward term can be calculated from the static rotor drag characteristics either from a parametric approximation or a lookup table.

Assuming that the angular rotor velocity Ω achieved Ω_{ref} , eq. (2.41) can be expressed as

$$\frac{K_m K_e}{R} \Omega = \frac{K_m}{R} v - \tau_l. \quad (3.2)$$

If we now plug (2.43) into (3.2) and solve for the input voltage v , the feedforward term can be obtained in the form

$$v_{\text{ff}}(\Omega_{\text{ref}}) = K_e \Omega_{\text{ref}} + \frac{Rd}{K_m} \Omega_{\text{ref}}^2. \quad (3.3)$$

To derive the final model of the motor dynamics, eq. (2.41) can be written in the form

$$\dot{\Omega} = -\frac{K_m K_e}{I_{zzm} R} \Omega + \frac{K_m}{I_{zzm} R} v - \frac{\tau_l}{I_{zzm}} = f_\Omega(\Omega, v), \quad (3.4)$$

from which one can illustrate the use of the angular velocity controller K_Ω as in Fig. 3.1.

Fig. 3.2 indicates how well angular velocity is controlled using only proportional component for K_Ω . It can be seen that the output velocity Ω (red) tracks quickly the reference input Ω_{ref} (blue) and the transient phase is a bit longer when the reference input is larger. This occurs when the reference value is close to the velocity saturation of the motor. The controller gain ($K_\Omega = 2$) is selected to decrease the oscillations in the motor current and voltage, as shown respectively in Figs. 3.3 i 3.4, in order to prolong its life cycle.

If we now aim to apply a controller K_ω to an octocopter, it is necessary to define the vector consisting of all motor angular velocities

$$\mathbf{\Omega} = [\Omega_1 \quad \Omega_2 \quad \Omega_3 \quad \Omega_4 \quad \Omega_5 \quad \Omega_6 \quad \Omega_7 \quad \Omega_8]^T, \quad (3.5)$$

the reference vector for each single motor

$$\mathbf{\Omega}_{\text{ref}} = [\Omega_{\text{ref},1} \quad \Omega_{\text{ref},2} \quad \Omega_{\text{ref},3} \quad \Omega_{\text{ref},4} \quad \Omega_{\text{ref},5} \quad \Omega_{\text{ref},6} \quad \Omega_{\text{ref},7} \quad \Omega_{\text{ref},8}]^T, \quad (3.6)$$

the vector of control inputs

$$\mathbf{v} = [v_1 \quad v_2 \quad v_3 \quad v_4 \quad v_5 \quad v_6 \quad v_7 \quad v_8]^T, \quad (3.7)$$

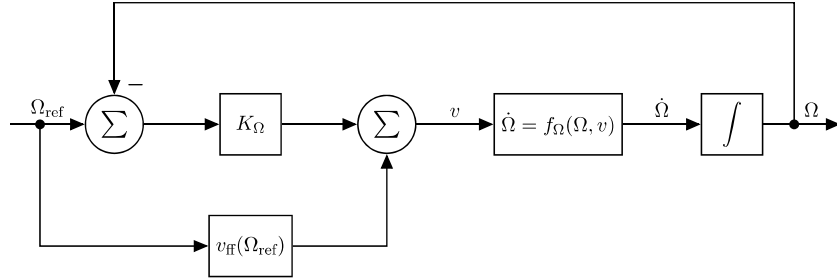


FIGURE 3.1
Motor speed control diagram .

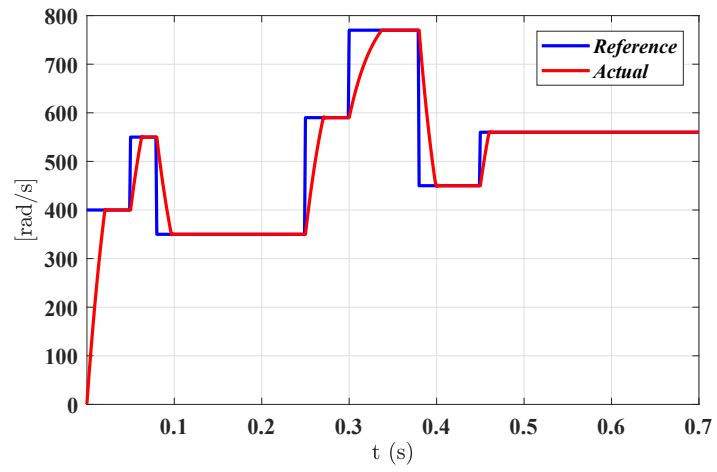


FIGURE 3.2
Motor speed tracking.

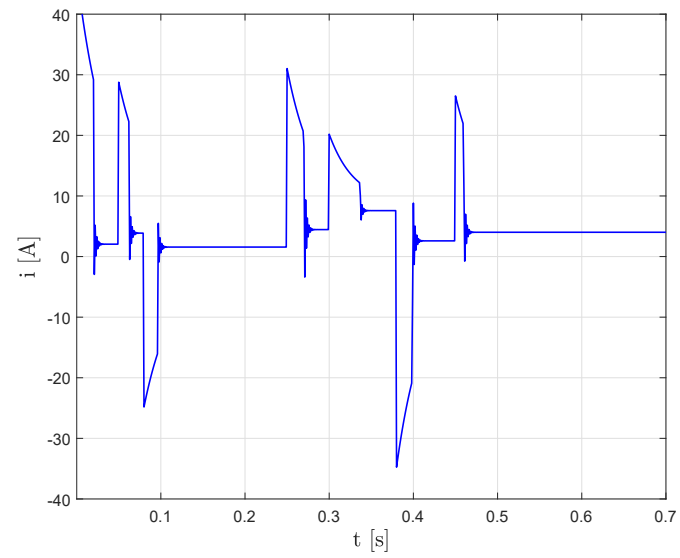


FIGURE 3.3
Time response of the armature current.

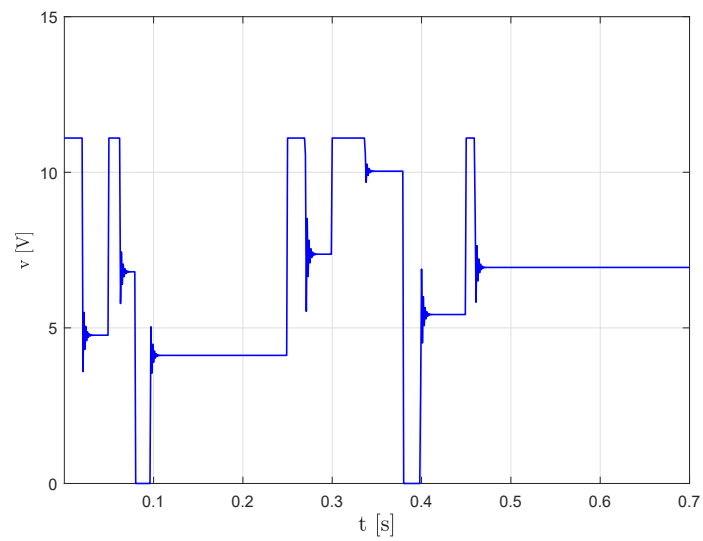


FIGURE 3.4
Time response of the armature voltage.

and the vector of feedforward terms as

$$\mathbf{v}_{\text{ff}}(\boldsymbol{\Omega}_{\text{ref}}) = \begin{bmatrix} v_{\text{ff}}(\Omega_{\text{ref},1}) \\ v_{\text{ff}}(\Omega_{\text{ref},2}) \\ v_{\text{ff}}(\Omega_{\text{ref},3}) \\ v_{\text{ff}}(\Omega_{\text{ref},4}) \\ v_{\text{ff}}(\Omega_{\text{ref},5}) \\ v_{\text{ff}}(\Omega_{\text{ref},6}) \\ v_{\text{ff}}(\Omega_{\text{ref},7}) \\ v_{\text{ff}}(\Omega_{\text{ref},8}) \end{bmatrix}. \quad (3.8)$$

In this case, the controller can be generalized using the form

$$\mathbf{v}^{\text{des}} = \mathbf{K}_{\Omega} (\boldsymbol{\Omega}_{\text{ref}} - \boldsymbol{\Omega}) + \mathbf{v}_{\text{ff}}(\boldsymbol{\Omega}_{\text{ref}}), \quad (3.9)$$

where \mathbf{K}_{Ω} is a diagonal matrix given as $\mathbf{K}_{\Omega} = K_{\Omega} \mathbf{I}_{8 \times 8}$. If we now describe the motor dynamic model using the following compact form

$$\mathbf{f}_{\Omega}(\boldsymbol{\Omega}, \mathbf{v}) = \begin{bmatrix} \dot{\Omega}_1 \\ \dot{\Omega}_2 \\ \dot{\Omega}_3 \\ \dot{\Omega}_4 \\ \dot{\Omega}_5 \\ \dot{\Omega}_6 \\ \dot{\Omega}_7 \\ \dot{\Omega}_8 \end{bmatrix} = \begin{bmatrix} f_{\Omega}(\Omega_1, v_1) \\ f_{\Omega}(\Omega_2, v_2) \\ f_{\Omega}(\Omega_3, v_3) \\ f_{\Omega}(\Omega_4, v_4) \\ f_{\Omega}(\Omega_5, v_5) \\ f_{\Omega}(\Omega_6, v_6) \\ f_{\Omega}(\Omega_7, v_7) \\ f_{\Omega}(\Omega_8, v_8) \end{bmatrix}, \quad (3.10)$$

then the vector of the angular velocity controllers can be illustrated as in Fig. 3.5.

3.3 Control allocation algorithm

The relation between the control inputs \mathbf{u} (the reference thrust force T and torques $\boldsymbol{\tau}$) and the rotation velocity $\boldsymbol{\Omega}_s$ of DC motors (see chapter 2) is given with:

$$\mathbf{u}_{\text{ref}} = \mathbf{A} \boldsymbol{\Omega}_s \quad (3.11)$$

where

$$\mathbf{u}_{\text{ref}} = [T \quad \boldsymbol{\tau}]^T = [T \quad \tau_x \quad \tau_y \quad \tau_z]^T, \quad (3.12)$$

\mathbf{A} being the system actuation matrix defined as:

$$\mathbf{A} = \begin{bmatrix} b & b & b & b & b & b & b & b \\ bl & \frac{\sqrt{2}}{2}bl & 0 & -\frac{\sqrt{2}}{2}bl & -bl & -\frac{\sqrt{2}}{2}bl & 0 & \frac{\sqrt{2}}{2}bl \\ 0 & -\frac{\sqrt{2}}{2}bl & -bl & -\frac{\sqrt{2}}{2}bl & 0 & \frac{\sqrt{2}}{2}bl & bl & \frac{\sqrt{2}}{2}bl \\ -d & \frac{2}{d} & -d & \frac{2}{d} & -d & \frac{2}{d} & -d & \frac{2}{d} \end{bmatrix}, \quad (3.13)$$

while $\boldsymbol{\Omega}_s \in D_{\Omega_s} \subset \mathbb{R}^8$ represents the squared rotor velocity vector given as

$$\boldsymbol{\Omega}_s = [\Omega_1^2 \quad \Omega_2^2 \quad \Omega_3^2 \quad \Omega_4^2 \quad \Omega_5^2 \quad \Omega_6^2 \quad \Omega_7^2 \quad \Omega_8^2]^T. \quad (3.14)$$

$\mathbf{u} \in D_u \subset \mathbb{R}^4$ is a surjective (onto) mapping $D_{\Omega_s} \mapsto D_u$ implying that multiple $\boldsymbol{\Omega}_s$ values map to the same \mathbf{u} value. Consequently, the so-called control allocation problem given by the inverse mapping $D_u \mapsto D_{\Omega_s}$ does not have a unique solution. Due to the motor voltage constraints, the set D_{Ω_s} is defined based on the squared rotor velocity constraints:

$$0 \leq \Omega_i^2 \leq \Omega_{\max}^2, \quad i = \overline{1..8}. \quad (3.15)$$

Assuming that the DC motor velocity is limited between 0 and ω_{max} (3.15) and the mapping is defined by the linear relation (3.11), it means that the set D_u represents a polytope in space \mathbb{R}^4 due to the linear actuation in conjunction with the box constrained inputs. Another interesting subtlety that arises due to the decentralized control approach is that the altitude and attitude controllers can generate desired control input values $\mathbf{u}^{\text{des}} \notin D_u$ that may cause actuator saturation.

An extensive survey on algorithms that are used to solve the control allocation problem is considered in [31]. For simplicity, we introduce the equality constraints

$$\Omega_1 = \Omega_3, \quad \Omega_2 = \Omega_4, \quad \Omega_5 = \Omega_7, \quad \Omega_6 = \Omega_8, \quad (3.16)$$

and therefore reduce the actuation matrix \mathbf{A} to its square (invertible) form

$$\mathbf{A}_f = \begin{bmatrix} 2b & 2b & 2b & 2b \\ bl & 0 & -bl & 0 \\ -bl & -\sqrt{2}bl & bl & \sqrt{2}bl \\ -2d & 2d & -2d & 2d \end{bmatrix}. \quad (3.17)$$

If we also introduce an auxiliary vector in the form

$$\boldsymbol{\Omega}_{s,f} = \begin{bmatrix} \Omega_{s,f,1} \\ \Omega_{s,f,2} \\ \Omega_{s,f,3} \\ \Omega_{s,f,4} \end{bmatrix} = \begin{bmatrix} \Omega_1^2 \\ \Omega_2^2 \\ \Omega_5^2 \\ \Omega_6^2 \end{bmatrix}, \quad (3.18)$$

it is then possible to solve the control allocation problem as:

$$\boldsymbol{\Omega}_{s,f} = \mathbf{A}_f^{-1} \mathbf{u}^{\text{des}},$$

and by introducing the selection operator

$$\mathbf{E} = \begin{bmatrix} 1 & 0 & 1 & 0 & 0 & 0 & 0 & 0 \\ 0 & 1 & 0 & 1 & 0 & 0 & 0 & 0 \\ 0 & 0 & 0 & 0 & 1 & 0 & 1 & 0 \\ 0 & 0 & 0 & 0 & 0 & 1 & 0 & 1 \end{bmatrix}^T, \quad (3.19)$$

it is also possible to reconstruct the squared rotor velocity vector as:

$$\boldsymbol{\Omega}_s = \mathbf{E} \boldsymbol{\Omega}_{s,f}. \quad (3.20)$$

In order to include the angular velocity saturations as well, one can define the function

$$f_s(\Omega_{s,f}) = \begin{cases} 0, & \Omega_{s,f} < 0 \\ \Omega_{s,f}, & 0 \leq \Omega_{s,f} \leq \Omega_{\max}^2 \\ \Omega_{\max}^2, & \Omega_{s,f} > \Omega_{\max}^2 \end{cases} \quad (3.21)$$

with its full vector form

$$\mathbf{f}_s(\boldsymbol{\Omega}_{s,f}) = [f_s(\Omega_{s,f,1}) \quad f_s(\Omega_{s,f,2}) \quad f_s(\Omega_{s,f,3}) \quad f_s(\Omega_{s,f,4})]^T, \quad (3.22)$$

which is used in control allocation as shown in Fig. 3.6 . If we further define the full vector of squares of the angular velocities of each single motor

$$\mathbf{f}_m(\boldsymbol{\Omega}) = [\Omega_1^2 \quad \Omega_2^2 \quad \Omega_3^2 \quad \Omega_4^2 \quad \Omega_5^2 \quad \Omega_6^2 \quad \Omega_7^2 \quad \Omega_8^2]^T = \boldsymbol{\Omega}_s, \quad (3.23)$$

than the whole actuation can be shown in a compact form as in Fig. 3.6.

3.4 Linearized model

The controlled variables are represented with the vehicle position x, y, z and its attitude $\boldsymbol{\Psi}$, while the overall architecture includes xy , altitude, attitude and motor controllers as well as the control allocation and system dynamics consisted of the motor, actuation and the octocopter dynamics (see Fig. 3.7).

The desired linear motion reference values along a mission trajectory are applied to the xy controller, while the corresponding desired attitude and altitude reference values are handled by the related controllers. The outputs of these controllers form the desired values of the total force and torques to the control allocation algorithm to deal with the over-actuated system. This algorithm then distributes these desired values onto the desired velocity vector $\boldsymbol{\Omega}_{ref}$ to provide speeds for each motor. For the purpose of this work, we use a pseudo-inverse control allocation [67],[1]. The motor controller is used as a

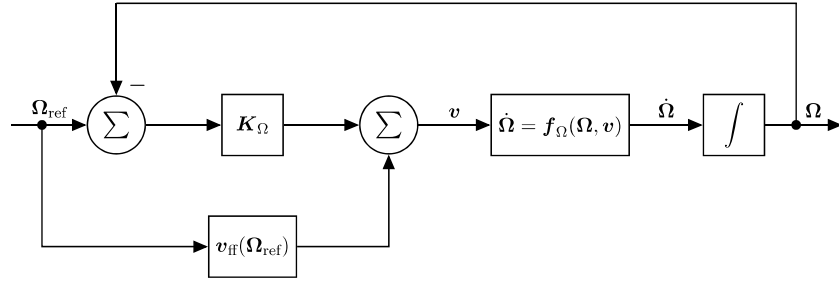


FIGURE 3.5
Vectorized control of motor speed.

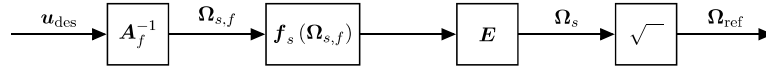


FIGURE 3.6
Actuation generation diagram.

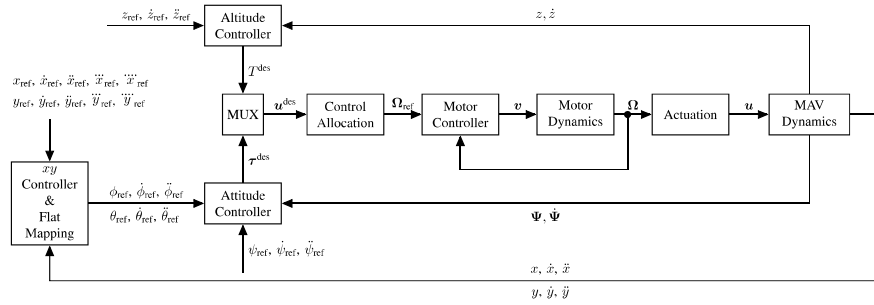


FIGURE 3.7
Control architecture.

low-level controller to force the motor velocity vector $\mathbf{\Omega}$ to follow the reference values from $\mathbf{\Omega}_{ref}$.

To design a PD tracking controller, it is common practice to linearize the octocopter dynamics around the hover configuration

$$\begin{aligned}(x_e, y_e, z_e) &= (x, y, z), \\ (u_e, v_e, w_e) &= (0, 0, 0), \\ (P_e, Q_e, R_e) &= (0, 0, 0), \\ (\phi_e, \theta_e, \psi_e) &= (0, 0, \psi).\end{aligned}\tag{3.24}$$

The linearized kinematic model of the linear motion can be described with:

$$\begin{aligned}\dot{x} &= c_{\psi_e} u - s_{\psi_e} v \\ \dot{y} &= s_{\psi_e} u + c_{\psi_e} v \\ \dot{z} &= w,\end{aligned}\tag{3.25}$$

while the linearized kinematic model of angular motion is represented by:

$$\begin{aligned}\dot{\phi} &= P \\ \dot{\theta} &= Q \\ \dot{\psi} &= R.\end{aligned}\tag{3.26}$$

Similarly, the linearized dynamic model of linear motion become

$$\begin{aligned}\dot{u} &= g\theta \\ \dot{v} &= -g\phi \\ \dot{w} &= \frac{T}{m_o} - g,\end{aligned}\tag{3.27}$$

while the linearized dynamic model of angular motion is simplified to

$$\begin{aligned}\dot{P} &= \frac{\tau_x}{I_{xx}} \\ \dot{Q} &= \frac{\tau_y}{I_{yy}} \\ \dot{R} &= \frac{\tau_z}{I_{zz}}.\end{aligned}\tag{3.28}$$

The compact form of these models can be written as

$$\dot{\mathbf{x}} = \mathbf{R}(Z, \psi_e) \mathbf{v}\tag{3.29}$$

$$\dot{\mathbf{\Psi}} = \mathbf{P}\tag{3.30}$$

$$\dot{\mathbf{v}} = \begin{bmatrix} 0 \\ 0 \\ \frac{T}{m_o} \end{bmatrix} + g \begin{bmatrix} \theta \\ -\phi \\ -1 \end{bmatrix}\tag{3.31}$$

$$\dot{\mathbf{P}} = \mathbf{J}^{-1} \boldsymbol{\tau},\tag{3.32}$$

where $\mathbf{R}(Z, \psi_e)$ represents the rotation matrix around the z -axis.

3.5 Altitude control near equilibrium

In order to design the tracking controller for maintaining the desired height of the octocopter, we start from the linearized dynamic model of linear motion in the form

$$\ddot{z} = \frac{T}{m_o} - g, \quad (3.33)$$

and form the control error as

$$e_z = z_{\text{ref}} - z, \quad (3.34)$$

where z_{ref} is a reference height. The PD control law can now be constructed in the form

$$T^{\text{des}} = m_o (g + \ddot{z}_{\text{ref}} + K_{dz}\dot{e}_z + K_{pz}e_z), \quad (3.35)$$

where g is the gravitational acceleration, while K_{pz} and K_{dz} proportional and derivative gains. Inserting (3.35) into (3.33), one can obtain the error dynamics as

$$\ddot{e}_z + K_{dz}\dot{e}_z + K_{pz}e_z = 0. \quad (3.36)$$

Since (3.36) is the second-order linear differential equation, the error e_z exponentially vanishes for positive values of K_{pz} and K_{dz} .

Fig. 3.8 demonstrates the block structure of the selected height tracking controller, while Fig. 3.9 shows the simulation results obtained for $K_{dz} = 5$ i $K_{pz} = 6.25$. One can notice from Fig. 3.9 that the octocopter satisfactory tracks the sinusoidal shape of the reference values.

3.6 Orientation control near equilibrium

In order to design the tracking controller for maintaining the desired orientation of the octocopter, we start from the linearized dynamic model of angular motion in the form

$$\ddot{\Psi} = \mathbf{J}^{-1}\boldsymbol{\tau}, \quad (3.37)$$

where \mathbf{J} is the inertia tensor of the octocopter given as

$$\mathbf{J} = \begin{bmatrix} I_{xx} & 0 & 0 \\ 0 & I_{yy} & 0 \\ 0 & 0 & I_{zz} \end{bmatrix}, \quad (3.38)$$

and $\dot{\Psi} = \mathbf{P}$, where $\Psi = [\phi \ \theta \ \psi]^T$ represent the angles with respect to the axes X , Y and Z , and $\mathbf{P} = [P \ Q \ R]^T$ being the vector of angular velocities in the local coordinate system.

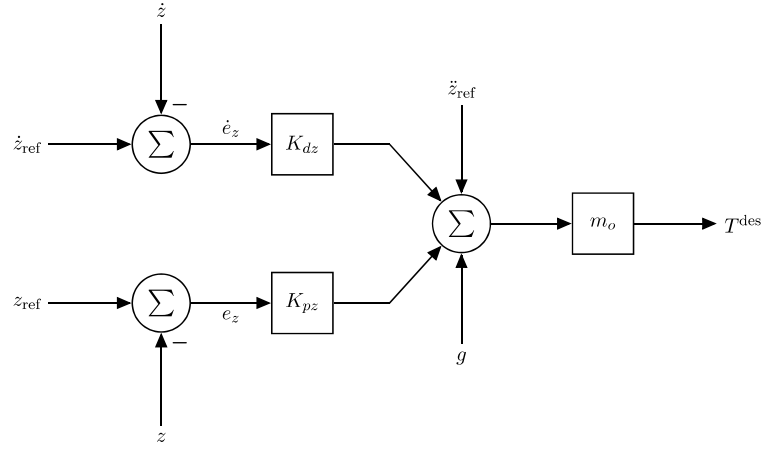


FIGURE 3.8
Altitude tracking control diagram.

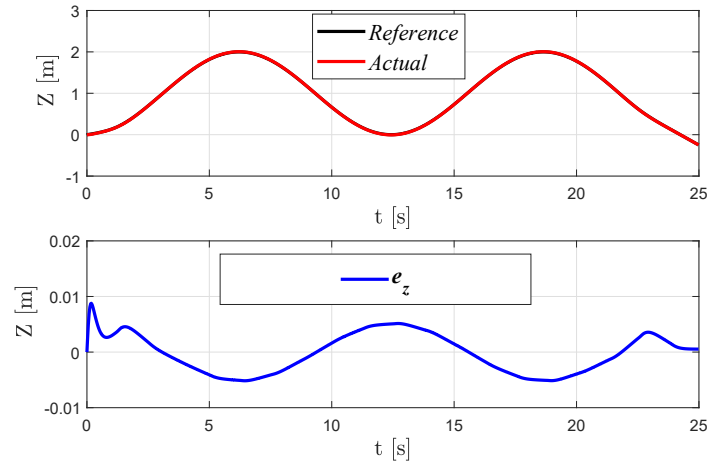
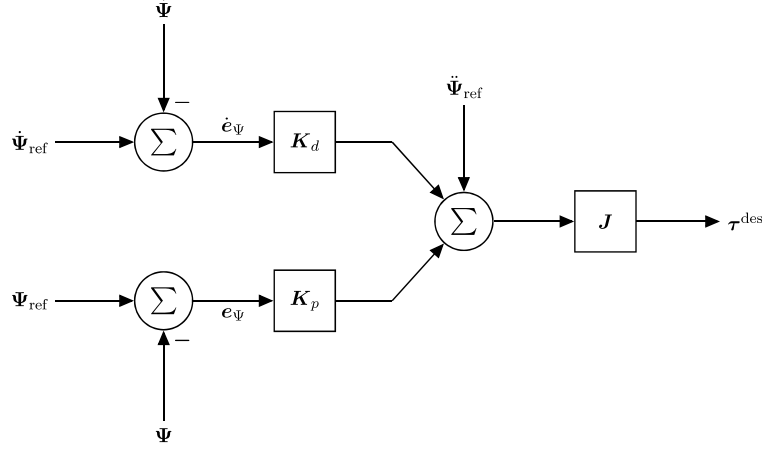


FIGURE 3.9
Altitude tracking results.

**FIGURE 3.10**

Orientation tracking control diagram.

The vector of control errors can be formed as

$$\mathbf{e}_{\Psi} = \begin{bmatrix} \phi_{\text{ref}} \\ \theta_{\text{ref}} \\ \psi_{\text{ref}} \end{bmatrix} - \begin{bmatrix} \phi \\ \theta \\ \psi \end{bmatrix} = \mathbf{\Psi}_{\text{ref}} - \mathbf{\Psi}, \quad (3.39)$$

and the PD control law can be constructed in the form

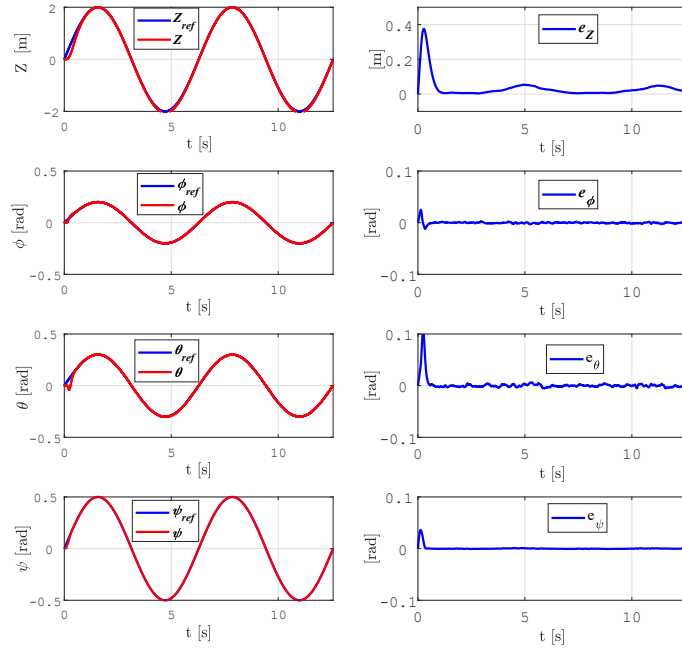
$$\boldsymbol{\tau}^{\text{des}} = \mathbf{J} \left(\ddot{\mathbf{\Psi}}_{\text{ref}} + \mathbf{K}_d \dot{\mathbf{e}}_{\Psi} + \mathbf{K}_p \mathbf{e}_{\Psi} \right), \quad (3.40)$$

yielding the error dynamics given in the vector form

$$\ddot{\mathbf{e}}_{\Psi} + \mathbf{K}_d \dot{\mathbf{e}}_{\Psi} + \mathbf{K}_p \mathbf{e}_{\Psi} = \mathbf{0}_{3 \times 1}. \quad (3.41)$$

Since (3.41) can be separated into three second-order differential equations, all three errors exponentially vanish for positive values of proportional and derivative gains K_d and K_p , where $\mathbf{K}_d = K_d \mathbf{I}_{3 \times 3}$ and $\mathbf{K}_p = K_p \mathbf{I}_{3 \times 3}$.

Fig. 3.10 demonstrates the block structure of the selected orientation tracking controller, while Fig. 3.11 shows the simulation results obtained of the simultaneous tracking of the height and orientations for $K_{dz} = 30$, $K_{pz} = 225$, $K_d = 20$ and $K_p = 100$. It can be seen from Fig. 3.11 that all tracking errors vanish within one second interval and that the tracking performance can be considered satisfactory despite the fact that the tracking is conducted simultaneously with respect to all control variables.

**FIGURE 3.11**

Altitude and orientation tracking results.

3.7 Position control near equilibrium

In order to design the tracking controller for maintaining the desired octo-copter position (x, y) in the global reference frame, we start from the linearized motion dynamics in the form

$$\begin{bmatrix} \ddot{x} \\ \ddot{y} \end{bmatrix} = g \begin{bmatrix} c_{\psi_e} & -s_{\psi_e} \\ s_{\psi_e} & c_{\psi_e} \end{bmatrix} \begin{bmatrix} \theta \\ -\phi \end{bmatrix}, \quad (3.42)$$

that is

$$\begin{bmatrix} \phi \\ \theta \end{bmatrix} = \frac{1}{g} \begin{bmatrix} s_{\psi_e} & -c_{\psi_e} \\ c_{\psi_e} & s_{\psi_e} \end{bmatrix} \begin{bmatrix} \ddot{x} \\ \ddot{y} \end{bmatrix}. \quad (3.43)$$

Therefore, in order to achieve tracking of the x and y position coordinates, we need a flat mapping between those positions and the altitude and attitude coordinates. For that reason, let the tracking errors $e_x = x_{\text{ref}} - x$ and $e_y = y_{\text{ref}} - y$ be introduced, where x_{ref} and y_{ref} are the reference values. If one wants the tracking errors to decay exponentially, it is sufficient that the following holds

$$\begin{bmatrix} \ddot{e}_x \\ \ddot{e}_y \end{bmatrix} + K_d \begin{bmatrix} \dot{e}_x \\ \dot{e}_y \end{bmatrix} + K_p \begin{bmatrix} e_x \\ e_y \end{bmatrix} = \mathbf{0}_{2 \times 1}, \quad (3.44)$$

which can be rewritten as (3.45)

$$\begin{bmatrix} \ddot{x} \\ \ddot{y} \end{bmatrix} = \begin{bmatrix} \ddot{x}_{\text{ref}} \\ \ddot{y}_{\text{ref}} \end{bmatrix} + K_d \begin{bmatrix} \dot{e}_x \\ \dot{e}_y \end{bmatrix} + K_p \begin{bmatrix} e_x \\ e_y \end{bmatrix}. \quad (3.45)$$

From (3.42) and assuming that $\Psi_e = \Psi_{\text{ref}} = \text{const}$, the reference values of the roll ϕ_{ref} and pitch θ_{ref} become

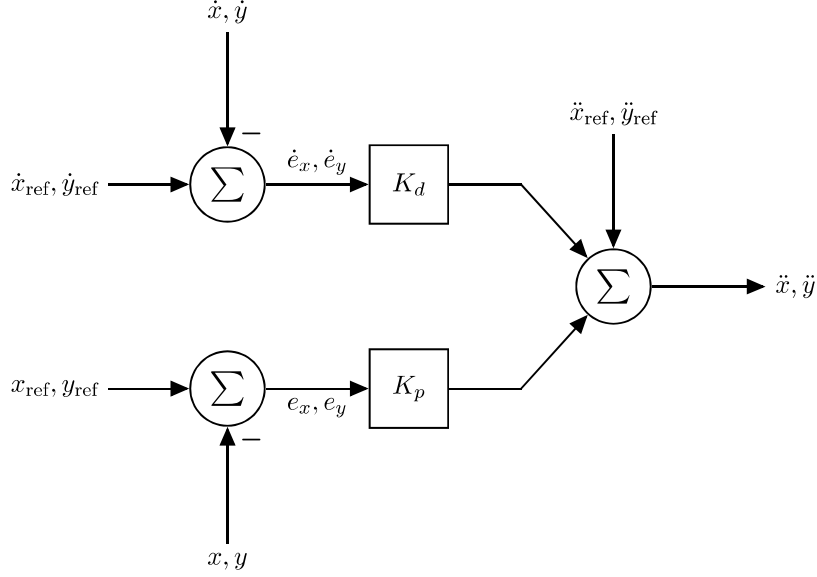
$$\begin{bmatrix} \phi_{\text{ref}} \\ \theta_{\text{ref}} \end{bmatrix} = \frac{1}{g} \begin{bmatrix} s\psi_{\text{ref}} & -c\psi_{\text{ref}} \\ c\psi_{\text{ref}} & s\psi_{\text{ref}} \end{bmatrix} \begin{bmatrix} \ddot{x} \\ \ddot{y} \end{bmatrix}. \quad (3.46)$$

The attitude controller (3.40) requires the first and the second derivation of the roll and pitch reference values. By differentiating (3.46), we get

$$\begin{aligned} \begin{bmatrix} \dot{\phi}_{\text{ref}} \\ \dot{\theta}_{\text{ref}} \end{bmatrix} &= \frac{1}{g} \begin{bmatrix} s\psi_{\text{ref}} & -c\psi_{\text{ref}} \\ c\psi_{\text{ref}} & s\psi_{\text{ref}} \end{bmatrix} \begin{bmatrix} \ddot{x} \\ \ddot{y} \end{bmatrix}, \\ \begin{bmatrix} \ddot{\phi}_{\text{ref}} \\ \ddot{\theta}_{\text{ref}} \end{bmatrix} &= \frac{1}{g} \begin{bmatrix} s\psi_{\text{ref}} & -c\psi_{\text{ref}} \\ c\psi_{\text{ref}} & s\psi_{\text{ref}} \end{bmatrix} \begin{bmatrix} \ddot{\ddot{x}} \\ \ddot{\ddot{y}} \end{bmatrix}. \end{aligned} \quad (3.47)$$

If \ddot{x} , \ddot{y} , $\ddot{\ddot{x}}$, $\ddot{\ddot{y}}$ are known, then one can obtain $\dot{\phi}_{\text{ref}}$, $\dot{\theta}_{\text{ref}}$, $\ddot{\phi}_{\text{ref}}$ and $\ddot{\theta}_{\text{ref}}$ from (3.47). By conducting additional differentiation of (3.45), we get $(\ddot{\ddot{x}}, \ddot{\ddot{y}})$ and $(\ddot{\ddot{x}}, \ddot{\ddot{y}})$ as follows

$$\begin{aligned} \begin{bmatrix} \ddot{\ddot{x}} \\ \ddot{\ddot{y}} \end{bmatrix} &= \begin{bmatrix} \ddot{\ddot{x}}_{\text{ref}} \\ \ddot{\ddot{y}}_{\text{ref}} \end{bmatrix} + K_d \begin{bmatrix} \ddot{e}_x \\ \ddot{e}_y \end{bmatrix} + K_p \begin{bmatrix} \dot{e}_x \\ \dot{e}_y \end{bmatrix}, \\ \begin{bmatrix} \ddot{\ddot{\ddot{x}}} \\ \ddot{\ddot{\ddot{y}}} \end{bmatrix} &= \begin{bmatrix} \ddot{\ddot{\ddot{x}}}_{\text{ref}} \\ \ddot{\ddot{\ddot{y}}}_{\text{ref}} \end{bmatrix} + K_d \begin{bmatrix} \ddot{\ddot{e}}_x \\ \ddot{\ddot{e}}_y \end{bmatrix} + K_p \begin{bmatrix} \ddot{e}_x \\ \ddot{e}_y \end{bmatrix}. \end{aligned} \quad (3.48)$$

**FIGURE 3.12**

Control diagram for tracking x and y Cartesian coordinates.

Eqs. (3.45) to (3.48) represent the xy position controller and the flat mapping between (x, y) and (ϕ, θ) . The proposed controller is able to track the reference x_{ref} , y_{ref} , and z_{ref} as well as ψ_{ref} . The proposed architecture has been exploited in [34] to control the position and orientation of the octocopter.

It is necessary to emphasize that the reference trajectories of the x and y position coordinates must be at least four times differentiable, while trajectories for the altitude z and orientation ψ must have the first and the second derivation. These trajectories are provided by an adequate motion planning algorithm, while references for ϕ and θ orientation coordinates are provided as the output of the xy controller.

Fig. 3.12 shows the block structure of the position tracking controller, while Fig. 3.13 illustrates how to transform x i y positions based on the flat mapping ((3.45) to (3.48)). Figs. 3.12 and 3.13, together with the altitude controller shown in Fig. (3.8) construct the position controller of the octocopter.

Fig. 3.14 shows the results obtained for position and orientation tracking for $K_{dz} = 14.5$, $K_{pz} = 52.56$, $K_d = 45$ and $K_p = 506.5$. Although the reference trajectories are quite demanding, it can be seen that the tracking errors vanish within a 4-second interval and the overall tracking performance can be considered satisfactory.

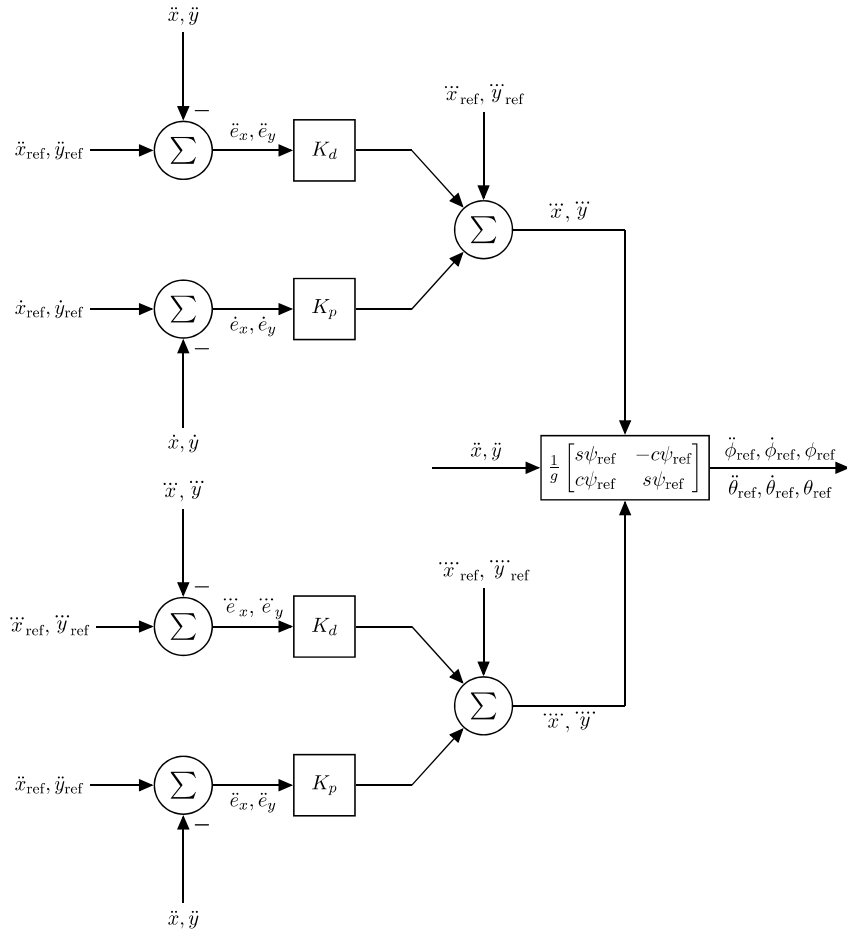


FIGURE 3.13
Flatness-based control diagram.

3.8 Overall UAV control architecture

The final control architecture for trajectory tracking which includes x , y , z coordinates, as well as orientation ψ , is shown in Fig. 3.7. The architecture contains the xy positional controller which includes flat mapping, altitude controller and attitude tracking controllers, control allocation and low-level control of motor angular velocity for each single motor.

As previously indicated, the reference trajectories for x and y coordinates should be at least four times differentiable, while the reference trajectories for the altitude z and the orientation ψ should be at least two times differentiable. In addition, one can notice that the change of ϕ and θ angles will be the result of the xy position controller.

To illustrate the proposed control architecture for the position and orientation tracking, we consider the Vivian curve (ococopter with PPNPPNN configuration) in the three-dimensional space, which is represented in Fig. 3.15. The tracking errors with respect to the coordinates x , y , z and the orientation ψ are give in Fig. 3.16 from which one can observe a small tracking errors with respect to the chosen reference trajectory.

3.9 RLS-based fault tolerant control

As a motivational example for the next subsection, we present here the tracking performance in case one motor (e.g., M_3) is in fault state from the start of the flying mission. As it can be seen from Fig. 3.17, there exist a permanent tracking error, where, for instance, the tracking error for x coordinate becomes 0.5 meters at some time instants. From this simple example, one can conclude that a single motor failure may cause a permanent error with respect to some coordinates. Depending on which motor is in a fault state, the tracking error may vary along different coordinates. It is also worth noting that the octocopter is a system with a redundant structure (there exist the remaining active 7 motors) and the controller used in this example does not exploit any information about the motor failure. For this reason, the control allocation generates the control inputs to that motor as well, producing undesired system behaviour.

In order to fully exploit the redundant structure of an octocopter system, it is worth designing a controller that will take into account the information about motor failure and allocate the control inputs only to those active motors in order to achieve a satisfactory tracking performance.

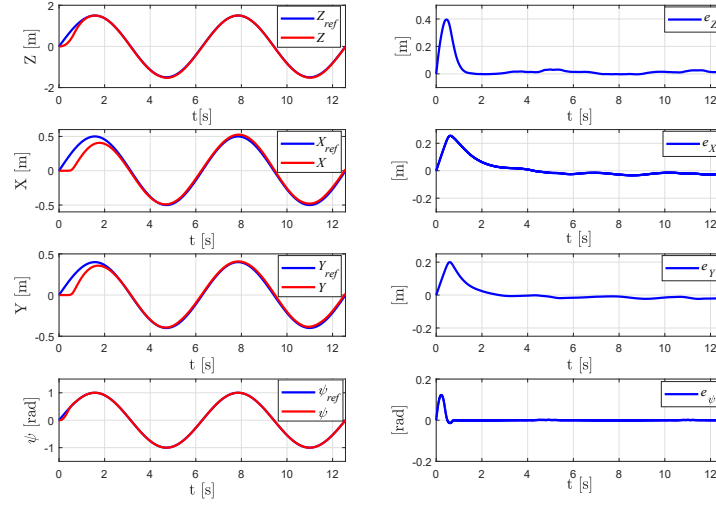


FIGURE 3.14
Position and orientation tracking results.

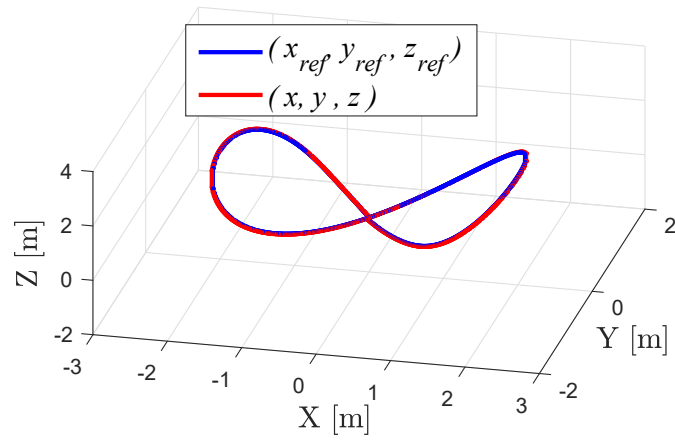
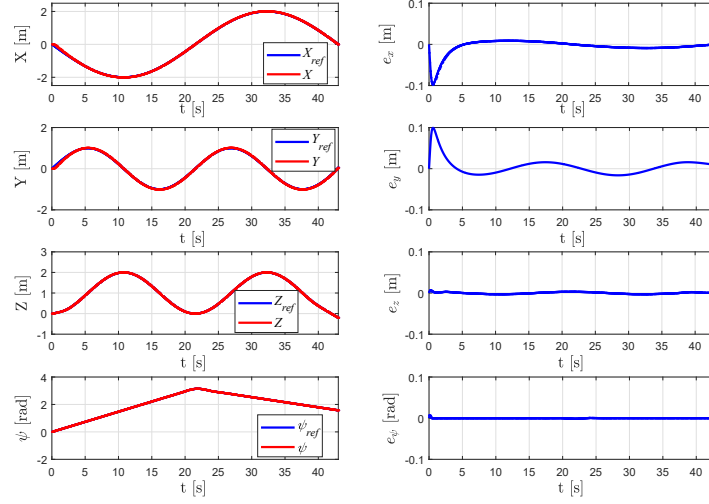
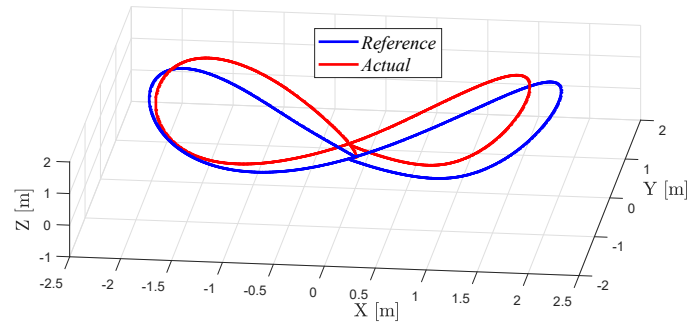


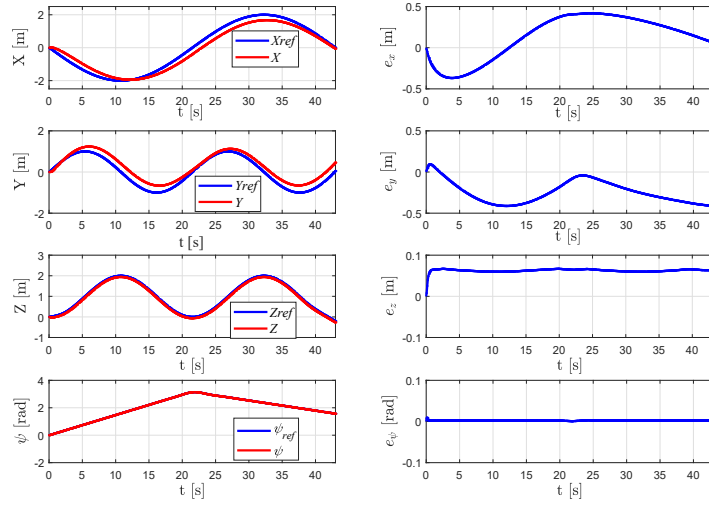
FIGURE 3.15
Trajectory tracking of Viviani curve achieved with an PNPNPNN octocopter configuration structure without any failure states.

**FIGURE 3.16**

Trajectory tracking for each position and orientation achieved with an PNPNPNP octocopter configuration structure without any failure states. Left: reference and achieved values. Right: tracking errors.

**FIGURE 3.17**

Trajectory tracking achieved with an PNPNPNP octocopter configuration structure with the motor M_3 being in a fault state.

**FIGURE 3.18**

Trajectory tracking achieved with an PNPNPNP octocopter configuration structure and M_3 being in a fault state. Left: reference and achieved values, Right: tracking errors.

3.9.1 Fault-tolerant PD tracking control

To design a fault-tolerant control, it is necessary to include information about fault states of DC motors into the actuation matrix. Accordingly, we can rewrite the actuation matrix as:

$$\mathbf{u} = \mathbf{A} \text{diag}(\boldsymbol{\Omega}_s) \boldsymbol{\theta}, \quad (3.49)$$

where $\boldsymbol{\theta} = [\theta_1 \ \theta_2 \ \theta_3 \ \theta_4 \ \theta_5 \ \theta_6 \ \theta_7 \ \theta_8]^T$ represents the fault state vector of DC motors. The coefficients $0 \leq \theta_i \leq 1$ ($i = \overline{1..8}$) represent the failure level of related DC motor, where $\theta_i = 1$ represents a fully available M_i motor, $\theta_i = 0$ a failed M_i motor, while all other values in between represent a partial loss of the related DC motor functionality that is their working capacity level. If we rewrite the actuation matrix as $\mathbf{A} = [\mathbf{A}_T \ \mathbf{A}_1 \ \mathbf{A}_2 \ \mathbf{A}_3]^T$, the components of the $\boldsymbol{\tau}_x$, $\boldsymbol{\tau}_y$ and $\boldsymbol{\tau}_z$ vectors of the controllable control signals \mathbf{u} can be represented as weighted scalar products in the form

$$\begin{aligned} T &= \mathbf{A}_T \text{diag}(\boldsymbol{\Omega}_s) \boldsymbol{\theta} \\ \tau_x &= \mathbf{A}_1 \text{diag}(\boldsymbol{\Omega}_s) \boldsymbol{\theta} \\ \tau_y &= \mathbf{A}_2 \text{diag}(\boldsymbol{\Omega}_s) \boldsymbol{\theta} \\ \tau_z &= \mathbf{A}_3 \text{diag}(\boldsymbol{\Omega}_s) \boldsymbol{\theta}. \end{aligned} \quad (3.50)$$

As we can see from (3.50), the control output can be represented by its four linearly dependant components. Based on these values, it is possible to estimate the parameter vector $\boldsymbol{\theta}$ in a least-squares manner. For the estimation, it is necessary to know all other parameters in (3.50). The basic requirement is that the values of the actuation matrix \mathbf{A} are a priori known. We only use gyroscopic data to detect and isolate failures, so that the first equality from (3.50) can be omitted, so the final model which will be used for prediction is

$$\begin{aligned} \tau_x &= \mathbf{A}_1 \text{diag}(\boldsymbol{\Omega}_s) \boldsymbol{\theta} \\ \tau_y &= \mathbf{A}_2 \text{diag}(\boldsymbol{\Omega}_s) \boldsymbol{\theta} \\ \tau_z &= \mathbf{A}_3 \text{diag}(\boldsymbol{\Omega}_s) \boldsymbol{\theta}. \end{aligned} \quad (3.51)$$

If we have N measurements at time instances 1 to N , then for each sample $i = \overline{1..N}$, based on (3.51), we have the following model to predict the output

$$\begin{aligned} \hat{\tau}_x(i) &= \boldsymbol{\Psi}_1^r(i) \boldsymbol{\theta}, \\ \hat{\tau}_y(i) &= \boldsymbol{\Psi}_2^r(i) \boldsymbol{\theta}, \\ \hat{\tau}_z(i) &= \boldsymbol{\Psi}_3^r(i) \boldsymbol{\theta}, \end{aligned} \quad (3.52)$$

where each regressor of output models is defined as

$$\begin{aligned} \boldsymbol{\Psi}_1^r(i) &= \mathbf{A}_1 \text{diag}(\boldsymbol{\Omega}_s(i)), \\ \boldsymbol{\Psi}_2^r(i) &= \mathbf{A}_2 \text{diag}(\boldsymbol{\Omega}_s(i)), \\ \boldsymbol{\Psi}_3^r(i) &= \mathbf{A}_3 \text{diag}(\boldsymbol{\Omega}_s(i)). \end{aligned} \quad (3.53)$$

Using the property that each tensor can be represented as a matrix using the skew-symmetric matrix \mathbf{S} defined in (2.26), we can represent the inertia tensor $\mathbf{J} = \text{diag}([I_{xx} \ I_{yy} \ I_{zz}])$ as a symmetric matrix. Now, we can rewrite (2.31) as

$$\begin{aligned}\tau_x(i) &= I_{xx}\dot{P}(i) - (I_{yy} - I_{zz})Q(i)R(i), \\ \tau_y(i) &= I_{yy}\dot{Q}(i) - (I_{zz} - I_{xx})P(i)R(i), \\ \tau_z(i) &= I_{zz}\dot{R}(i) - (I_{xx} - I_{yy})P(i)Q(i).\end{aligned}\quad (3.54)$$

We can now formulate the FDI technique for the propulsion system as a recursive least square (RLS) estimation problem of the rotor capacity vector $\boldsymbol{\theta}$ in the following way:

$$\boldsymbol{\tau} = [\tau_x(1) \ \tau_y(1) \ \tau_z(1) \ \dots \ \tau_x(N) \ \tau_y(N) \ \tau_z(N)]^T, \quad (3.55)$$

where the data matrix $\boldsymbol{\Psi}^r$ has the form

$$\boldsymbol{\Psi}^r = [\boldsymbol{\Psi}_1^{rT}(1) \ \boldsymbol{\Psi}_2^{rT}(1) \ \boldsymbol{\Psi}_3^{rT}(1) \ \dots \ \boldsymbol{\Psi}_1^{rT}(N) \ \boldsymbol{\Psi}_2^{rT}(N) \ \boldsymbol{\Psi}_3^{rT}(N)]^T. \quad (3.56)$$

By using a classical non-recursive least-square method [28], we can express the coefficient $\hat{\boldsymbol{\theta}}$ as

$$\hat{\boldsymbol{\theta}} = \left(\boldsymbol{\Psi}^{rT} \boldsymbol{\Psi}^r \right)^{-1} \boldsymbol{\Psi}^{rT} \boldsymbol{\tau}. \quad (3.57)$$

It is necessary to emphasize that this RLS technique has a linear configuration, while obtaining values for the vector rotor capacity comes from the nonlinear octocopter model (2.31). The proposed method can be applied to any type of MAV with $2n$ rotors mounted in a planar plane.

To apply the aforementioned RLS technique to an octocopter system, the RLS with a forgetting factor is used. The values for θ_i obtained by the RLS algorithm are used as a feedback to update the actuation matrix. Note that $\boldsymbol{\theta}$ and $\boldsymbol{\Omega}_s$ represent vectors of the same size, so (3.49) can be rewritten as

$$\mathbf{u} = \mathbf{A} \text{diag}(\boldsymbol{\theta}) \boldsymbol{\Omega}_s. \quad (3.58)$$

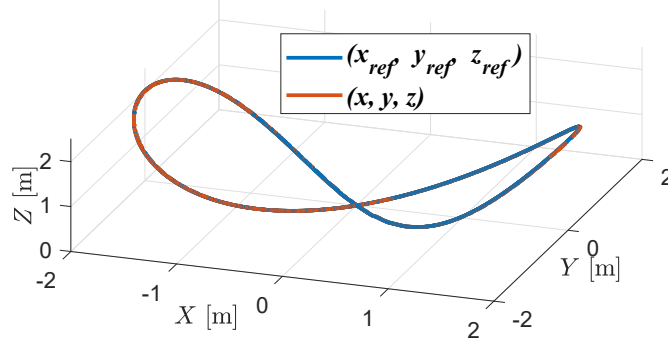
Furthermore, by introducing a new matrix \mathbf{B} as $\mathbf{B} = \mathbf{A} \text{diag}(\boldsymbol{\theta})$, we can calculate the velocity for all DC motors that can achieve the reference thrust and torques as

$$\boldsymbol{\Omega}_s = \mathbf{B}^+ \mathbf{u}, \quad (3.59)$$

where $\mathbf{B}^+ = \mathbf{B}^T (\mathbf{B} \mathbf{B}^T)^{-1}$.

3.9.2 Simulation results for Fault-tolerant PD tracking control

In this subsection, we present the simulation results for the RLS-based technique for detection and isolation of DC motor failures on an octocopter system.

**FIGURE 3.19**

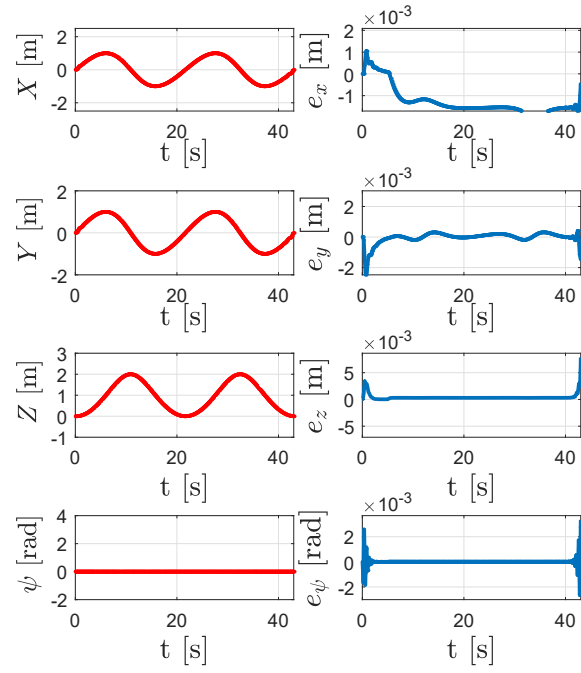
Tracking performance achieved in 3D space with an PNPNPNP octocopter configuration structure based on a PD controller and control allocation algorithm with a fault state in motor M_3 starting from $t = 5$ [s].

We used a fault-tolerant PD tracking control system around the hovering configuration. To illustrate that the designed controller is capable of handling a fault state on an octocopter system, we consider the PPNPNN configuration.

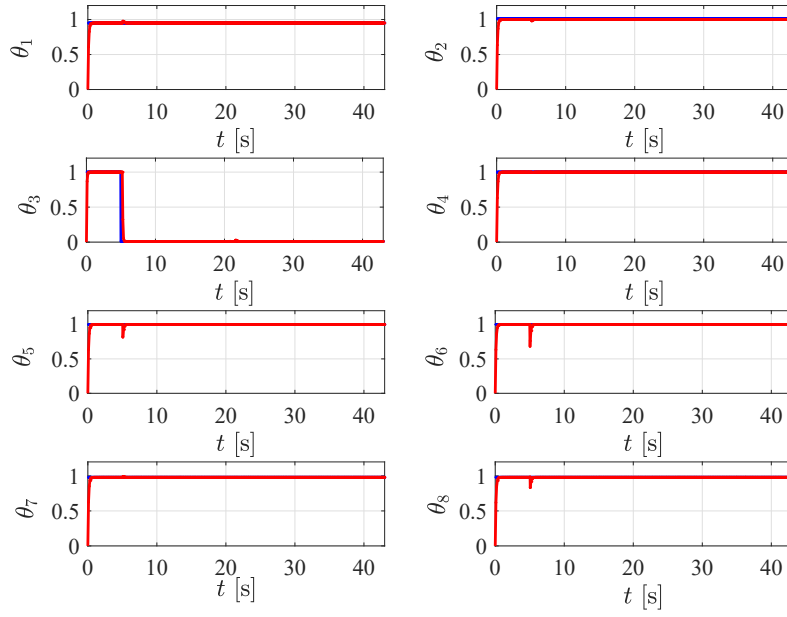
It should be emphasized that the presented approach was tested for different types of possible faults (different numbers of failed motors and different values of rotor capacity). For the purpose of the RLS algorithm (3.55), we need to determine eight unknowns parameters θ_i , so we need at least eight equations. It follows that the number of samples N must be $N \geq 8$. However, to eliminate the impact of noise, it is advisable to use a larger number of equations, that is $N \gg 8$. So, we set the forgetting factor to 0.8 in order to take into account the measurements from the previous 0.8 seconds to provide a sufficient number of samples for the RLS algorithm. Let now a failure related to the motor M_3 occurs at time $t = 5$ [s], which can be expressed by the rotor capacity vector $\theta = [1 \ 1 \ 0 \ 1 \ 1 \ 1 \ 1 \ 1]^T$. Figs. 3.19 and 3.20 depict the performance of the RLS-based PD tracking controller merged with the control allocation for the given failure. Fig. 3.21 also shows that the relative capacity of each motor is properly estimated.

[scale=0.4]

From Fig. 3.20, we can conclude that the presented RLS controller has an acceptable tracking performance which is similar to the tracking performance of a healthy octocopter system (an octocopter system without any faulty states). Such a result is expected and it can be attributed to fault-tolerability that an octocopter system inherently possesses by design.

**FIGURE 3.20**

Tracking performance achieved with an PNPNPNP octocopter configuration based on a PD control with a fault state in motor M_3 starting from $t = 5$ [s]. Left: reference values. Right: tracking error.

**FIGURE 3.21**

Estimation of rotor capacities during the tracking task.

4

Maneuverability

CONTENTS

4.1	Fault-dependent admissible set of thrust force and torques	51
4.2	Fault-dependent controllability test procedure	56
4.3	Fault-dependent controllability analysis for a quadcopter system	57
4.3.1	Fault-dependent controllability analysis for a hexacopter system	58
4.3.2	Fault-dependent controllability analysis for an octocopter system	58

In order to develop a motion planner and estimate a possibility of completing a pre-planned mission, it is necessary to determine whether the system is capable of generating necessary thrust and torques, to be able to reach the waypoints generated by the motion planner with available DC motors. Regardless of whether the system contains a redundant actuation or not, it is possible to have a case when a control algorithm is not able to track the referent trajectory (e.g, a fault state). This problem has been addressed in [67, 13, 12, 71, 79, 41] for a MAV designed with fixed and classical rotor configurations (quadcopter, hexacopter and octocopter). In addition, in [52] and [46], the controllability analysis has been considered for a MAV designed with a tilted rotor, while for non-classical (coaxial) octocopters the relevant analysis has been given in [66]. In this chapter, an empirical method is presented which can be used for any MAV configuration designed with different number of rotors and their rotational directions.

4.1 Fault-dependent admissible set of thrust force and torques

To find an admissible set of thrust force and torques in control space, it is necessary to check whether the system can reach and stay in a hovering state without any rotation. For illustration purposes, consider again an octocopter with the PNPNP configuration. The relation between the control inputs

u (the reference thrust force T and torques τ) and the rotation velocity Ω_s of DC motors is given with $\mathbf{u}_{ref} = \mathbf{A}\Omega_s$ (see Chapter 3), where the control vector \mathbf{u}_{ref} is represented by

$$\mathbf{u}_{ref} = [T \quad \tau]^T = [T \quad \tau_x \quad \tau_y \quad \tau_z]^T, \quad (4.1)$$

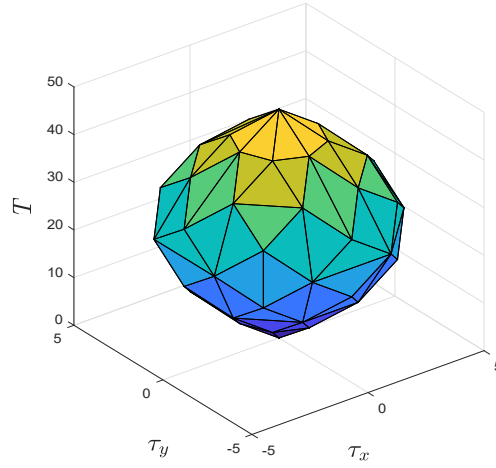
$\Omega_s \in D_{\Omega_s} \subset \mathbb{R}^8$ and $\mathbf{u} \in D_u \subset \mathbb{R}^4$. The set D_{Ω_s} is defined based on velocity constraints of DC motors

$$0 \leq \Omega_i^2 \leq \Omega_{\max}^2, \quad i = \overline{1..8}. \quad (4.2)$$

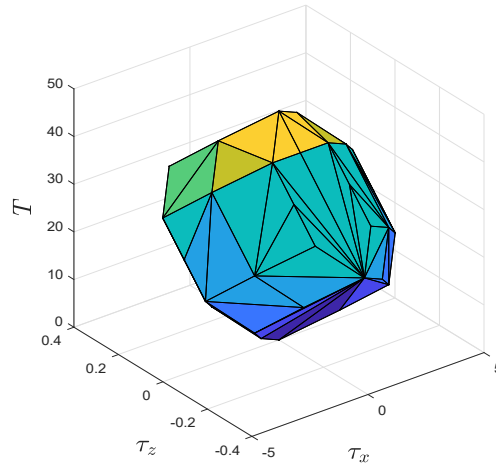
Assuming that the DC motor velocity is limited between 0 and ω_{max} (4.2) and the mapping is defined by the linear relation $\mathbf{u}_{ref} = \mathbf{A}\Omega_s$, it means that the set D_u represents a polytope in space \mathbb{R}^4 . If velocities of all DC motors are equal to zero when all components of the control input are zero-valued, we get the first point in control space determined with 4 coordinates (T , τ_x , τ_y and τ_z). If we now set the angular velocity of the first DC motor to its maximum value, we get the second point in control space. The total number of these combinations is 2^{2n} , where n is the number of pairs DC motors. For the octocopter example, it is possible to construct one hyper-plane for each tuple (4 control components) of 256 points in total. However, only those hyper-planes that form an outer region are relevant to define the admissible set. In this way, one can construct a convex polytope-like admissible region in four-dimensional space. These admissible sets can be used to impose additional constraints during the planning stage in order to generate only those referent trajectories which the octocopter will be capable of tracking. Since the obtained region is constructed in four-dimensional control space, we only illustrate three simplified cases for which $\tau_x = 0$, $\tau_y = 0$ and $\tau_z = 0$. An orthogonal projection of the polytope of the set D_u (with coordinates (T, τ_x, τ_y) , (T, τ_x, τ_z) i (T, τ_y, τ_z)) is shown in Figs. 4.1, 4.2 and 4.3, respectively.

In order to make an octocopter system stable at an arbitrarily hovering point, it is obvious that the thrust force should compensate the gravitational force, that is $T = mg$. If the represented three-dimensional set from Fig. 4.1 is projected onto the plane $T = mg$, then the projection is shown in Fig. 4.4. It can be observed that the torques τ_x and τ_y have symmetric values and that they are mutually constrained, meaning that is not possible to simultaneously reach maximal values of the torques τ_x and τ_y . Consider now the DC motor M_1 is in a fault state. The projection of the torques τ_x and τ_y onto the plane $T = mg$ is shown in Fig. 4.5. In case of a double fault (fault states of DC motors M_1 and M_2), the projection of the torques onto the plane $T = mg$ is shown in Fig. 4.6.

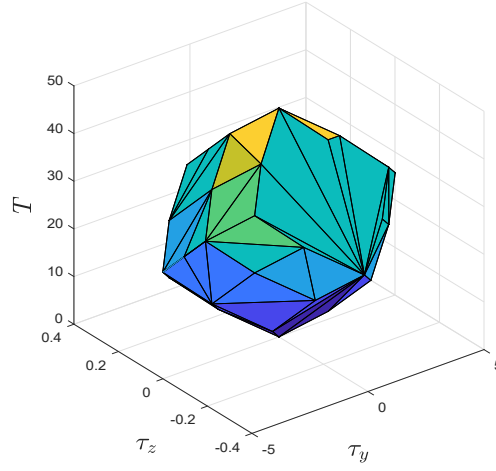
It can be seen from Fig. 4.5 and 4.6 that the admissible set for τ_x and τ_y is reduced with respect to a healthy octocopter system shown in Fig. 4.4. Depending on the type and combination of faults occurred, some of the planned maneuvers for stabilizing a hovering state will not be possible. The final control admissible set depends on the failure mode occurred and ultimately influence

**FIGURE 4.1**

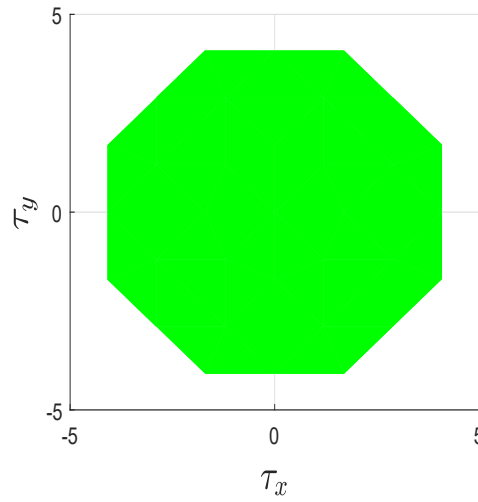
Representation of the four-dimensional admissible region $(T, \tau_x, \tau_y, \tau_z)$ in three-dimensional space (T, τ_x, τ_y) when $\tau_z = 0$.

**FIGURE 4.2**

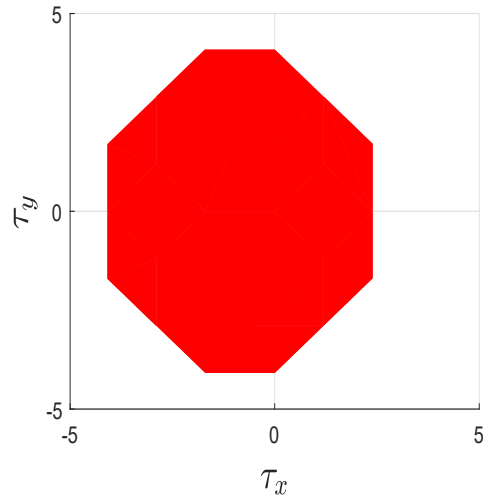
Representation of the four-dimensional admissible region $(T, \tau_x, \tau_y, \tau_z)$ in three-dimensional space (T, τ_x, τ_z) when $\tau_y = 0$.

**FIGURE 4.3**

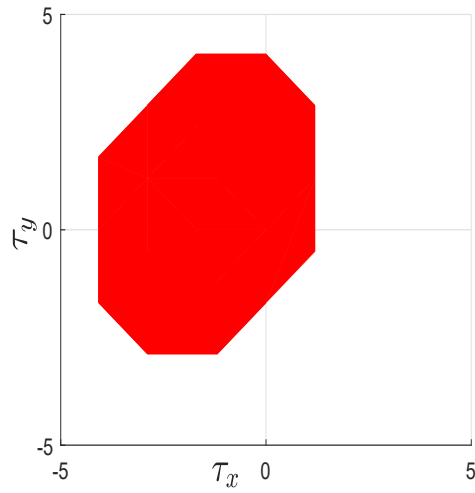
Representation of the four-dimensional admissible region $(T, \tau_x, \tau_y, \tau_z)$ in three-dimensional space (T, τ_y, τ_z) when $\tau_x = 0$.

**FIGURE 4.4**

The projection of torques τ_x, τ_y onto the plane $T = mg$ along its orthogonal direction for a PNPNPNP octocopter configuration structure without any fault states.

**FIGURE 4.5**

The projection of torques τ_x and τ_y onto the plane $T = mg$ along its orthogonal direction for a PNPNPNP octocopter configuration structure with a fault state related to the DC motor M_1 .

**FIGURE 4.6**

The projection of torques τ_x and τ_y onto the plane $T = mg$ along its orthogonal direction, for a PNPNPNP octocopter configuration structure with a double fault state related to the DC motors M_1 and M_2 .

the maneavarebility of the octocopter system. For different combinations of failure modes, the system will not be capable to achieve and stay at different hovering states. The obtained admissible sets have been illustrated only to understand that each DC motor has a different effect on the generation of thrust T and torques τ_x , τ_y and τ_z .

4.2 Fault-dependent controllability test procedure

To understand whether an octocopter system is controllable (or at least stabilizable) in case of a single fault (or any multiple-faults combination), we introduce a testing procedure to check whether a hovering state is reachable or not. We say that an octocopter system is controllable with respect to a certain state in case there is a control input that moves the octocopter to that state. In case the controller is not capable to influence yaw-torque τ_z only, we say the system is stabilizable in that state. The latter means that the vehicle is capable to remain at the given position only by rotating around z -axes.

The task of the control allocation algorithm is to distribute DC motor velocities Ω_s to each motor in order to achieve the referent thrust force and torques for reaching a waypoint generated by a motion planner. For all MAVs for which $n > 2$, there is an infinite number of realization to achieve the same result in case a feasible solution exists. To check whether a feasible solution exists, we define the optimization problem to generate the optimal solution Ω_s^* that minimizes the square-error between the reference $u_{ref} = \mathbf{A}\Omega_s$ and the achieved control over the feasible control region ($0 \leq \Omega_s \leq \omega_{max}^2$)

$$\Omega_s^* = \underset{0 \leq \Omega_s \leq \omega_{max}^2}{\operatorname{argmin}} (\|e_p\|^2) = \underset{0 \leq \Omega_s \leq \omega_{max}^2}{\operatorname{argmin}} (\|u_{ref} - \mathbf{A}\Omega_s\|^2), \quad (4.3)$$

where the hovering reference control is defined as $u_{ref} = [mg \ 0 \ 0 \ 0]^T$.

For the optimization problem (4.3), one can obtain three different cases.

1. In case there is no feasible solution, i.e. the octocopter is not capable of achieving the desired hovering state, the system is not controllable with respect to the control admissible set.
2. In case there is a feasible solution yielding zero-valued $e_p = [0 \ 0 \ 0 \ 0]^T$, then the hovering state is achievable and the octocopter is controllable with respect to the control admissible set.
3. In case there is a feasible solution for which there is at least one non-zero error component, we have two additional cases.
 - (a) If we allow free movements around z -axis, we exclude the torque θ_z , that is $u_{ref}^- = [T \ \tau_x \ \tau_y]^T = [mg \ 0 \ 0]^T$ and

repeat the optimization. In case we obtain zero-valued error $e_p^- = [0 \ 0 \ 0]^T$, then the octocopter is capable to achieve and stay at the hovering state, although it will be rotating around z -axis. In this case, we say the octocopter is stabilizable with respect to the control admissible set.

- (b) In case the error e_p^- has at least one non-zero component, the octocopter is not controllable with respect to the control admissible set. However, in this case the non-zero error indicates the closest state to the desired hovering state from which one can understand the resulted behaviour of the octocopter system. For instance, we can conclude whether the system will increase ($T > mg$) or decrease ($T < mg$) its height with respect to the desired hovering state or the octocopter system will rotate around an axis in one or the other direction.

By checking whether the hovering point is reachable or not, we can understand if the octocopter system is capable for given mission regardless of the faults. In the following subsection, we show how to thoroughly analyze controllability of different types of MAVs by examining different single and multiple faults including the octocopter system. For clarity, we include the related procedures for the quadcopter and hexacopter systems as well.

4.3 Fault-dependent controllability analysis for a quadcopter system

Consider a quadcopter without any fault states (a healthy quadcopter system). The quadcopter is designed based on the following parameters [35]: $m_o = 1.32 \text{ [kg]}$, $l = 0.211 \text{ [m]}$, $I_{xx} = I_{yy} = 0.0128 \text{ [kgm}^2\text{]}$, $I_{zz} = 0.0239 \text{ [kgm}^2\text{]}$, $I_{zzm} = 4.3 \cdot 10^{-5} \text{ [kgm}^2\text{]}$, $b = 9.9865 \cdot 10^{-6} \text{ [}\frac{\text{Ns}^2}{\text{rad}^2}\text{]}$, $d = 1.5978 \cdot 10^{-7} \text{ [}\frac{\text{Nms}^2}{\text{rad}^2}\text{]}$, $\omega_{max} = 840 \text{ [rad/s]}$.

Solving the optimization problem (4.3), in which the referent thrust force and torques are given as $\mathbf{u}_{ref} = [T \ \boldsymbol{\tau}]^T = [mg \ 0 \ 0 \ 0]^T$, we obtain $\omega_1 = \omega_2 = \omega_3 = \omega_4 = 569.35 \text{ [rad/s]}$ and $e_p = [0 \ 0 \ 0 \ 0]^T$. This means that the hovering point is reached and it is possible to stabilize the MAV at this point. Let now the same optimization problem be considered for the quadcopter case for each possible single fault with the same reference $\mathbf{u}_{ref} = [T \ \boldsymbol{\tau}]^T = [mg \ 0 \ 0 \ 0]^T$. The results of these optimizations are shown in Table 4.1. As it can be seen, the quadcopter cannot be fully controlled at the hovering point for every single failure. Such cases are indicated by red color in Table 4.1. For example, in case of a failure occurred in the DC motor M_1 , we obtain $e_p = [0 \ -0.03 \ 0 \ 0.21]^T$. For this case the quadcopter is

stabilizable, but there is a constant rotation in the negative direction about the x -axis as well as intense rotation about the z -axis.

The obtained results are expected since they are in line with the state-of-the-art work. In [79], the authors have shown that the quadcopter does not have a redundant configuration and its controllability will be lost in case any of the DC motors fails. These results indicate that a quadcopter structure designed with only four motors cannot be reliable system in cases when there is a high probability of any single motor failure.

4.3.1 Fault-dependent controllability analysis for a hexacopter system

In this subsection, we analyze two types of hexacopter design, including the PNPNP and the PPNNPN rotation configuration. The hexacopter is designed based on the following parameters: $m_o = 1.54$ [kg], $l = 0.211$ [m], $I_{xx} = I_{yy} = 0.0168$ [kgm²], $I_{zz} = 0.0308$ [kgm²], $I_{zzm} = 2 \cdot 10^{-5}$ [kgm²], $b = 8.5485 \cdot 10^{-6}$ [$\frac{Ns^2}{rad^2}$], $d = 1.3678 \cdot 10^{-7}$ [$\frac{Nms^2}{rad^2}$], $\omega_{max} = 874$ [rad/s].

First, we consider controllability of both configurations without fault states by using the same control reference $\mathbf{u}_{ref} = [T \ \boldsymbol{\tau}]^T = [mg \ 0 \ 0 \ 0]^T$. As it can be seen from Table 4.2, both versions of the hexacopter are inherently fault-tolerant with respect to a single DC motor failure. For this reason, we consider different double-fault cases (left columns in Tables 4.3 and 4.4) and the cases where the hovering point is stabilizable but not controllable when the reference is used in the form $\mathbf{u}_{ref} = [T \ \boldsymbol{\tau}_x \ \boldsymbol{\tau}_y]^T = [mg \ 0 \ 0]^T$ (right columns in Tables 4.3 and 4.4). Although the hexacopter may lose controllability, the latter case is important to be examined since a safety landing can be performed which can protect the vehicle and its equipment from potential damage.

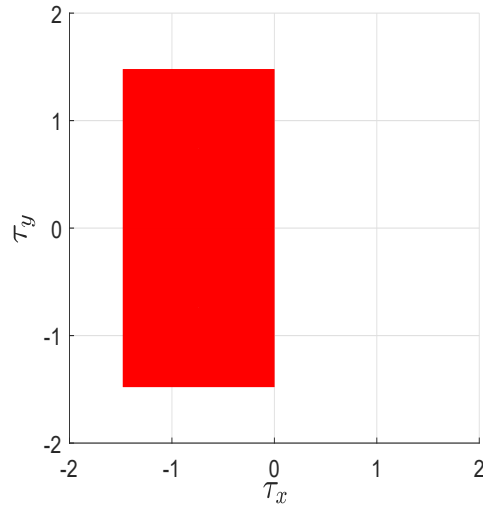
From the results presented in Tables 4.3 and 4.4 related to the two different hexacopter orientation configurations, 80% of total double-fault cases lead to the loss of controllability (red color in the left columns), while 40% cases are unstable without possibility for a safe landing (red colors in the right columns). This further means that the hexacopter will have a potential to continue the mission only in three cases (green color in the left columns) and to be safe in 60% (green color in right columns). One can also conclude that the hexacopter is single-fault-tolerant, while it is quite sensitive to double faults in terms of mission execution. However, it possesses a certain level of safety robustness. Since the obtained results are similar, there is no advantage of using any particular hexacopter configuration over the other one.

4.3.2 Fault-dependent controllability analysis for an octocopter system

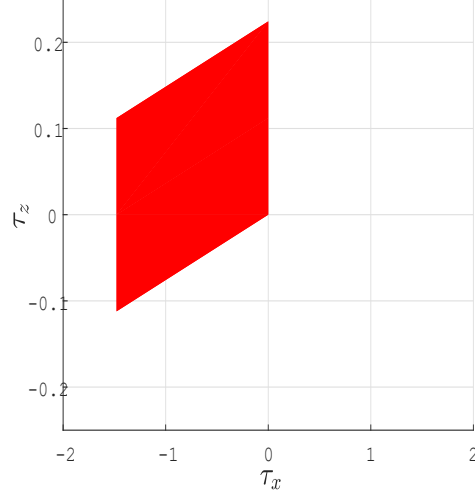
TABLE 4.1

Quadcopter: Analysis of single-fault cases.

Fault	$e_p = u_{ref} - A\Omega_s$
Motor M_1	$[0.0 \quad -0.03 \quad 0.0 \quad 0.21]^T$
Motor M_2	$[0.0 \quad 0.0 \quad 0.03 \quad -0.21]^T$
Motor M_3	$[0.0 \quad 0.03 \quad 0.0 \quad 0.21]^T$
Motor M_4	$[0.0 \quad 0.0 \quad -0.03 \quad -0.21]^T$

**FIGURE 4.7**

The projection of torques τ_x and τ_y onto the plane $T = mg$ along its orthogonal direction for a PNPNPNP octocopter configuration structure with a fault state related to the DC motor M_1 .

**FIGURE 4.8**

The projection of torques τ_x and τ_z onto the plane $T = mg$ along its orthogonal direction a PNPNPNP octocopter configuration structure with a fault state related to the DC motor M_1 .

TABLE 4.2

Hexacopter: Analysis of single-fault cases for the PNPNPN and PPNNPN configurations.

Fault	e_p for the PNPNPN	e_p for the PPNNPN
M_1	$\begin{bmatrix} 0.0 & 0.0 & 0.0 & 0.0 \end{bmatrix}^T$	$\begin{bmatrix} 0.0 & 0.0 & 0.0 & 0.0 \end{bmatrix}^T$
M_2	$\begin{bmatrix} 0.0 & 0.0 & 0.0 & 0.0 \end{bmatrix}^T$	$\begin{bmatrix} 0.0 & 0.0 & 0.0 & 0.0 \end{bmatrix}^T$
M_3	$\begin{bmatrix} 0.0 & 0.0 & 0.0 & 0.0 \end{bmatrix}^T$	$\begin{bmatrix} 0.0 & 0.0 & 0.0 & 0.0 \end{bmatrix}^T$
M_4	$\begin{bmatrix} 0.0 & 0.0 & 0.0 & 0.0 \end{bmatrix}^T$	$\begin{bmatrix} 0.0 & 0.0 & 0.0 & 0.0 \end{bmatrix}^T$
M_5	$\begin{bmatrix} 0.0 & 0.0 & 0.0 & 0.0 \end{bmatrix}^T$	$\begin{bmatrix} 0.0 & 0.0 & 0.0 & 0.0 \end{bmatrix}^T$
M_6	$\begin{bmatrix} 0.0 & 0.0 & 0.0 & 0.0 \end{bmatrix}^T$	$\begin{bmatrix} 0.0 & 0.0 & 0.0 & 0.0 \end{bmatrix}^T$

TABLE 4.3

Hexacopter: Analysis of double-fault cases for the PNPNP configuration.

Fault	$e_p = [0 \ 0 \ 0 \ 0]^T$	$e_p = [0 \ 0 \ 0]^T$
M_{12}	$[0.0 \ -0.44 \ 0.25 \ 0.0]^T$	$[0.0 \ -0.44 \ 0.25]^T$
M_{14}	$[0.0 \ 0.0 \ 0.03 \ 0.13]^T$	$[0.0 \ 0.0 \ 0.0]^T$
M_{14}	$[0.0 \ 0.0 \ 0.0 \ 0.0]^T$	$[0.0 \ 0.0 \ 0.0]^T$
M_{15}	$[0.0 \ -0.2 \ 0.0 \ 0.12]^T$	$[0.0 \ 0.0 \ 0.0]^T$
M_{16}	$[0.0 \ -0.6 \ -0.3 \ 0.0]^T$	$[0.0 \ -0.44 \ -0.25]^T$
M_{23}	$[0.0 \ 0.0 \ 0.51 \ 0.0]^T$	$[0.0 \ 0.5 \ 0.0]^T$
M_{24}	$[0.0 \ 0.24 \ 0.42 \ -0.13]^T$	$[0.0 \ 0.0 \ 0.0]^T$
M_{25}	$[0.0 \ 0.0 \ 0.0 \ 0.0]^T$	$[0.0 \ 0.0 \ 0.0]^T$
M_{26}	$[0.0 \ -0.04 \ 0.0 \ -0.12]^T$	$[0.0 \ 0.0 \ 0.0]^T$
M_{34}	$[0.0 \ 0.64 \ 0.36 \ 0.0]^T$	$[0.0 \ 0.44 \ 0.25]^T$
M_{35}	$[0.0 \ 0.04 \ 0.0 \ 0.12]^T$	$[0.0 \ 0.0 \ 0.0]^T$
M_{36}	$[0.0 \ 0.0 \ 0.0 \ 0.0]^T$	$[0.0 \ 0.0 \ 0.0]^T$
M_{45}	$[0.0 \ 0.04 \ -0.25 \ 0.12]^T$	$[0.0 \ 0.61 \ -0.35]^T$
M_{46}	$[0.0 \ 0.02 \ -0.03 \ -0.12]^T$	$[0.0 \ 0.0 \ 0.0]^T$
M_{56}	$[0.0 \ 0.0 \ -0.5 \ 0.0]^T$	$[0.0 \ 0.0 \ -0.51]^T$

TABLE 4.4

Hexacopter: Analysis of double-fault cases for the PPNNPN configuration.

Fault	$e_p = [0 \ 0 \ 0 \ 0]^T$	$e_p = [0 \ 0 \ 0]^T$
M_{12}	$[0.0 \ -0.43 \ 0.27 \ 0.18]^T$	$[0.0 \ -0.44 \ 0.25]^T$
M_{13}	$[0.0 \ 0.0 \ 0.0 \ 0.0]^T$	$[0.0 \ 0.0 \ 0.0]^T$
M_{14}	$[0.0 \ 0.0 \ 0.0 \ 0.0]^T$	$[0.0 \ 0.0 \ 0.0]^T$
M_{15}	$[0.0 \ 0.0 \ -0.01 \ 0.07]^T$	$[0.0 \ 0.0 \ 0.0]^T$
M_{16}	$[0.0 \ -0.44 \ -0.25 \ -0.15]^T$	$[0.0 \ -0.44 \ -0.25]^T$
M_{23}	$[0.0 \ 0.0 \ 0.51 \ 0.0]^T$	$[0.0 \ 0.0 \ 0.5]^T$
M_{24}	$[0.0 \ 0.0 \ 0.0 \ 0.0]^T$	$[0.0 \ 0.0 \ 0.0]^T$
M_{25}	$[0.0 \ 0.0 \ 0.0 \ 0.04]^T$	$[0.0 \ 0.0 \ 0.0]^T$
M_{26}	$[0.0 \ 0.0 \ 0.0 \ -0.05]^T$	$[0.0 \ 0.0 \ 0.0]^T$
M_{34}	$[0.0 \ 0.43 \ 0.27 \ -0.02]^T$	$[0.0 \ 0.44 \ 0.25]^T$
M_{35}	$[0.0 \ 0.0 \ 0.0 \ 0.05]^T$	$[0.0 \ 0.0 \ 0.0]^T$
M_{36}	$[0.0 \ 0.0 \ 0.0 \ -0.05]^T$	$[0.0 \ 0.0 \ 0.0]^T$
M_{45}	$[0.0 \ 0.44 \ -0.25 \ 0.14]^T$	$[0.0 \ 0.44 \ -0.25]^T$
M_{46}	$[0.0 \ 0.0 \ 0.0 \ -0.08]^T$	$[0.0 \ 0.0 \ 0.0]^T$
M_{56}	$[0.0 \ -0.51 \ 0.0 \ 0.0]^T$	$[0.0 \ 0.0 \ -0.51]^T$

In this subsection we address two different octocopter configuration structures, the PNPNPNP and the PPNNPPNN. The octocopters are designed based on the following parameters [59] $m_o = 1.8$ [kg], $l = 0.211$ [m], $I_{xx} = I_{yy} = 0.0429$ [kgm²], $I_{zz} = 0.0748$ [kgm²], $I_{zzm} = 2 \cdot 10^{-5}$ [kgm²], $b = 8.5485 \cdot 10^{-6}$ [$\frac{Ns^2}{rad^2}$], $d = 1.3678 \cdot 10^{-7}$ [$\frac{Nms^2}{rad^2}$], $\omega_{max} = 874$ [rad/s].

The analysis of single-fault cases for both considered octocopter configurations is presented in Table 4.5, while for double-fault cases in Tables 4.6 and 4.7. It is evident that both octocopter configurations are fully insensitive with respect to all single failures in terms of their potential to continue the mission execution. From the results presented in Tables 4.6 related to the PNPNPNP configuration, 28% of total double-fault cases lead to the loss of controllability (red color in the left column), while there are no unstable cases without possibility for a safe landing. This means that this octocopter configuration will have a potential to continue the mission in 72% of cases (green color in the left column) and to be safe in 100% (green color in the right column). For the hexacopter PPNNPPNN configuration we have 14% of controllability loss, no unstable cases, 86% potential to continue mission and 100% safety (see Table 4.7). The obtained conclusions are the same as those obtained in [67].

TABLE 4.5

Octocopter: Analysis of single-fault cases for the PNPNPNN and PPN-NPPNN configurations.

Fault	e_p for the PNPNPNN	e_p for the PPNNPPNN
M_1	$[0.0 \ 0.0 \ 0.0 \ 0.0]^T$	$[0.0 \ 0.0 \ 0.0 \ 0.0]^T$
M_2	$[0.0 \ 0.0 \ 0.0 \ 0.0]^T$	$[0.0 \ 0.0 \ 0.0 \ 0.0]^T$
M_3	$[0.0 \ 0.0 \ 0.0 \ 0.0]^T$	$[0.0 \ 0.0 \ 0.0 \ 0.0]^T$
M_4	$[0.0 \ 0.0 \ 0.0 \ 0.0]^T$	$[0.0 \ 0.0 \ 0.0 \ 0.0]^T$
M_5	$[0.0 \ 0.0 \ 0.0 \ 0.0]^T$	$[0.0 \ 0.0 \ 0.0 \ 0.0]^T$
M_6	$[0.0 \ 0.0 \ 0.0 \ 0.0]^T$	$[0.0 \ 0.0 \ 0.0 \ 0.0]^T$
M_7	$[0.0 \ 0.0 \ 0.0 \ 0.0]^T$	$[0.0 \ 0.0 \ 0.0 \ 0.0]^T$
M_8	$[0.0 \ 0.0 \ 0.0 \ 0.0]^T$	$[0.0 \ 0.0 \ 0.0 \ 0.0]^T$

TABLE 4.6

Octocopter: Analysis of double-fault cases for the PNPNPNN configuration.

Fault	$e_p = [0 \ 0 \ 0 \ 0]^T$	$e_p = [0 \ 0 \ 0]^T$
M_{12}	$[0.0 \ 0.0 \ 0.0 \ 0.0]^T$	$[0.0 \ 0.0 \ 0.0]^T$
M_{13}	$[0.0 \ 0.0 \ 0.0 \ 0.01]^T$	$[0.0 \ 0.0 \ 0.0]^T$
M_{14}	$[0.0 \ 0.0 \ 0.0 \ 0.0]^T$	$[0.0 \ 0.0 \ 0.0]^T$
M_{15}	$[0.0 \ 0.0 \ 0.0 \ 0.0]^T$	$[0.0 \ 0.0 \ 0.0]^T$
M_{16}	$[0.0 \ 0.0 \ 0.0 \ 0.0]^T$	$[0.0 \ 0.0 \ 0.0]^T$
M_{17}	$[0.0 \ 0.0 \ 0.0 \ 0.01]^T$	$[0.0 \ 0.0 \ 0.0]^T$
M_{18}	$[0.0 \ 0.0 \ 0.0 \ 0.0]^T$	$[0.0 \ 0.0 \ 0.0]^T$
M_{23}	$[0.0 \ 0.0 \ 0.0 \ 0.0]^T$	$[0.0 \ 0.0 \ 0.0]^T$
M_{24}	$[0.0 \ 0.0 \ 0.0 \ -0.01]^T$	$[0.0 \ 0.0 \ 0.0]^T$
M_{25}	$[0.0 \ 0.0 \ 0.0 \ 0.0]^T$	$[0.0 \ 0.0 \ 0.0]^T$
M_{26}	$[0.0 \ 0.0 \ 0.0 \ 0.0]^T$	$[0.0 \ 0.0 \ 0.0]^T$
M_{27}	$[0.0 \ 0.0 \ 0.0 \ 0.0]^T$	$[0.0 \ 0.0 \ 0.0]^T$
M_{28}	$[0.0 \ 0.0 \ 0.0 \ 0.01]^T$	$[0.0 \ 0.0 \ 0.0]^T$
M_{34}	$[0.0 \ 0.0 \ 0.0 \ 0.0]^T$	$[0.0 \ 0.0 \ 0.0]^T$
M_{35}	$[0.0 \ 0.0 \ 0.0 \ 0.01]^T$	$[0.0 \ 0.0 \ 0.0]^T$
M_{36}	$[0.0 \ 0.0 \ 0.0 \ 0.0]^T$	$[0.0 \ 0.0 \ 0.0]^T$
M_{37}	$[0.0 \ 0.0 \ 0.0 \ 0.0]^T$	$[0.0 \ 0.0 \ 0.0]^T$
M_{38}	$[0.0 \ 0.0 \ 0.0 \ 0.0]^T$	$[0.0 \ 0.0 \ 0.0]^T$
M_{45}	$[0.0 \ 0.0 \ 0.0 \ 0.0]^T$	$[0.0 \ 0.0 \ 0.0]^T$
M_{46}	$[0.0 \ 0.0 \ 0.0 \ -0.01]^T$	$[0.0 \ 0.0 \ 0.0]^T$
M_{47}	$[0.0 \ 0.0 \ 0.0 \ 0.0]^T$	$[0.0 \ 0.0 \ 0.0]^T$
M_{48}	$[0.0 \ 0.0 \ 0.0 \ 0.0]^T$	$[0.0 \ 0.0 \ 0.0]^T$
M_{56}	$[0.0 \ 0.0 \ 0.0 \ 0.0]^T$	$[0.0 \ 0.0 \ 0.0]^T$
M_{57}	$[0.0 \ 0.0 \ 0.0 \ 0.01]^T$	$[0.0 \ 0.0 \ 0.0]^T$
M_{58}	$[0.0 \ 0.0 \ 0.0 \ 0.0]^T$	$[0.0 \ 0.0 \ 0.0]^T$
M_{67}	$[0.0 \ 0.0 \ 0.0 \ 0.0]^T$	$[0.0 \ 0.0 \ 0.0]^T$
M_{68}	$[0.0 \ 0.0 \ 0.0 \ -0.01]^T$	$[0.0 \ 0.0 \ 0.0]^T$
M_{78}	$[0.0 \ 0.0 \ 0.0 \ 0.0]^T$	$[0.0 \ 0.0 \ 0.0]^T$

TABLE 4.7

Octocopter: Analysis of double-fault cases for the PPNNPPNN configuration.

Fault	$e_p = [0 \ 0 \ 0 \ 0]^T$	$e_p = [0 \ 0 \ 0]^T$
M_{12}	$[0.0 \ 0.0 \ 0.0 \ 0.13]^T$	$[0.0 \ 0.0 \ 0.0]^T$
M_{13}	$[0.0 \ 0.0 \ 0.0 \ 0.0]^T$	$[0.0 \ 0.0 \ 0.0]^T$
M_{14}	$[0.0 \ 0.0 \ 0.0 \ 0.0]^T$	$[0.0 \ 0.0 \ 0.0]^T$
M_{15}	$[0.0 \ 0.0 \ 0.0 \ 0.0]^T$	$[0.0 \ 0.0 \ 0.0]^T$
M_{16}	$[0.0 \ 0.0 \ 0.0 \ 0.0]^T$	$[0.0 \ 0.0 \ 0.0]^T$
M_{17}	$[0.0 \ 0.0 \ 0.0 \ 0.0]^T$	$[0.0 \ 0.0 \ 0.0]^T$
M_{18}	$[0.0 \ 0.0 \ 0.0 \ 0.0]^T$	$[0.0 \ 0.0 \ 0.0]^T$
M_{23}	$[0.0 \ 0.0 \ 0.0 \ 0.0]^T$	$[0.0 \ 0.0 \ 0.0]^T$
M_{24}	$[0.0 \ 0.0 \ 0.0 \ 0.0]^T$	$[0.0 \ 0.0 \ 0.0]^T$
M_{25}	$[0.0 \ 0.0 \ 0.0 \ 0.0]^T$	$[0.0 \ 0.0 \ 0.0]^T$
M_{26}	$[0.0 \ 0.0 \ 0.0 \ 0.0]^T$	$[0.0 \ 0.0 \ 0.0]^T$
M_{27}	$[0.0 \ 0.0 \ 0.0 \ 0.0]^T$	$[0.0 \ 0.0 \ 0.0]^T$
M_{28}	$[0.0 \ 0.0 \ 0.0 \ 0.0]^T$	$[0.0 \ 0.0 \ 0.0]^T$
M_{34}	$[0.0 \ 0.01 \ 0.02 \ -0.13]^T$	$[0.0 \ 0.0 \ 0.0]^T$
M_{35}	$[0.0 \ 0.0 \ 0.0 \ 0.0]^T$	$[0.0 \ 0.0 \ 0.0]^T$
M_{36}	$[0.0 \ 0.0 \ 0.0 \ 0.0]^T$	$[0.0 \ 0.0 \ 0.0]^T$
M_{37}	$[0.0 \ 0.0 \ 0.0 \ 0.0]^T$	$[0.0 \ 0.0 \ 0.0]^T$
M_{38}	$[0.0 \ 0.0 \ 0.0 \ 0.0]^T$	$[0.0 \ 0.0 \ 0.0]^T$
M_{45}	$[0.0 \ 0.0 \ 0.0 \ 0.0]^T$	$[0.0 \ 0.0 \ 0.0]^T$
M_{46}	$[0.0 \ 0.0 \ 0.0 \ 0.0]^T$	$[0.0 \ 0.0 \ 0.0]^T$
M_{47}	$[0.0 \ 0.0 \ 0.0 \ 0.0]^T$	$[0.0 \ 0.0 \ 0.0]^T$
M_{48}	$[0.0 \ 0.0 \ 0.0 \ 0.0]^T$	$[0.0 \ 0.0 \ 0.0]^T$
M_{56}	$[0.0 \ 0.02 \ -0.01 \ 0.13]^T$	$[0.0 \ 0.0 \ 0.0]^T$
M_{57}	$[0.0 \ 0.0 \ 0.0 \ 0.0]^T$	$[0.0 \ 0.0 \ 0.0]^T$
M_{58}	$[0.0 \ 0.0 \ 0.0 \ 0.0]^T$	$[0.0 \ 0.0 \ 0.0]^T$
M_{67}	$[0.0 \ 0.0 \ 0.0 \ 0.0]^T$	$[0.0 \ 0.0 \ 0.0]^T$
M_{68}	$[0.0 \ 0.0 \ 0.0 \ 0.0]^T$	$[0.0 \ 0.0 \ 0.0]^T$
M_{78}	$[0.0 \ -0.01 \ -0.03 \ -0.13]^T$	$[0.0 \ 0.0 \ 0.0]^T$

5

Risk-sensitive motion planning

CONTENTS

5.1	Presentation of the admissible set of thrust force and torques with a set of inequality constraints	67
5.2	Selected optimization framework for motion planning	68
5.3	Risk-sensitive motion planner based on mission-related fault-tolerant analysis	70
5.4	Simulation results	72

This section presents an idea how to construct a motion planner for an octo-copter system based on the admissible set of thrust force and torques obtained through fault-dependent maneuverability analysis presented in Section 4. We present a risk-sensitive (or risk-aware) motion-planning algorithm capable of taking into account risks during the planning stage by means of mission-related fault-tolerant analysis. We showed in [61] that the approach was less conservative in terms of selected performance measures than a conservative risk planner (or risk-averse) that assumed that the considered fault would certainly occur during the mission execution. On the other hand, the risk-sensitive motion planner is also readier for accepting failures during the mission execution than the risk-Ignorant approach (or risk-prone) that assumes no failure will occur. In this section, we describe this approach and present the obtained results.

5.1 Presentation of the admissible set of thrust force and torques with a set of inequality constraints

As shown in Chapter 4, the admissible set for thrust force and torques can be determined depending on the number of DC motors used, the orientation configuration and the states of DC motors (with or without faults). This admissible set has a convex polytope-like form in four-dimensional space.

Each of the outer sides of the polytope can be represented by its related

hyper-plane based on the four points that form that side, that is:

$$\mathbf{a}T + \mathbf{b}\tau_x + \mathbf{c}\tau_y + \mathbf{d}\tau_z \leq \mathbf{e}, \quad (5.1)$$

where \mathbf{a} , \mathbf{b} , \mathbf{c} , \mathbf{d} and \mathbf{e} are the slope coefficients of the individual axes.

Since the polytope-like admissible set is composed of a large number of such hyper-planes, it can be represented as a set of inequalities that fully describes the admissible set of thrust force and torques for each specific MAV design. For instance, for a healthy PNPNPNP octocopter system, it turned out that the related polytope can be described by 617 inequalities. In case any of DC motor is in a fault state, the number of inequalities decreases, while in an extreme case when all DC motors are in failure modes, the admissible set is reduced to a single point at origin, that is $u_{ref} = [T \ \tau_x \ \tau_y \ \tau_z] = [0 \ 0 \ 0 \ 0]$, in which the system is fully uncontrollable.

The obtained inequalities can be further used in motion planning to generate a feasible trajectory that depends on the initial admissible set (i.e., the resulting polytope) of thrust force and torques. In the next section, we describe a risk-sensitive planner (RSP) based on a careful selection of some of the inequalities that describe the admissible set (only a few of them), where the selection process depends on the required mission.

5.2 Selected optimization framework for motion planning

In Chapter 3 it is shown that for the reference trajectory position tracking, the functions representing the coordinates x and y must be at least four times differentiable, while the functions representing the heights z and orientations ψ are at least twice differentiable. The references for ϕ and θ orientation coordinates are obtained as an output of controlling the x and y position coordinates. Accordingly, the height z and orientation coordinates ψ behave as double integrators, that is

$$\ddot{q}, \quad (5.2)$$

and the x and y position coordinates can be approximated by a quadruple integrator:

$$\cdots \ddot{q}, \quad (5.3)$$

where $q = [x \ y \ z \ \psi]$, \dot{q} and \ddot{q} represent the generalized coordinates, velocity and acceleration, respectively.

The minimization of acceleration (5.2) and snap (5.3) directly yields the minimization of the generalized forces acting on the system. This further results in the minimization of energy consumption while taking into account the constraints imposed on the trajectory. This consequently means that the battery

consumption during the mission will be minimal. Detailed description of motion planning based on minimal acceleration and snap can be found in [47].

For this reason, motion planning problem can be described as a fixed finite-time optimization problem given as

$$\begin{aligned}
 & \underset{0 \leq t \leq T}{\text{minimize}} (\|\ddot{\mathbf{q}}\|^2) \\
 & \text{subject to} \\
 & \quad q_{\min} \leq q \leq q_{\max} \\
 & \quad \dot{q}_{\min} \leq \dot{q} \leq \dot{q}_{\max} \\
 & \quad \ddot{q}_{\min} \leq \ddot{q} \leq \ddot{q}_{\max},
 \end{aligned} \tag{5.4}$$

where the fixed finite-time represents the mission execution time T . The waypoints, as part of the given mission, through which the octocopter is supposed to pass should also be included in the optimization framework as desired constraints. One way to include these constraints is to impose hard constraints into the optimization. To ensure that the planner can be risk-averse, if necessary, we need to allow the motion planner to be capable of generating trajectories that may deviate from the waypoints which are designed for the selected mission. The deviation from the waypoints can be also used as a performance measure for the given mission. To do so, we include these constraints into the objective function by penalizing large deviations from the given waypoints as

$$\begin{aligned}
 & \underset{0 \leq t \leq T}{\text{minimum}} (\|\ddot{\mathbf{q}}\|^2 + \sum_i \alpha_i (\|q - q_i\|^2)) \\
 & \text{subject to} \\
 & \quad q_{\min} \leq q \leq q_{\max} \\
 & \quad \dot{q}_{\min} \leq \dot{q} \leq \dot{q}_{\max} \\
 & \quad \ddot{q}_{\min} \leq \ddot{q} \leq \ddot{q}_{\max},
 \end{aligned} \tag{5.5}$$

where the weights $0 \leq \alpha_i \leq 1$ are used to describe how important it is to pass through the waypoints q_i during the mission execution. For the purpose of this presentation, we set $\alpha_i = 1$ for all i .

Since (3.33), (3.37) and (3.25) provide the relations between T , τ_x , τ_y and τ_z and q , it is now possible to include the inequalities which describe the fault-dependent admissible set into the optimization framework. This gives the final form of the optimization framework used for the RSP motion planner:

$$\begin{aligned}
 & \underset{0 \leq t \leq T}{\text{minimize}} (\|\ddot{\mathbf{q}}\|^2 + \sum_i \alpha_i (\|q - q_i\|^2)) \\
 & \text{subject to} \\
 & \quad q_{\min} \leq q \leq q_{\max} \\
 & \quad \dot{q}_{\min} \leq \dot{q} \leq \dot{q}_{\max} \\
 & \quad aT + b\tau_x + c\tau_y + d\tau_z \leq e.
 \end{aligned} \tag{5.6}$$

In this way, the control admissible set obtained through the maneuverability analysis presented in Chapter 4 can be included in the optimization

framework as an additional set of constraints for each i , where i indicates the number of waypoints. It should be noted that the optimization requires \ddot{q} and \dot{q} which can be approximated by the first-order approximation as

$$\dot{q} = \frac{q(i) - q(i-1)}{\Delta t}, \quad (5.7)$$

where $\Delta t = T/N$, T the mission execution time, while N is the number of additional points included between waypoints. The role of these additional points is to increase a path resolution in order to provide a smooth reference path between waypoints.

In case the environment contains obstacles preventing the octocopter from crossing some given waypoints, it is also possible to impose an additional constraint to secure collision-free paths. Namely, it is necessary to define a safety distance R_{safe} to permit the system to stay distant from obstacles during the mission execution. The complete optimization framework that can be used for the RSP is given in the form

$$\begin{aligned} & \underset{0 \leq t \leq T}{\text{minimum}} (\|\ddot{q}\|^2 + \sum_i \alpha_i (\|q - q_i\|^2)), \\ & \text{subject to} \\ & \quad q_{min} \leq q \leq q_{max} \\ & \quad R_{safe} \leq |q - q_{ob}| \\ & \quad \dot{q}_{min} \leq \dot{q} \leq \dot{q}_{max} \\ & \quad aT + b\tau_x + c\tau_y + d\tau_z \leq e. \end{aligned} \quad (5.8)$$

where q_{ob} is the obstacle coordinate position.

In order to take into account any possible failure during the motion planning stage, one can include all constraints related to the admissible set of that failure. We call such a planner a risk-conservative planner (RCP). However, the RCP planner would be quite conservative, so in the following subsection we describe how to select some of the inequalities by carefully examining the given mission to form the RSP planner. It should be noted that the decision related to which failures and their related admissible sets to include should follow from the failure mode and effects analysis (FMEA) [67], [60].

5.3 Risk-sensitive motion planner based on mission-related fault-tolerant analysis

In addition to the RCP planner, the RSP planner proposed in [61] takes into account only relevant inequalities from the total number included in the

control admissible set. The classical planner which does not consider any possible failure is referred to as Risk-Ignorant Planer (RIP).

In this section we describe how to take possible failures into account during the motion planning stage by means of their related admissible sets. By doing so, we aim to include the associated risk into the planner in order to increase reliability of the mission execution in terms of satisfactory performance. This will be done at the cost of a much smaller performance deterioration than in case when the RCP planner is used for which all constraints related to risk-dependent admissible sets are included. As expected, the planner will require a bit more time to complete the mission than the RIP planner.

When a fault occurs the octocopter system may be in a position and orientation such that the control allocation is capable to produce desired thrust force and torques for the remaining DC motors without any effect on the mission performance. On the contrary, the octocopter may be in such position and orientation to significantly deteriorate the performance. The idea behind the proposed RSP motion planner is to carefully select a certain number of fault-dependent inequalities to retain the overall performance of a healthy system as much as possible. By doing so, the planner aims to minimally reduce the vehicle maneuverability (much less than in case of the RCP motion planner) in order to decrease probability of being in those states in which the vehicle might significantly deteriorate the performance when any of selected fault occurs.

The overall steps for mission-related fault-tolerant analysis and for designing the proposed RSP motion planner can be summarized as follows:

1. Select the failure modes of interest based on the FMEA analysis (e.g., single motor failures).
2. Determine the minimum mission execution time for the RIP motion planner to achieve a feasible solution (from those that secure passing through waypoints).
3. For all selected failure modes, determine the minimum mission execution times of the RCP motion planner to achieve feasible solutions.
4. Set the maximum time of all minimum times obtained in step 3 to be the mission time in order to ensure that the RCP planner provides feasible solutions for each failure modes.
5. Find all inequalities associated to the fault dependent admissible sets for each selected failure mode from step 1, which are not satisfied during the mission execution based on the RIP motion planner

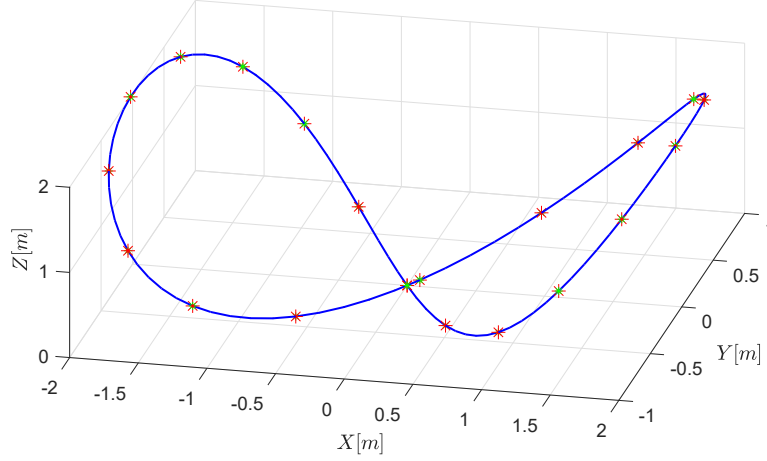
and the mission time obtained in step 4.

6. Form the final optimization framework for the RSP motion planner by including all constraints found in step 5 and determine the minimum mission execution time for the RSP motion planner to achieve a feasible solution. This optimization framework represents the proposed RSP motion planner.

The presented design steps can be explained as follows. First, we perform the FMEA analysis in order to find the most critical failure mode that will be taken into account during the planning stage (step 1). Second, we determine the minimum execution time for the RIP planner (step 2). The minimum mission execution time represents a time for which the optimization framework still gives a feasible solution, that is, the solution which ensures passing through the waypoints. Since the proposed design steps can be conducted off-line, that is before the mission execution, this minimum value can be easily found by incrementally decreasing the time and checking whether the related solution is feasible or not. Then, for all selected failure modes from step 1, we determine the minimum execution times (step 3) obtained with the RCP planner. In step 4, we select the worst-case (maximum time) from step 3 to be the mission time in order to ensure that all planners provide feasible solutions. This is also important for a fair comparison of all planners by means of the performance measured by deviation from the waypoints. Otherwise, some of the planners would be infeasible. In step 5, we first find the admissible sets for each failure mode and determine their related inequality sets. Then, we test the RIP motion planner, given the mission time from step 4, in order to find only those inequalities which are not possible to satisfy for the considered mission. To do so, we check the thrust force and the torques obtained by the RIP motion planner against the related admissible sets for each failure mode. In step 6, we form the final optimization framework by including a constraint set consisted of the inequalities extracted from step 5 and the admissible set of the healthy octocopter system.

5.4 Simulation results

The mission is defined in the form of Vivian curve as in preceding sections, in which 21 points have been generated uniformly along the curve to define the waypoints (Figure 5.1). For the optimization framework (5.8), we generate additional 10 points between each successive waypoints, which gives the total number of $N = 210$ points.

**FIGURE 5.1**

Uniform sampling of the Viviani curve with 21 points.

To test the quality of generated trajectories, we use two types of error, the first is related to the position e_R and the second to the orientation e_Ψ , as:

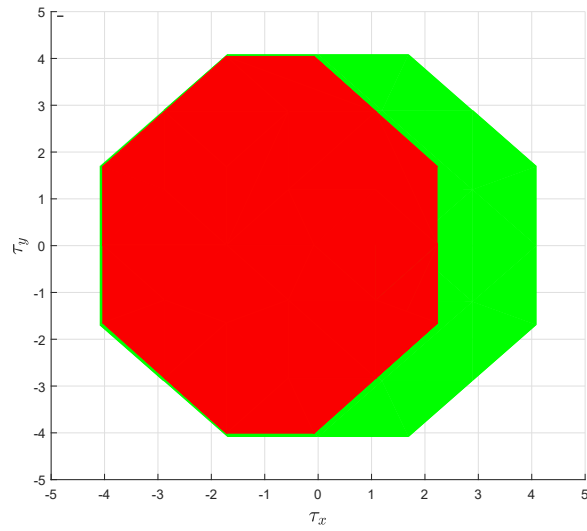
$$e_R = \sum_i \sqrt{(x_i - x_{ref_i})^2 + (y_i - y_{ref_i})^2 + (z_i - z_{ref_i})^2} \quad (5.9)$$

$$e_\Psi = \sum_i \sqrt{(\psi_i - \psi_{ref_i})^2}. \quad (5.10)$$

Case 1: First, we consider only a single failure occurred in the DC motor M_1 in order to take it into account in the motion planning stage (step 1 of the *RSP* planning algorithm). Fig. 5.2 shows the control admissible set obtained with the maneuverability analysis based on this failure. The obtained set is obviously reduced with respect to the admissible set for the system without failure consideration (the healthy octocopter system).

In steps 2 and 3 we determine the minimum times to get a feasible solution for the *RIP* motion planner, which is 16 [s], and for the *RCP* motion planner, which is 20 [s] (see Table 5.1).

In accordance to step 4, we then choose the mission time to be 20 [s] for the next step. In accordance with step 5, for the thrust forces and torques obtained by the *RIP* planner, we find all inequalities from the fault-dependent admissible set which are not satisfied during the mission execution. For the considered example, in the case of the *RIP* planner, the obtained thrust force and torques violate only two inequalities (out of 440 that describe the admissible set of thrust force and torques) in 111 cases related to 99 discrete positions along the mission curve (out of possible 210). By including only

**FIGURE 5.2**

Control input domain (projection onto plane $T = mg$) in case without any faults (green), and in case of M1 in fault state (red).

TABLE 5.1

Performance comparison between the RIP and RCP approaches (Case 1, steps 1, 2 and 3).

MAV	T [s]	$e_R[m]$	$e_R/N[m]$	$e_\Psi[rad]$	e_Ψ/N [rad]
<i>RIP</i>	16	0,0412	0,0019	4e-12	4e-13
<i>RCP</i>	20	0,0566	0,0027	1e-18	5e-21

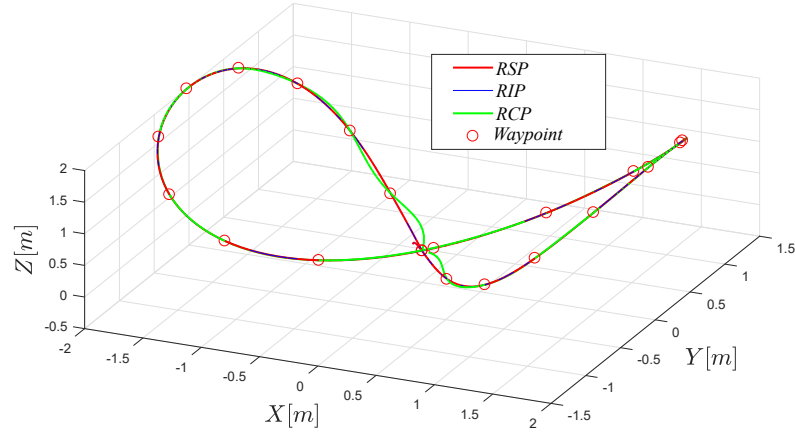
these two additional constraints into the final optimization (step 6), we get the RSP planner. One can observe that the RSP planner violates only one inequality constraint at only one position (see Table 5.2).

In order to fairly compare the results, the RIP planner is also executed for the mission time $T = 20$ [s]. The paths generated by all three planners are shown in Fig. 5.3. One can observe that the RSP and RIP planners generated almost the same path, while the RCP has slight deviations with respect to the mission waypoints. However, the detailed comparison of all three planners (RIP, RCP and RSP) for the maximum time obtained ($T = 20$, step 4), is given in Table 5.2. It can be seen that the RIP and RSP planners obtained similar performances, better than the RCP approach. On the other hand, the RIP planner violated the constraints in 51 positions, which is less than in case when the mission execution time was $T = 16$ [s] when there were 111 such positions. Unlike the RIP, the RSP violated only one inequality constraint at only one position (see Table 5.2).

In order to justify the use of the RSP instead of the RIP, we illustrate one example with $T = 20$ [s] and a failure occurred in the motor M_1 at $t = 8$ [s]. The resulting paths are shown in Fig. 5.4. One can observe that the RSP planner (red) has the smallest total deviation from the waypoints. The RCP (green) has the worst deviation before the failure occurs, which is expected since during this period the planner produces the most conservative paths. The RIP (blue) generates the path without deviations before that critical event, but the significant deviation appears after that moment.

To further compare the planners, we additionally introduce three types of errors. $e_{Rp}[m]$ and $e_{\Psi p}[rad]$ represent the first error type indicating position and orientation errors with respect to the mission waypoints. The second type of errors are $e_{RRef}[m]$ and $e_{\Psi Ref}[rad]$ which indicate the position and orientation errors with respect to the no-failure path, while the third type of errors, $e_{RRIP}[m]$ and $e_{\Psi RIP}[rad]$, are the position and orientation errors with respect to the no-failure path obtained with the RIP planner which represents an ideal path in case without failures. From Table 5.3, one can see that the RSP has the best overall performance.

Figs. 5.5, 5.6 i 5.7 show the tracking results and related errors for each coordinate during the mission execution. Fig. 5.5 clearly indicates the previous conclusion that the RIP planner experiences the problems immediately after the failure occurs ($t = 8s$). Namely, the octocopter needs several seconds to

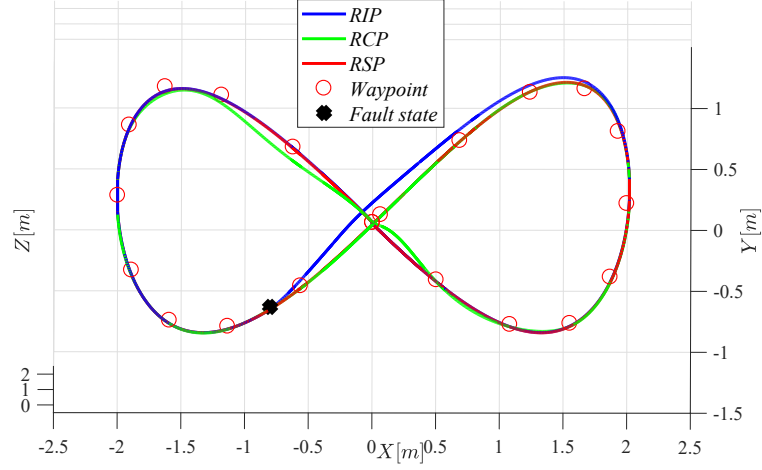
**FIGURE 5.3**

Paths generated using RIP, RCP, and RSP motion planners. The traversal time is 20 seconds..

TABLE 5.2

Performance comparison for RIP, RCP and RSP motion planners with traversal time $T=20s$ (Case 1, steps 5 and 6). .

Performance	T [s]	e_R [m]	e_Ψ [rad]	<i>violated constraints</i>
<i>RIP</i>	20	0,038	5e-19	51
<i>RCP</i>	20	0,057	1e-18	0
<i>RSP</i>	20	0,038	1,25e-18	1

**FIGURE 5.4**

Tracking of trajectories obtained using RIP, RCP, and RSP planners. The nominal traversal time is 20s, with the fault state at M1 occurring at $t = 8s$.

TABLE 5.3

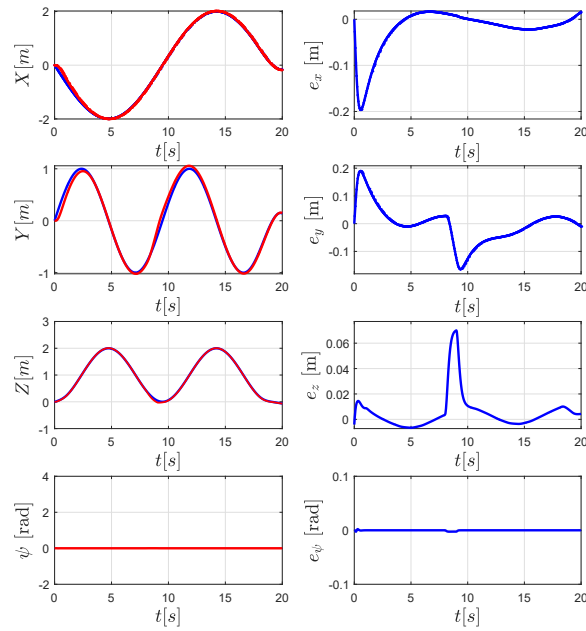
Performance comparison for RIP, RCP and RSP motion planners with traversal time $T=20s$ (Case 1, steps 5 and 6).

Perf.	$e_{Rp}[m]$	$e_{\Psi p}[rad]$	$e_{RRRef}[m]$	$e_{\Psi Ref}[rad]$	$e_{RRIP}[m]$	$e_{\Psi RIP}[rad]$
<i>RIP</i>	1.75	0.251	1.29	-2.7e-3	1.29	-2.7e-3
<i>RCP</i>	1.55	2.56e-3	1.08	1.8e-3	1.41	-1.58e-2
<i>RSP</i>	1.44	-1.22e-2	0.86	-0.7e-5	1.01	2.9e-2

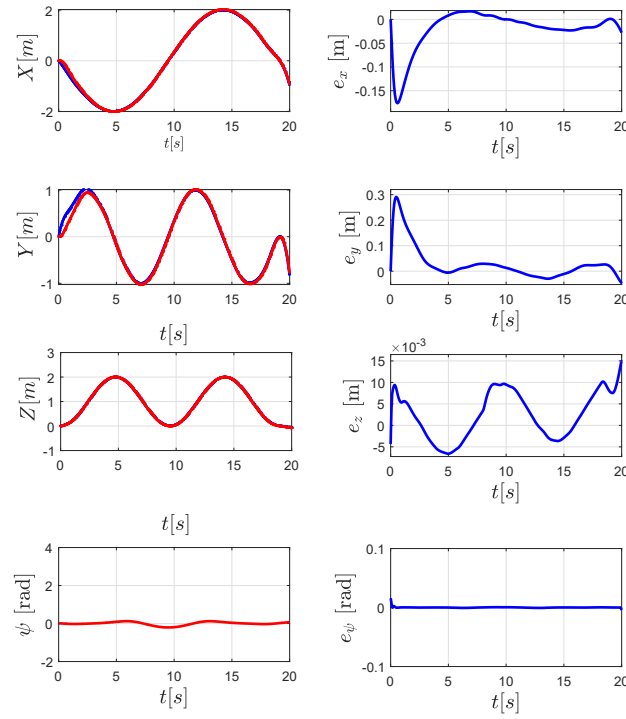
decrease the error with respect to y coordinate after the failure occurs. Fig. 5.6 shows the results obtained by the RCP planner. As previously stressed, the octocopter experiences the worst deviations before the failure occurs due to the conservative maneuvers used during the no-failure stage. As expected, the RSP planner (see Fig. 5.7) navigates the octocopter system to perceive the minimum deviation from the given waypoints during the whole mission duration.

Case 2: Consider now a double-fault case related to the motors M_1 and M_6 . Fig. 5.8 shows the control admissible set for this case (red), which is reduced with respect to the admissible set obtained without considering any fault state (green).

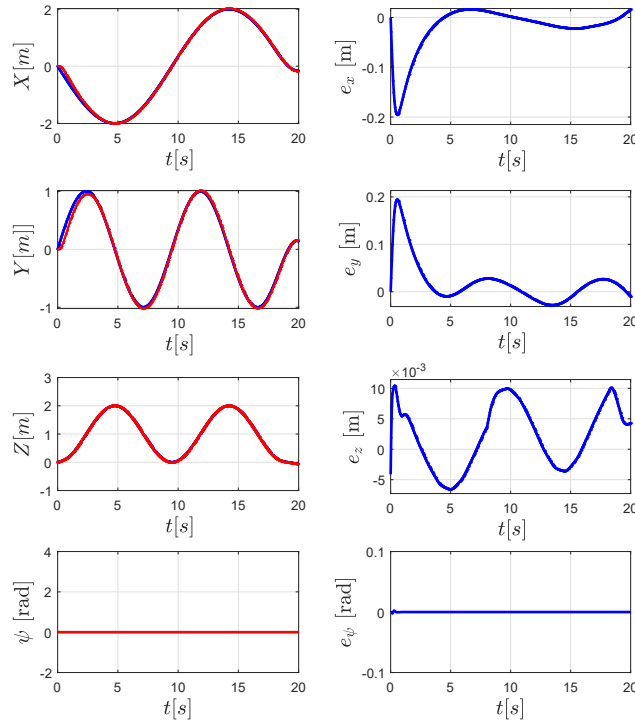
As expected, we can see from Table 5.4, that the RIP planner obtains the best performance. The RSP and RCP planner obtain similar performance, except that the RCP planner needs a bit more time ($T = 26s$ vs. $T = 18s$) to complete the mission. This is due to a more restrictive set of inequality con-

**FIGURE 5.5**

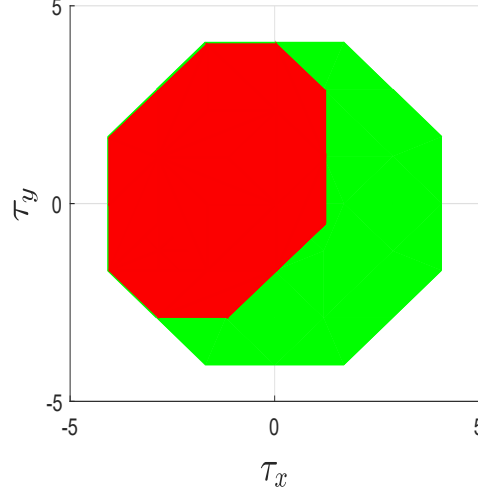
Tracking of Cartesian coordinates x , y , z orientation ψ and respective tracking errors e_x , e_y , e_z i e_ψ in case of trajectory generated by RIP planner. The traversal time is 20s, with the fault at M1 occurring at $t=8$ s.

**FIGURE 5.6**

Tracking of Cartesian coordinates x , y , z orientation ψ and respective tracking errors e_x , e_y , e_z and e_ψ in case of trajectory generated by RCP planner. The traversal time is 20s, with the fault at M1 occurring at $t=8$ s.

**FIGURE 5.7**

Tracking of Cartesian coordinates x , y , z and orientation ψ and respective tracking errors e_x , e_y , e_z and e_ψ in case of trajectory generated by *RSP* planner. The traversal time is 20s, with the fault at M1 occurring at $t=8$ s.

**FIGURE 5.8**

Control input domain (projection onto plane $T = mg$) in case without any faults (green), and in case of simultaneous faults at M1 and M6 (red).

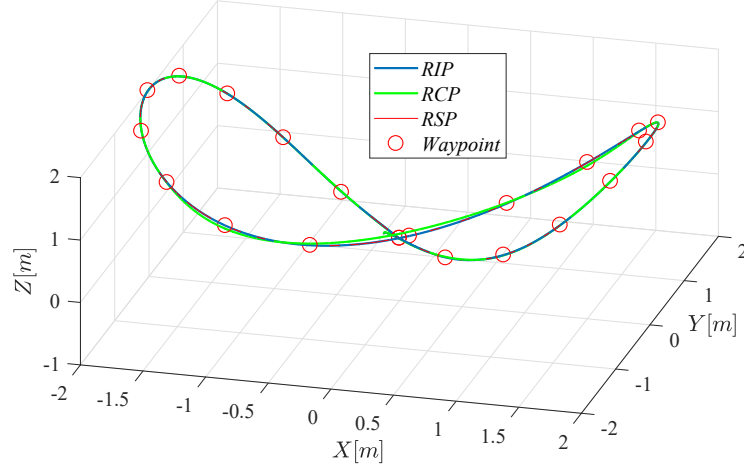
TABLE 5.4

Performance comparison for RIP, RCP and RSP motion planners in case of double fault, where their minimum respective traversal times are considered (Case 2, steps 2, 3, and 5).

Performance	T [s]	$e_R[m]$	$e_\Psi[rad]$	violated constraints
<i>RIP</i>	16	0,0412	4e-19	80
<i>RCPM16</i>	26	0,284	2e-17	0
<i>RSP</i>	18	0,234	1,2e-9	21

straints included in the optimization for the RCP planner. However, in the case when the execution time is set to the maximum time (see Table 5.4) obtained from these planners ($T = 26s$), the RIP planner violates fault-dependent inequality constraints 80 times at 73 positions, while the RSP motion planner only 21 times at 21 positions. This indicates that the RSP motion planner is readier than the RIP planner in case this double fault occurs, while it needs a bit more time than the RIP planner to complete the mission.

The planners are compared for the mission execution time $T = 26$ [s]. The paths generated by three considered planners are shown in Fig. 5.9, from which one can see that the smallest and largest deviations from the waypoints are obtained with the RIP and RCP planners, respectively.

**FIGURE 5.9**

Paths generated using RIP (without fault states), RCP (faults at M1 and M6), and RSP (faults at M1 and M6 – selected inequalities) motion planners. The traversal time is 26 seconds.

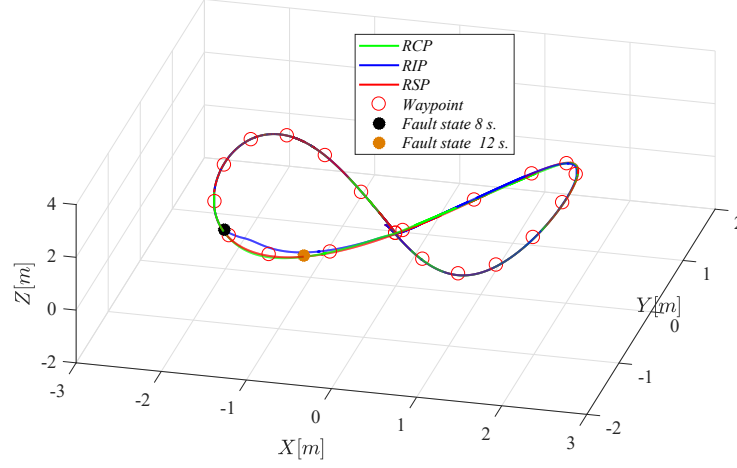
TABLE 5.5

Performance comparison for RIP, RCP and RSP motion planners in case of simultaneous fault at M1 and M6 (Case 2, steps 5 and 6). Traversal time is $T=26s$.

Perf.	$e_{Rp}[m]$	$e_{\Psi p}[rad]$	$e_{RRef}[m]$	$e_{\Psi Ref}[rad]$	$e_{RRIP}[m]$	$e_{\Psi RIP}[rad]$
<i>RIP</i>	1.32	5.6e-3	1.04	-3.8e-3	1.08	-3.9e-3
<i>RCP</i>	1.15	2.79e-3	0.72	-7.9e-4	0.85	-8.21e-4
<i>RSP</i>	1.01	2.38e-2	0.65	-2.9e-5	0.67	-3e-5

In order to fully compare the planners, we simulate the case when the motors M_1 and M_6 fail at $t = 8s$ and $t = 12s$, respectively. The obtained paths are shown in Fig. 5.10, while the overall performance is summarized in Table 5.5. It can be seen that the RSP planner obtains the best performance in comparison to the worst performance obtained by the RIP planner. The results are expected since the RIP planner does not take any information about motor failures into account during the planning stage.

It is also interesting to test the results such that the mission execution times for each planner are the same as in case when the considered fault does not occur, that is $T_{RIP} = 16s$, $T_{RCP} = 26s$ and $T_{RSP} = 16s$. The paths obtained by these three planners are shown in Fig. 5.11, while the performance is summarized in Table 5.6. One can derive the same conclusion and see that the RIP planner generates the worst deviation from the mission

**FIGURE 5.10**

Tracking of trajectories obtained using RIP, RCP, and RSP planners. The nominal traversal time is 26s, with the fault states at M1 and M6 occurring at $t=8s$ and $t=12s$ respectively.

TABLE 5.6

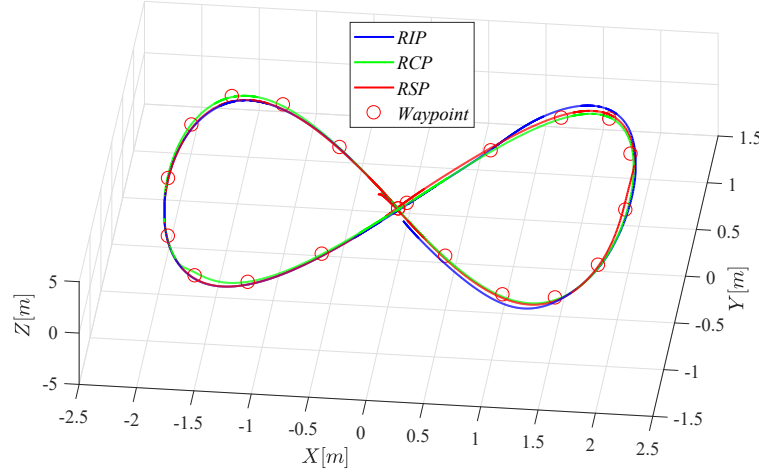
Performance comparison for RIP, RCP and RSP motion planners in case of simultaneous fault at M1 and M6 (Case 2, steps 5 and 6). Traversal times are $T=16s$, $26s$, and $18s$ respectively.

Performance	$e_{Rp}[m]$	$e_{\Psi p}[rad]$	$e_{RRef}[m]$	$e_{\Psi Ref}[rad]$
<i>RIP</i>	1.74	-7.65e-3	1.43	-7.8e-3
<i>RCP</i>	1.26	-7.65e-3	0.71	-1.3e-3
<i>RSP</i>	1.32	-7.6e-3	1.02	-2.8e-5

waypoints, while the RCP and RSP have the similar performance. However, the execution time of the RSP is much smaller than in case of the RCP planner. This means that the RSP generates the paths with good performance with mission execution times close to the one obtained with the RIP planner.

The similar analysis can be further conducted for different multiple-faults. However, every additional fault would substantially reduce the control admissible set which would further deteriorate the results of the RCP planner.

Case 3: In this case we address all eight possible single faults for an octocopter system. Table 5.7 shows the results obtained by the RIP, RSP as well as different variants of the RCP planner related to different single-faults, that is the $RCP-M_i$, $i = \overline{1..8}$. The $RCP-M_i$ planner takes into account

**FIGURE 5.11**

Tracking of trajectories obtained using RIP, RCP, and RSP planners. The traversal times are 16s, 26s and 18s respectively. The fault states at M1 and M6 occur at $t=8s$ and $t=12s$ respectively.

only the admissible set related to the fault of the motor M_i , meaning that the planner is conservatively prepared only for that fault. It should be noted that the RCP planner is not able to take all 8 single faults simultaneously into account during the planning stage since the final admissible set would be an empty set. However, the RSP planner is capable to address all M_i single faults simultaneously. As previously explained, this is possible since the RSP planner takes only a few inequality constraints for the admissible sets related to all M_i faults, in order to form the optimization framework. For this reason, the RSP is capable to provide a feasible solution, unlike the RCP planner.

One can observe from Table 5.7 that the RSP planner needs more time ($T = 28s$) to complete the mission in a satisfactory manner. This is due to the fact that it is the only planner that takes all 8 single-faults into account. However, for the mission execution time set to the maximum $T = 28s$, one can see from Table 5.8 [61] that the number of violated inequalities related to all single-fault admissible sets (M_i) was significantly smaller for the RSP motion planner with respect to other planners. As expected, the RIP planner violates the largest number of those constraints which makes it unprepared for any single-fault occurrence during the mission executions. It is worth mentioning that the constraints of the admissible set related to the motor M_3 are violated in a huge number except by the RCP- M_3 planner that takes into account those constraints in the planning stage. This is probably due to the selected mission which requires such maneuvers sensitive to those constraints. An additional

TABLE 5.7

Performance comparison between the RIP, RCP and RSP planners (Case 3. step 1, 2 and 3).

Performance	T [s]	$e_R[m]$	$e_R/N[m]$	$e_\Psi[rad]$	$e_\Psi/N[rad]$
<i>RIP</i>	16	0,0412	0,0019	4e-12	4e-13
<i>RCP</i> (M_1)	20	0,057	0,0027	1e-18	5e-21
<i>RCP</i> (M_2)	20	0,038	0,018	4e-18	2e-19
<i>RCP</i> (M_3)	20	0,038	0,018	7e-12	3,4e-13
<i>RCP</i> (M_4)	28	0,5	0,0238	1,4e-8	6,9e-10
<i>RCP</i> (M_5)	24	0,26	0,012	0,0012	5,9e-4
<i>RCP</i> (M_6)	24	0,43	0,021	9e-12	4,4e-13
<i>RCP</i> (M_7)	20	0,073	0,0035	1,5e-10	7,4e-12
<i>RCP</i> (M_8)	20	0,038	0,018	7e-12	3,4e-13
<i>RSP</i>	28	0,54	0,025	7e-6	3,5e-7

interesting observation regarding the admissible sets related to the motors M_2 and M_5 is that all planners have managed to satisfy all related constraints during the whole mission. Finally, as expected, all $RCP-M_i$ planners satisfy all constraints related to their own admissible sets M_i .

As in Case 1 and Case 2, the results are compared using the mission execution time obtained with step 3 of the RSP planning algorithm which is now set to $T = 28$ [s]. We have conducted 30 single-fault simulations for each planner, where a single fault has been randomly generated at a random time moment. The statistical results obtained for all previously considered errors are summarized in Table 5.9.

As expected, the RCP which was customized only to one particular single-fault, generates the worst statistical results, since the simulated single-failures could be linked to any motor. Moreover, two simulations based on the RCP planner were terminated since the octocopter became uncontrollable immediately after the fault occurred. One can also observe that the best statistical results have been obtained by the RSP planner, since it was inherently constructed to be prepared for any possible single fault.

Case 4: In the following set of scenarios, the octocopter has to pass through a narrow corridor, which is 1m long, with the square cross-section of dimensions 1m x 1m. The dimensions of the craft are 0,5m x 0,5m x 0,2m. For computing the collision free path, the RRT planning algorithm is used, where the octocopter is considered as a free-flying rigid body. RRT has generated 20 intermediate waypoints, which serve as milestones for the octocopter motion. Figure 5.12 depicts the corridor, the initial configuration (red), the final configuration (green) and the waypoints. This setup is used to test several scenarios. The first one (Case 4.1), the planning is performed using RIP, RCP and RSP planners. In a simulation scenario, we assume, no fault state

TABLE 5.8

The number of unsatisfied inequalities for RIP, RCP and RSP planners for each possible single fault state (M_i), with respect to feasible control inputs (Case 3, steps 4,5, and 6).

MAV	M_1	M_2	M_3	M_4	M_5	M_6	M_7	M_8
<i>RIP</i>	52	0	108	206	0	108	24	136
<i>RCP</i> (M_1)	0	0	107	179	0	89	20	116
<i>RCP</i> (M_2)	52	0	110	205	0	108	24	136
<i>RCP</i> (M_3)	53	0	0	185	0	87	23	137
<i>RCP</i> (M_4)	52	0	99	0	0	99	24	136
<i>RCP</i> (M_5)	52	0	101	197	0	99	24	136
<i>RCP</i> (M_6)	52	0	101	197	0	0	24	136
<i>RCP</i> (M_7)	52	0	101	191	0	95	0	134
<i>RCP</i> (M_8)	52	0	108	197	0	108	24	0
<i>RSP</i>	0	0	118	15	0	5	0	0

TABLE 5.9

Feasibility comparison for trajectories obtained using RIP, RCP and RSP planners, for each possible single fault state (M_i). The time instant of fault occurrence is random.

	<i>RIP</i>	<i>RCP</i>	<i>RSP</i>
Mean value ($e_{Rp}[m]$)	1,21	1,3	1,105
Standard deviation ($e_{Rp}[m]$)	7,44e-2	1,86e-1	3,98e-2
Mean value ($e_{\Psi p}[rad]$)	-2,28e-4	3,26e-2	4,42e-3
Standard deviationa ($e_{\Psi p}[rad]$)	1,63e-3	4,44e-2	8,93e-4
Mean value ($e_{RRef}[m]$)	0,738	0,743	0,608
Standard deviation ($e_{RRef}[m]$)	0,058	0,145	0,0506
Mean value ($e_{\Psi Ref}[rad]$)	8,133e-5	-3,74e-3	-9,93e-5
Standard deviation ($e_{\Psi Ref}[rad]$)	1,22e-3	5,43e-3	6,48e-4
Mean value($e_{RRIP}[m]$)	0,738	0,937	0,635
Standard deviationa ($e_{RRIP}[m]$)	0,058	0,257	0,056
Mean value($e_{\Psi RIP}[rad]$)	8,133e-5	-1,04e-2	-2,82e-3
Standard deviation ($e_{\Psi RIP}[rad]$)	1,22e-3	1,69e-2	6,48e-4

occurs. Following the steps of the RSP planner, the mission duration is set to 12s. For such setting, all three planners generate paths with the octocopter passing the narrow corridor without colliding with the walls. Figure (fali slika) shows the diagram of minimum distance between the octocopter and the corridor walls.

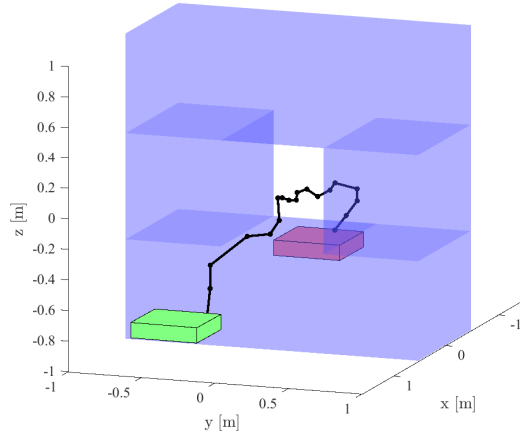
In Case 4.2, RCP planner anticipates the fault state at motor M_1 . In simulation, the actual fault occurs at motor M_1 at $t = 3$ s. The minimum distance diagram for all three planners is given in Figure 5.13. It can be noted that RCP and RSP planners enable collision-free motion, whereas the motion generated by the RIP planner causes collision of octocopter with the corridor wall. The fault is generated at the time when the octocopter enters the corridor and likely represents the most sensitive region within the whole mission. This can also be noted from the motion along the path generated by RCP and RSP planners, which are in this case identical. Though collision-free, the considered path comes rather close to the wall. When the fault occurs at the motor M_1 ($t = 3$ s), the maneuver performed by octocopter, according to the path planned by RIP, clearly does not compensate for the fault state. A significant deviation from the reference path occurs and the octocopter collides with the wall. On the other hand, RCP planner accounts for the fault state at M_1 . Therefore, when the specific fault occurs, it does not cause the deviation from the nominal path computed by RCP. A similar behavior is observed when the octocopter follows the path obtained by the RSP planner.

In scenario 4.3, the fault state occurs again at $t = 3$ s at motor M_1 , however, RCP planner anticipates the fault state at motor M_8 . Similarly, as in the previous case, octocopter collides with the wall in case of following the path generated by the RIP planner. On the other hand, the motions generated by RCP and RSP planners are collision-free (see Figure 5.14). The reason collision does not occur for the RCP-planned motion may be the fact that the control region implied by the possible fault state at M_8 prevents aggressive maneuvers near the entrance of the corridors. Thus, the octocopter may adapt to the actual fault at M_1 , though the fault at this motor has not been anticipated.

In case 4.4, a double fault occurs, at motors M_1 and M_4 , at $t = 3$ s and $t = 5$ s respectively. Only RSP planner generates the collision-free motion, while the paths computed by RIP and RCP are not feasible. The minimum distance diagram is shown in Figure 5.15.

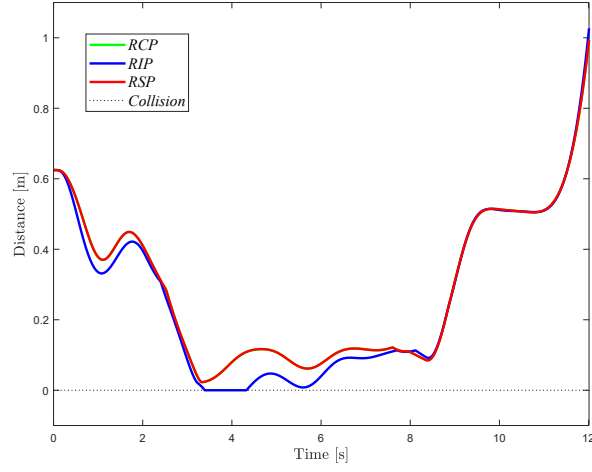
The case 4.5. assumes fault states at motors M_1 and M_4 , at $t = 5$ s and $t = 8$ s respectively. This time, all three planners generate collision-free motions. This is likely due to the fact that at $t = 5$ s, the octocopter is already inside the corridor, with ample clearance margins. Hence, even when the fault occurs, there is sufficient room for adjustment without causing collisions. The minimum distance diagram is shown in Figure 5.16.

Based on presented scenarios for motion planning through a narrow corridor, it can be seen that the RSP planner shows the best performance in cases of single and double fault states. For cases 4.1 and 4.5, all three planners show reliable performance. However, since we cannot predict the time of

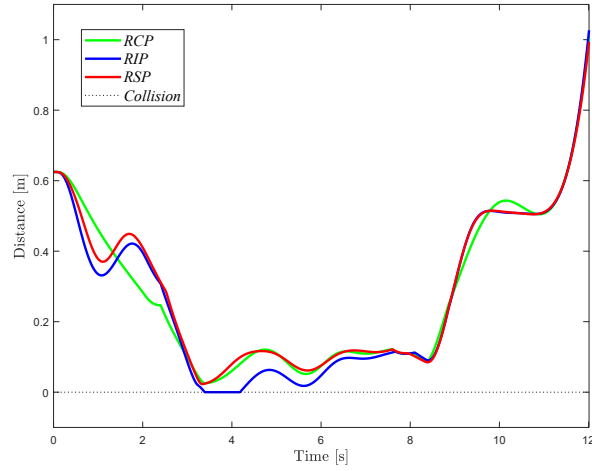
**FIGURE 5.12**

Octocopter motion through a narrow corridor (dimensions 1m x 1m x 1m). RRT algorithm is used for generating waypoints..

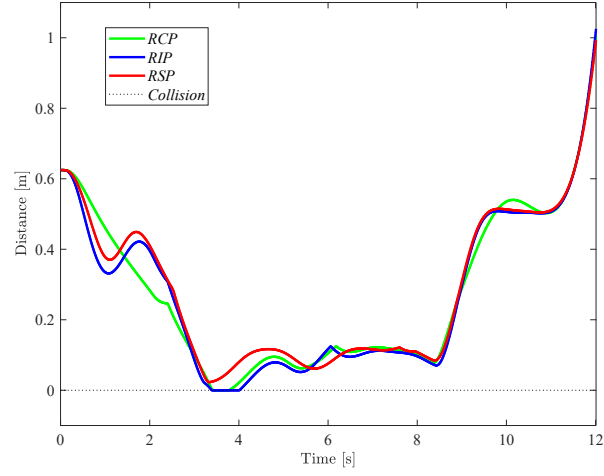
fault occurrence with certainty, or the maneuver performed by the craft at the time, the RSP-generated motion turns out to be most reliable. Clearly, this approach encourages those octocopter maneuvers that are the most beneficial to recovering the path following.

**FIGURE 5.13**

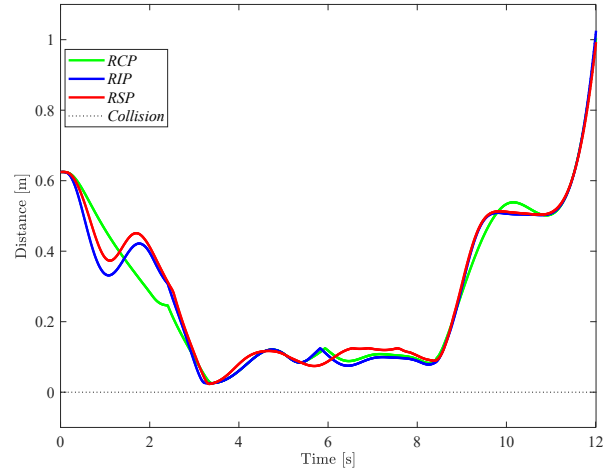
Octocopter motion through the corridor with a single fault state at M_1 at $t = 3$ s. RCP anticipates the fault state at M_1 .

**FIGURE 5.14**

Octocopter motion through the corridor with a single fault state at M_1 at $t = 3$ s. RCP anticipates the fault state at M_8 .

**FIGURE 5.15**

Octocopter motion through the corridor with a double fault states at M_1 and M_4 at $t = 3s$ and $t = 5s$ respectively. RCP anticipates the fault state at M_8 .

**FIGURE 5.16**

Octocopter motion through the corridor with a double fault states at M_1 and M_4 at $t = 5s$ and $t = 8s$ respectively. RCP anticipates the fault state at M_8 .

6

Conclusion

CONTENTS

This book includes all necessary ingredients to design control and motion planning algorithms for an autonomous octocopter system. Chapter 2 describes motion principles of an octocopter design and includes the octocopter kinematics and dynamics equations as well as motor dynamic models. It also provides a general octocopter state-space model upon which it is possible to construct a variety of control design algorithms.

Chapter 3 provides a fault-tolerant control, control allocation and a simple PD controller that controls the octocopter system to track the given reference position and orientation. In order to include information about potentially active fault states of DC motors into a control design, it is necessary to implement an algorithm that can include those information into the actuation matrix and adjust the control so that the octocopter system is still optimally controlled during such circumstances. The presented algorithm which is capable of identifying and isolating the active failures is based on the recursive least-squares algorithm. The information of the fault state identification is then fed to the control allocation algorithm which adapts the distribution of control signals only to the remaining active motors in order to achieve a feasible control whenever is possible. It is shown that the octocopter system based on such a control architecture is capable of achieving good performance in case all eight DC motors of the octocopter system are fully available. However, in case of a single motor failure, the control may be feasible but the tracking performance could be significantly deteriorated.

Chapter 4 introduces a fault-dependant controllability analysis which thoroughly examines the potential of an octocopter system to continue the mission execution under variety of possible fault states. The analysis considers single-fault, double faults, and the effects those faults may have on the system behaviour, depending on the distribution of the motor rotational directions. The analysis shows that a careful selection of an octocopter configuration structure may additionally influence the overall maneuverability of the system and it can make the octocopter more fault-tolerant to variety of fault states. For instance, in case the probability of a double motor fault state is high, it is possible to select an octocopter based on the PPNNPPNN config-

uration structure to increase reliability of the system. Other multiple faults, including triple and quadruple faults, can be analyzed under the same framework as well. However, the occurrence probabilities of such faults are much lower, so these faults are not considered in the book.

Chapter 5 provides a full algorithm to construct a risk-sensitive motion planner (RSP). The RSP is a risk-aware planner which is capable of including the relevant information about mission-dependant constraints which are related to potential fault states and imposed to the maneuverability of an octocopter system into the planning stage. In this way, the reference trajectories which are designed to follow a given sequence of mission waypoints are more appropriate in case a motor failure occurs during the mission execution than in case when this information are ignored as in case of a risk-insensitive motion planner (RIP). The obtained results of the RSP are compared to the results obtained with the RIP and the risk-conservative planner (RCP). Unlike the RSP planner, the RCP takes full information about fault states regardless of their relevance to the selected mission. The results related to any single- and double motor faults show that the RSP planner outperforms the RIP and RCP planners in case any of those faults occur during the mission execution, while it preserves good performance of the RIP and safety of the RCP approach.

Bibliography

- [1] Lionel Basson. *Control allocation as part of a fault-tolerant control architecture for UAV s*. PhD thesis, Stellenbosch: University of Stellenbosch, 2011.
- [2] C Berbra, S Lesecq, and JJ Martinez. A multi-observer switching strategy for fault-tolerant control of a quadrotor helicopter. In *Control and Automation, 2008 16th Mediterranean Conference on*, pages 1094–1099. IEEE, 2008.
- [3] John David Blom. *Unmanned Aerial Systems: A Historical Perspective*, volume 45. Combat Studies Institute Press, 2010.
- [4] Samir Bouabdallah. *Design and control of Quad rotors with Application to Autonomous flying*. PhD thesis, PhDM thesis, Ecole Polytechnique Federale De Lausanne, Laboratoire de systemes autonomes 1, Section De microtechnique, 2007.
- [5] Samir Bouabdallah, Pierpaolo Murrieri, and Roland Siegwart. Design and control of an indoor micro quadrotor. In *IEEE International Conference on Robotics and Automation, 2004. Proceedings. ICRA'04. 2004*, volume 5, pages 4393–4398. IEEE, 2004.
- [6] Samir Bouabdallah and Roland Siegwart. Backstepping and sliding-mode techniques applied to an indoor micro quadrotor. In *Proceedings of the 2005 IEEE international conference on robotics and automation*, pages 2247–2252. IEEE, 2005.
- [7] Alessandro Casavola and Emanuele Garone. Fault-tolerant adaptive control allocation schemes for overactuated systems. *International journal of robust and nonlinear control*, 20(17):1958–1980, 2010.
- [8] Hsiang-Kuan Chang, Yih-Chi Tan, Jihn-Sung Lai, Tsung-Yi Pan, Tzu-Ming Liu, and Ching-Pin Tung. Improvement of a drainage system for flood management with assessment of the potential effects of climate change. *Hydrological Sciences Journal*, 58(8):1581–1597, 2013.
- [9] Martinez-De Dios, A Ollero, et al. Automatic detection of windows thermal heat losses in buildings using UAV s. In *Automation Congress, 2006. WAC'06. World*, pages 1–6. IEEE, 2006.

- [10] Patrick Doherty and Piotr Rudol. A uav search and rescue scenario with human body detection and geolocalization. In *AI 2007: Advances in Artificial Intelligence*, pages 1–13. Springer, 2007.
- [11] Graham R Drozeski, Bhaskar Saha, and George J Vachtsevanos. A fault detection and reconfigurable control architecture for unmanned aerial vehicles. In *Aerospace Conference, 2005 IEEE*, pages 1–9. IEEE, 2005.
- [12] Guang-Xun Du, Quan Quan, and Kai-Yuan Cai. Controllability analysis and degraded control for a class of hexacopters subject to rotor failures. *Journal of Intelligent & Robotic Systems*, 78(1):143–157, 2015.
- [13] Guangxun Du, Quan Quan, Binxian Yang, and K Cai. Controllability analysis for a class of multirotors subject to rotor failure/wear. *Comput. Res. Repository (CoRR)*, 2014.
- [14] Claude Flener, Matti Vaaja, Anttoni Jaakkola, Anssi Krooks, Harri Kaartinen, Antero Kukko, Elina Kasvi, Hannu Hyyppä, Juha Hyyppä, and Petteri Alho. Seamless mapping of river channels at high resolution using mobile lidar and UAV -photography. *Remote Sensing*, 5(12):6382–6407, 2013.
- [15] Claude Flener, Matti Vaaja, Anttoni Jaakkola, Anssi Krooks, Harri Kaartinen, Antero Kukko, Elina Kasvi, Hannu Hyyppä, Juha Hyyppä, and Petteri Alho. Seamless mapping of river channels at high resolution using mobile lidar and UAV -photography. *Remote Sensing*, 5(12):6382–6407, 2013.
- [16] Friedrich Fraundorfer, Lionel Heng, Dominik Honegger, Gim Hee Lee, Lorenz Meier, Petri Tanskanen, and Marc Pollefeys. Vision-based autonomous mapping and exploration using a quadrotor mav. In *Intelligent Robots and Systems (IROS), 2012 IEEE/RSJ International Conference on*, pages 4557–4564. IEEE, 2012.
- [17] Alessandro Freddi, Sauro Longhi, and Andrea Monteriù. A diagnostic thau observer for a class of unmanned vehicles. *Journal of Intelligent & Robotic Systems*, 67(1):61–73, 2012.
- [18] Michael Freed, Robert Harris, and M Shafto. Human-interaction challenges in UAV -based autonomous surveillance. In *Proceedings of the 2004 Spring Symposium on Interactions Between Humans and Autonomous Systems Over Extended Operations*, 2004.
- [19] Pedro Castillo Garcia, Rogelio Lozano, and Alejandro Enrique Dzul. *Modelling and control of mini-flying machines*. Springer Science & Business Media, 2006.
- [20] Anouck R Girard, Adam S Howell, and J Karl Hedrick. Border patrol and surveillance missions using multiple unmanned air vehicles. In *Decision*

- and Control, 2004. CDC. 43rd IEEE Conference on, volume 1, pages 620–625. IEEE, 2004.
- [21] Torkel Glad and Ola Härkegård. Flight control design using backstepping. *Linköping University Electronic press*, 2000.
- [22] Ian Golightly and Dewi Jones. Visual control of an unmanned aerial vehicle for power line inspection. In *Advanced Robotics, 2005. ICAR'05. Proceedings., 12th International Conference on*, pages 288–295. IEEE, 2005.
- [23] Michael A Goodrich, Bryan S Morse, Damon Gerhardt, Joseph L Cooper, Morgan Quigley, Julie A Adams, and Curtis Humphrey. Supporting wilderness search and rescue using a camera-equipped mini UAV. *Journal of Field Robotics*, 25(1-2):89–110, 2008.
- [24] Ola Harkegard and S Torkel Glad. A backstepping design for flight path angle control. In *Decision and Control, 2000. Proceedings of the 39th IEEE Conference on*, volume 4, pages 3570–3575. IEEE, 2000.
- [25] Mostafa Hassanalian and Abdessattar Abdelkefi. Classifications, applications, and design challenges of drones: A review. *Progress in Aerospace Sciences*, 91:99–131, 2017.
- [26] John Safko Herbert Goldstein, Charles Poole. *Classical Mechanics*. Addison Wesley, 2014.
- [27] Inseok Hwang, Sungwan Kim, Youdan Kim, and Chze Eng Seah. A survey of fault detection, isolation, and reconfiguration methods. *IEEE transactions on control systems technology*, 18(3):636–653, 2009.
- [28] Rolf Isermann and Marco Münchhof. *Identification of dynamic systems: an introduction with applications*. Springer Science & Business Media, 2010.
- [29] Hojjat A Izadi, Youmin Zhang, and Brandon W Gordon. Fault tolerant model predictive control of quad-rotor helicopters with actuator fault estimation. *IFAC Proceedings Volumes*, 44(1):6343–6348, 2011.
- [30] Xiaozheng Jin, Guanghong Yang, and Li Peng. Robust adaptive tracking control of distributed delay systems with actuator and communication failures. *Asian Journal of Control*, 14(5):1282–1298, 2012.
- [31] Tor A Johansen and Thor I Fossen. Control allocation—a survey. *Automatica*, 49(5):1087–1103, 2013.
- [32] Rudaba Khan, Paul Williams, Robin Hill, Cees Bil, et al. Fault tolerant flight control system design for UAV ’s using nonlinear model predictive contro. *Australian Control Conference, 10-11 November 2011, Melbourne, Australia*, 2011.

- [33] Tomáš Krajník, Vojtěch Vonásek, Daniel Fišer, and Jan Faigl. Ar-drone as a platform for robotic research and education. In *Research and Education in Robotics-EUROBOT 2011*, pages 172–186. Springer, 2011.
- [34] Muhamed Kuric, Bakir Lacevic, Nedim Osmic, and Adnan Tahirovic. Rls-based fault-tolerant tracking control of multirotor aerial vehicles. In *2017 IEEE International Conference on Advanced Intelligent Mechatronics (AIM)*, pages 1148–1153. IEEE, 2017.
- [35] Muhamed Kuric, Nedim Osmic, and Adnan Tahirovic. Multirotor aerial vehicle modeling in modelica. In *Proceedings of 12th International Modelica Conference, Prague, Czech Republic, May 15-17, 2017*, pages 373–380. Linköping University Electronic Press, 2017.
- [36] Alex Kushleyev, Daniel Mellinger, Caitlin Powers, and Vijay Kumar. Towards a swarm of agile micro quadrotors. *Autonomous Robots*, 35(4):287–300, 2013.
- [37] Joao M Lemos, Inês Sampaio, Manuel Rijo, and Luis M Rato. Actuator fault tolerant lqg control of a water delivery canal. In *Control and Fault-Tolerant Systems (SysTol), 2013 Conference on*, pages 432–437. IEEE, 2013.
- [38] Zhengrong Li, Yuee Liu, Ross Hayward, Jinglan Zhang, and Jinhai Cai. Knowledge-based power line detection for UAV surveillance and inspection systems. In *Image and Vision Computing New Zealand, 2008. IVCNZ 2008. 23rd International Conference*, pages 1–6. IEEE, 2008.
- [39] Quentin Lindsey, Daniel Mellinger, and Vijay Kumar. Construction of cubic structures with quadrotor teams. *Proc. Robotics: Science & Systems VII*, 2011.
- [40] Josip Lorincz, Adnan Tahirović, and Biljana Risteska Stojkoska. A novel real-time unmanned aerial vehicles-based disaster management framework. In *2021 29th Telecommunications Forum (TELFOR)*, pages 1–4. IEEE, 2021.
- [41] Jan Lunze. From fault diagnosis to reconfigurable control: A unified concept. In *2016 3rd Conference on Control and Fault-Tolerant Systems (SysTol)*, pages 413–421. IEEE, 2016.
- [42] Sergei Lupashin, Markus Hehn, Mark W Mueller, Angela P Schoellig, Michael Sherback, and Raffaello D’Andrea. A platform for aerial robotics research and demonstration: The flying machine arena. *Mechatronics*, 24(1):41–54, 2014.
- [43] Tarek Madani and Abdelaziz Benallegue. Control of a quadrotor mini-helicopter via full state backstepping technique. In *Decision and Control, 2006 45th IEEE Conference on*, pages 1515–1520. IEEE, 2006.

- [44] Robert Mahony, Vijay Kumar, and Peter Corke. Multirotor aerial vehicles: Modeling, estimation, and control of quadrotor. *IEEE robotics & automation magazine*, 19(3):20–32, 2012.
- [45] Iván Maza, Fernando Caballero, Jesús Capitán, JR Martínez-de Dios, and Aníbal Ollero. Experimental results in multi-UAV coordination for disaster management and civil security applications. *Journal of intelligent & robotic systems*, 61(1-4):563–585, 2011.
- [46] Hamza Mehmood, Takuma Nakamura, and Eric N Johnson. A maneuverability analysis of a novel hexarotor UAV concept. In *2016 International Conference on Unmanned Aircraft Systems (ICUAS)*, pages 437–446. IEEE, 2016.
- [47] Daniel Mellinger and Vijay Kumar. Minimum snap trajectory generation and control for quadrotors. In *2011 IEEE International Conference on Robotics and Automation*, pages 2520–2525. IEEE, 2011.
- [48] Daniel Mellinger, Nathan Michael, and Vijay Kumar. Trajectory generation and control for precise aggressive maneuvers with quadrotors. *The International Journal of Robotics Research*, 31(5):664–674, 2012.
- [49] L.F. Mendonca, S.M. Vieira, J.M.C. Sousa, and J.M.G. Sa da Costa. Fault accommodation using fuzzy predictive control. In *Fuzzy Systems, 2006 IEEE International Conference on*, pages 1535–1542, 2006.
- [50] Najib Metni and Tarek Hamel. A UAV for bridge inspection: Visual servoing control law with orientation limits. *Automation in construction*, 17(1):3–10, 2007.
- [51] Nathan Michael, Daniel Mellinger, Quentin Lindsey, and Vijay Kumar. The grasp multiple micro-UAV testbed. *IEEE Robotics & Automation Magazine*, 17(3):56–65, 2010.
- [52] Giulia Michieletto, Markus Ryll, and Antonio Franchi. Control of statically hoverable multi-rotor aerial vehicles and application to rotor-failure robustness for hexarotors. In *2017 IEEE International Conference on Robotics and Automation (ICRA)*, pages 2747–2752. IEEE, 2017.
- [53] David Morin. *Introduction to classical mechanics: with problems and solutions*. Cambridge University Press, 2008.
- [54] Mark W Mueller and Raffaello D’Andrea. Stability and control of a quadcopter despite the complete loss of one, two, or three propellers. In *2014 IEEE international conference on robotics and automation (ICRA)*, pages 45–52. IEEE, 2014.
- [55] Mark W Mueller and Raffaello D’Andrea. Stability and control of a quadcopter despite the complete loss of one, two, or three propellers. In

- 2014 IEEE international conference on robotics and automation (ICRA)*, pages 45–52. IEEE, 2014.
- [56] Mark W Mueller and Raffaello D’Andrea. Relaxed hover solutions for multicopters: Application to algorithmic redundancy and novel vehicles. *The International Journal of Robotics Research*, 35(8):873–889, 2016.
- [57] Mark Müller, Sergei Lupashin, and Raffaello D’Andrea. Quadrocopter ball juggling. In *2011 IEEE/RSJ international conference on Intelligent Robots and Systems*, pages 5113–5120. IEEE, 2011.
- [58] Michael W Oppenheimer, David B Doman, and Michael A Bolender. Control allocation for over-actuated systems. In *Control and Automation, 2006. MED’06. 14th Mediterranean Conference on*, pages 1–6. IEEE, 2006.
- [59] Nedim Osmić, Muhamed Kurić, and Ivan Petrović. Detailed octorotor modeling and pd control. In *2016 IEEE International Conference on Systems, Man, and Cybernetics (SMC)*, pages 002182–002189. IEEE, 2016.
- [60] Nedim Osmic, Anel Tahirbegovic, Adnan Tahirovic, and Stjepan Bogdan. Failure mode and effects analysis for large scale multirotor unmanned aerial vehicle controlled by moving mass system. In *2018 IEEE International Systems Engineering Symposium (ISSE)*, pages 1–8. IEEE, 2018.
- [61] Nedim Osmic, Adnan Tahirovic, and Ivan Petrovic. Risk-sensitive motion planning for mavs based on mission-related fault-tolerant analysis. *Automatika*, 61(2):295–311, 2020.
- [62] Anuj Puri. A survey of unmanned aerial vehicles (UAV) for traffic surveillance. *Department of computer science and engineering, University of South Florida*, 2005.
- [63] Guilherme V Raffo, Manuel G Ortega, and Francisco R Rubio. An integral predictive/nonlinear hinf control structure for a quadrotor helicopter. *Automatica*, 46(1):29–39, 2010.
- [64] Filippo Rinaldi, A Gargioli, and Fulvia Quagliotti. Pid and lq regulation of a multirotor attitude: Mathematical modelling, simulations and experimental results. *Journal of Intelligent and Robotic Systems*, 73(1-4):33–50, 2014.
- [65] Robin Ritz, Mark W Müller, Markus Hehn, and Raffaello D’Andrea. Co-operative quadrocopter ball throwing and catching. In *2012 IEEE/RSJ International Conference on Intelligent Robots and Systems*, pages 4972–4978. IEEE, 2012.
- [66] Majd Saied, Hassan Shraim, Clovis Francis, Isabelle Fantoni, and Benjamin Lussier. Controllability analysis and motors failures symmetry in

- a coaxial octorotor. In *2015 Third International Conference on Technological Advances in Electrical, Electronics and Computer Engineering (TAECE)*, pages 245–250. IEEE, 2015.
- [67] Thomas Schneider. *Fault-tolerant Multirotor Systems*. MSC thesis, ETH Zurich, Swiss Federal Institute of Technology Zurich, 2011.
- [68] Farid Sharifi, Mostafa Mirzaei, Brandon W Gordon, and Youmin Zhang. Fault tolerant control of a quadrotor UAV using sliding mode control. In *Control and Fault-Tolerant Systems (SysTol), 2010 Conference on*, pages 239–244. IEEE, 2010.
- [69] Shaojie Shen, Nathan Michael, and Vijay Kumar. Autonomous multi-floor indoor navigation with a computationally constrained mav. In *2011 IEEE International Conference on Robotics and Automation*, pages 20–25. IEEE, 2011.
- [70] Shaojie Shen, Yash Mulgaonkar, Nathan Michael, and Vijay Kumar. Multi-sensor fusion for robust autonomous flight in indoor and outdoor environments with a rotorcraft mav. In *2014 IEEE International Conference on Robotics and Automation (ICRA)*, pages 4974–4981. IEEE, 2014.
- [71] Dongjie Shi, Binxian Yang, and Quan Quan. Reliability analysis of multicopter configurations based on controllability theory. In *2016 35th Chinese Control Conference (CCC)*, pages 6740–6745. IEEE, 2016.
- [72] Villani L. Siciliano B., Sciavicco L. and Oriolo G. *Robotics: Modelling, Planning and Control*. Springer, 2009.
- [73] Gilbert Strang. *Linear Algebra and Its Applications*. Thomson Learning Academic Resource Center, 2006.
- [74] Adnan Tahirovic. Discussion on:” control and navigation in manoeuvres of formations of unmanned mobile vehicles”. *European Journal of Control*, 19(2):172, 2013.
- [75] Adnan Tahirovic and Alessandro Astolfi. A convergent solution to the multi-vehicle coverage problem. In *2013 American Control Conference*, pages 4635–4641. IEEE, 2013.
- [76] Adnan Tahirovic, Mehmed Brkic, Aldin Bostan, and Benjamin Seferagic. A receding horizon scheme for constrained multi-vehicle coverage problems. In *2016 IEEE International Conference on Systems, Man, and Cybernetics (SMC)*, pages 004652–004656. IEEE, 2016.
- [77] Teodor Tomic, Korbinian Schmid, Philipp Lutz, Andreas Domel, Michael Kassecker, Elmar Mair, Iris Lynne Grix, Felix Ruess, Michael Suppa,

- and Darius Burschka. Toward a fully autonomous UAV : Research platform for indoor and outdoor urban search and rescue. *IEEE robotics & automation magazine*, 19(3):46–56, 2012.
- [78] Cesar Martinez Torres. *Fault Tolerant Controln by Flatneess approach*. Phd thesis, San Nicolas De Los Garza, Nuevo Leon, 2013.
- [79] Daniel Vey and Jan Lunze. Structural reconfigurability analysis of multirotor UAV s after actuator failures. In *2015 54th IEEE Conference on Decision and Control (CDC)*, pages 5097–5104. IEEE, 2015.
- [80] Tao Wang, Wenfang Xie, and Youmin Zhang. Sliding mode fault tolerant control dealing with modeling uncertainties and actuator faults. *ISA transactions*, 51(3):386–392, 2012.
- [81] Qing Xu, Hao Yang, Bin Jiang, Donghua Zhou, and Youmin Zhang. Adaptive fault-tolerant control design for UAV s formation flight under actuator faults. In *Unmanned Aircraft Systems (ICUAS), 2013 International Conference on*, pages 1097–1105. IEEE, 2013.
- [82] Chunhua Zhang and John M Kovacs. The application of small unmanned aerial systems for precision agriculture: a review. *Precision agriculture*, 13(6):693–712, 2012.
- [83] Youmin Zhang and Jin Jiang. Bibliographical review on reconfigurable fault-tolerant control systems. *Annual reviews in control*, 32(2):229–252, 2008.